FEDERAL UNIVERSITY OF SÃO CARLOS
CENTER FOR EXACT SCIENCES AND TECHNOLOGY
MATERIALS SCIENCE AND ENGINEERING GRADUATE PROGRAM

SYNTHESIS AND CHARACTERIZATION OF $CH_3NH_3SnI_3$, Mn DOPED $CH_3NH_3SnI_3$ AND OXYGEN-DEFICIENT TiO_2 AS VISIBLE-LIGHT ACTIVE SEMICONDUCTORS

Margaret Dawson

São Carlos-SP
2020

FEDERAL UNIVERSITY OF SÃO CARLOS
CENTER FOR EXACT SCIENCES AND TECHNOLOGY
MATERIALS SCIENCE AND ENGINEERING GRADUATE PROGRAM

SYNTHESIS AND CHARACTERIZATION OF $CH_3NH_3SnI_3$, Mn DOPED $CH_3NH_3SnI_3$ AND OXYGEN-DEFICIENT TiO_2 AS VISIBLE-LIGHT ACTIVE SEMICONDUCTORS

Margaret Dawson

Thesis submitted in partial fulfillment of the requirements for the degree DOCTOR OF PHILOSOPHY IN MATERIALS SCIENCE AND ENGINEERING

Advisor: Dr. Márcio Raymundo Morelli
Co-advisor: Dr. Cauê Ribeiro de Oliveira
Funding Agency: (CNPq- Process:141704/2015-2)

São Carlos-SP
2020

DEDICATION

This work is dedicated to my mother,

Beauty Norgbey

And my siblings,

Emmanuella Hofe (In loving memory), Solomon Dawson, John Dawson and David Dawson.

CANDIDATE`S VITAE

Master of Science in Materials Science and Engineering (UFSCar-2015), Bachelor of Science in Materials Engineering with major in Metals (UFSCar - 2012) and Bachelor of Science in Materials Engineering with major in Ceramics (UFSCar - 2011).

UNIVERSIDADE FEDERAL DE SÃO CARLOS

Centro de Ciências Exatas e de Tecnologia
Programa de Pós-Graduação em Ciência e Engenharia de Materiais

Folha de Aprovação

Assinaturas dos membros da comissão examinadora que avaliou e aprovou a Defesa de Tese de Doutorado da candidata Margaret Dawson, realizada em 14/02/2020:

Prof. Dr. Anselmo Ortega Boschi
UFSCar

Prof. Dr. Márcio Raymundo Morelli
UFSCar

Prof. Dr. Marco Aurelio Lutheviciene Cordeiro
UFSCar

Profa. Dra. Elaine Cristina Paris
EMBRAPA

Profa. Dra. Gabriela Byzynski Soares
NanoChemTech

Prof. Dr. Mario Godinho Junior
UFG-Catalão

Certifico que a defesa realizou-se com a participação à distância do(s) membro(s) Márcio Raymundo Morelli, Gabriela Byzynski Soares e, depois das arguições e deliberações realizadas, o(s) participante(s) à distância está(ao) de acordo com o conteúdo do parecer da banca examinadora redigido neste relatório de defesa.

Prof. Dr. Anselmo Ortega Boschi

ACKNOWLEDGEMENT

I thank God, the Federal University of São Carlos (UFSCar) and the Materials Science and Engineering graduate program for giving me the opportunity to study. I am grateful to CNPq for the scholarship (141704/2015-2). This study was financed in part by Coordenação de Aperfeiçoamento de Pessoal de Nível Superior - Brasil (CAPES) - Finance Code 001.

I would like to express my profound gratitude to my advisor, Dr. Márcio Raymundo Morelli, for the guidance, assistance, patience and support throughout the planning, development and completion of this thesis.

I am grateful to my co-advisor, Dr. Cauê Ribeiro de Oliveira, for the technical input, feedbacks, suggestions and timely assistance whenever needed.

I thank the laboratory technicians of the departments of Materials Science and Engineering (PPGCEM-UFSCar) and Chemistry (DQ-UFSCar) as well as Embrapa Instrumentation for their assistance. I would like to thank the nanotechnology research team (Embrapa Instrumentation) and friends for the encouragement, support and advice. I am particularly grateful to Francisco Willian de Souza Lucas, Gabriela Byzynski and Edson Tobias for their valuable suggestions and assistance with the electrochemical analysis.

I would like to thank members of Laboratório de Nanotecnologia e Energia Solar (LNES), Unicamp, for helping with the photovoltaic measurements, especially Jose Carlos and Franciedene Araújo.

I would like to thank Silvia Leticia Fernandes, Laboratório de Novos Materiais e Dispositivos (LNVD), Unesp, for the assistance.

ABSTRACT

$CH_3NH_3SnI_3$ is an environmentally-friendly (lead-free) perovskite whose synthesis depends on SnI_2. Some disadvantages of SnI_2 include high cost and tin(IV) contamination. Thus, $SnSO_4$ and $C_{16}H_{30}O_4Sn$ are presented as cheaper alternatives and different synthesis conditions were studied: 110 ^oC/10 min, 150 ^oC/10 min and 150 ^oC/20 min. Based on X-ray diffraction results, $CH_3NH_3SnI_3$ was successfully synthesized, being 110 ^oC/10 min sufficient for phase formation. However, annealing at 150 ^oC improved crystallinity irrespective of precursor while prolonged annealing time (20 min) was detrimental to the $C_{16}H_{30}O_4Sn$-based perovskite. Film morphology differed by type of precursor. The bandgaps (1.37-1.59 eV) and photoluminescence emissions (831 nm) of the samples characterize them as visible light active semiconductors. Because $CH_3NH_3SnI_3$ suffers from Sn^{2+} oxidation to Sn^{4+}, some studies have proposed doping with metal cations. So far, Mn has not been tested. Thus, Mn (2% and 10% mol) doped $CH_3NH_3SnI_3$ samples were synthesized and characterized. Mn did not disrupt the perovskite structure but slightly increased bandgap. Chlorine from the Mn precursor is not eliminated by annealing, thus could affect material properties. Regarding stability, Mn partially stabilized $CH_3NH_3SnI_3$, indicating the need for an optimum level of doping. Mn doping does not seem to improve the photovoltaic properties of $CH_3NH_3SnI_3$, but it should be noted that the solar cells were not optimized. Several questions about $CH_3NH_3SnI_3$ cells are still open, including alternative TiO_2 compatible with the same. Here, oxygen-deficient TiO_2 powders were studied. Electron paramagnetic spectroscopy and X-ray photoelectron spectroscopy confirmed oxygen vacancy. Photocatalytic and photocurrent tests showed activity under visible light and an optimum level of oxygen vacancies for lower recombination and high charge separation, important properties for photovoltaic applications.

Keywords: Organic-Inorganic tin perovskite; Tin halide perovskite; Mn doping; tin precursor; oxygen deficient TiO_2; solar cell material.

SÍNTESE E CARACTERIZAÇÃO DE $CH_3NH_3SnI_3$, $CH_3NH_3SnI_3$ DOPADA COM Mn E TiO_2 DEFICIENTE EM OXIGÊNIO COMO SEMICONDUTORES ATIVOS NO VISÍVEL

RESUMO

$CH_3NH_3SnI_3$ é uma perovskita ambientalmente amigável (sem chumbo) normalmente sintetizada a partir de SnI_2, que apresenta algumas desvantagens como elevado custo e contaminação por Sn(IV). Diante disso, $SnSO_4$ e $C_{16}H_{30}O_4Sn$ são apresentados como precursores alternativos para a síntese de $CH_3NH_3SnI_3$ em diferentes temperaturas e tempos de tratamentos térmicos (110 ^oC /10 min, 150 ^oC /10 min e 150 ^oC /20 min). A eficácia da síntese de $CH_3NH_3SnI_3$ a partir dos precursores apresentados foi confirmada por raio-X. O tratamento térmico a 110 ^oC /10 min foi suficiente para a formação de fase, a 150 ^oC/10min melhorou a cristalinidade, independentemente do precursor, porém a 150 ^oC/20 min foi prejudicial para a perovskita produzida com $C_{16}H_{30}O_4Sn$. As energias de *bandgaps* entre 1,37-1,59 eV e valores de emissão de fotoluminescência de 831 nm confirmam que as amostras sintetizadas são semicondutores ativos sob luz visível. Além disso, diferentes morfologias de filmes foram obtidas para cada tipo de precursor utilizado. A $CH_3NH_3SnI_3$ sintetizada a partir de SnI_2 foi dopada com Mn (2% e 10% mol de $MnCl_2$) a fim de controlar a sua oxidação. A caracterizacão das amostras dopadas mostrou que o Mn estabiliza parcialmente a $CH_3NH_3SnI_3$ contra degradação, mas não resulta em nenhuma melhora do desempenho final das células solares. Além disso, o cloro proveniente do $MnCl_2$ não foi eliminado durante o tratamento térmico, o que pode influenciar as propriedades finais do material. Observou-se que o Mn não alterou a estrutura da perovskita, mas aumentou ligeiramente a sua energia de bandgap, mas ainda são necessários estudos para otimizar o nível de dopagem. Várias questões sobre as células de $CH_3NH_3SnI_3$ ainda estão abertas, incluindo o TiO_2 alternativo compatível com as mesmas. Neste trabalho, pós de TiO_2 deficientes em oxigênio foram estudados a partir da análise de espectroscopia paramagnética de elétrons e a espectroscopia de fotoelétrons de

raios-X. Os resultados confirmaram a vacância de oxigênio. Os testes fotocatalíticos e fotocorrentes mostraram atividade sob luz visível, um nível ótimo de vacâncias de oxigênio para menor recombinação e alta separação de carga, propriedades importantes para aplicações fotovoltaicas.

Palavras chave: Perovskita orgânica-inorgânica de estanho; Perovskita de Haleto de estanho; Dopagem com Mn; Precursor de estanho; TiO_2 deficiente de oxigenio; Material para célula solar.

PUBLICATIONS

Dawson, M., Ribeiro, C., Morelli, M.R., $MnCl_2$ doping increases phase stability of tin halide perovskites, Materials Science in Semiconducting Processing, vol.123, p. 105908, 2021.

Dawson, M., Ribeiro, C., Morelli, M.R., Characterization of tin halide perovskites based on different tin(II) perovskites, Materials Letters, vol. 308, 131163, 2022.

x

TABLE OF CONTENTS

LIST OF FIGURES

LIST OF TABLES

ABBREVIATIONS

AM	Air mass
ATR	Attenuated total reflectance
CV	Cyclic voltammetry
DMF	N,N-dimethylformamide
DMSO	Dimethyl sulfoxide
DRS	Diffuse Reflectance Spectroscopy
EDX	Energy dispersive X-ray spectroscopy
EIS	Electrochemical impedance spectroscopy
FA	Formamidinium
FEG	Field emission gun
FF	Fill factor
FTIR	Fourier-transform infrared spectroscopy
FTO	Fluorine-doped tin oxide
HRTEM	High resolution transmission electron microscopy
IR	Infra-red
I-V	Current-Voltage
J-V	Current density-Voltage
Jsc	Short-circuit current density
KDa	KiloDaltons
MA	Methylammonium
MAI	Methylammonium iodide
PCE	Power Conversion Efficiency
PL	Photoluminescence
P3HT	Poly(3-hexylthiophene-2,5-diyl)
SAED	Selected area electron diffraction
SEM	Scanning electron microscopy
$TBAPF_6$	Tetrabutylammonium hexafluorophosphate
TEM	Transmission electron microscopy
TGA	Thermogravimetric analysis
USD	United States Dollar

UV	Ultraviolet
Voc	Open-circuit voltage
XRD	X-ray diffraction
XPS	X-ray photoelectron spectroscopy

1 INTRODUCTION

The transition from conventional to renewable energy systems depends on the development of technologies that allow affordable large scale production and the use of cheap resources–being photovoltaics one of the most important technologies to be improved. Since the development of dye-sensitized solar cells (DSSC), TiO_2 has been established as an important component due to its affordability, non-toxicity and chemical stability. Currently, DSSC have not attained their maximum conversion efficiency, thus research efforts have been driven towards light absorbing materials (sensitizers) compatible with the electronic properties of TiO_2 [1].

A recent breakthrough was the development of organic-inorganic metal halide perovskites which consist of methylammonium coordinated with halides and metal cations [2][3]. Although the most studied material is $CH_3NH_3PbI_3$, the replacement of Pb by Sn, an environmentally-benign material ($CH_3NH_3SnI_3$), has gained significant research attention. Several questions about this perovskite are still open, including the most adequate TiO_2 compatible with the same. Given that research on perovskites is in its infancy, there is the need to explore different aspects of the structure and properties of $CH_3NH_3SnI_3$ and TiO_2, in order to understand how these materials can be applied in the future.

This section presents the background for the thesis theme and associated research questions aimed to be answered. The first part discusses the synthesis of $CH_3NH_3SnI_3$ and doping with manganese while the second part focuses on oxygen-deficient TiO_2 .

1.1 $CH_3NH_3SnI_3$

The drawbacks of silicon technology, such as the reduction of silicon dioxide, purification of silicon and wafer production, have motivated the quest for solution-processable solar cell technologies [4][5]. The advantages of solution processing include low temperature synthesis, mass production and flexibility in reagent choice. Some examples of emerging solution-processable solar cells include dye-sensitized solar cells, quantum dot solar cells, organic solar cells and perovskite solar cells [6]. Special attention has been given to organic-inorganic

metal halide perovskites, $CH_3NH_3PbI_3$ (Methylammonium (MA) lead iodide) and $CH_3NH_3SnI_3$ (Methylammonium (MA) tin iodide), due to their high charge carrier mobility [7], good absorption coefficients and direct bandgaps [8].

Figure 1.1 shows the impressive evolution of perovskites (represented by yellow-filled red circle) since their discovery as photovoltaic materials in 2009.

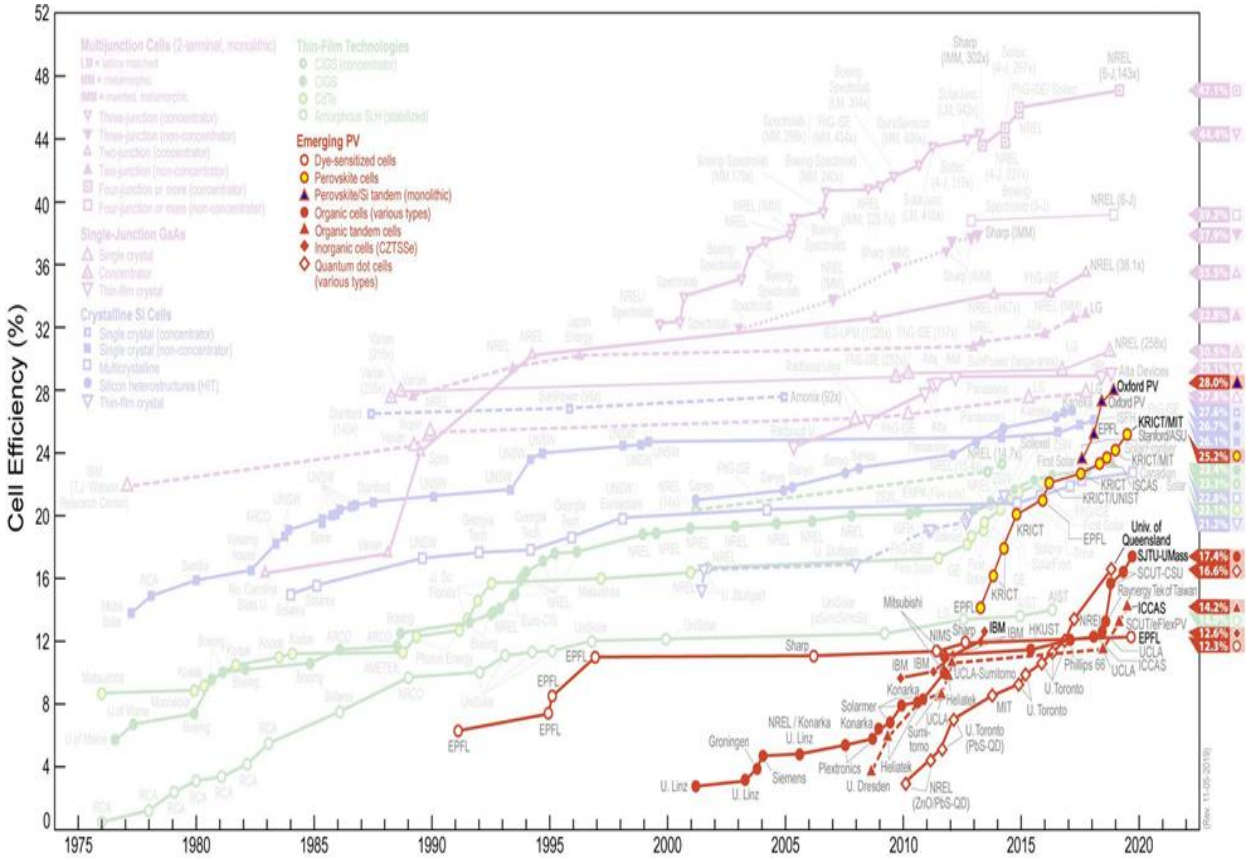

Figure 1.1 - Evolution of the efficiency of perovskite solar cells (represented by yellow-filled red circle), courtesy of the National Renewable Energy Laboratory, Golden, Colorado [9].

In a relatively short span of time (close to a decade), lead perovskite solar cells have attained efficiencies close to well-established technologies such as silicon and have surpassed dye-sensitized solar cells. In fact, the estimated theoretical efficiency of lead perovskites is about 31% [10][11] and the highest laboratory efficiency so far is 25.2% (2019) compared to 26.1% for single crystal silicon cells [9].

In 2009, Kojima et al. (2009) observed an improvement in the conversion efficiency of dye-sensitized solar cells (3.8%) when perovskites, $MAPbBr_3$ and $MAPbI_3$, replaced conventional photoactive dyes [12]. However, Li-based

electrolytes and organic solvents in the set-up promoted the degradation of perovskites. In a similar work, Im et al. (2011) utilized $MAPbI_3$ quantum dots which significantly improved the conversion efficiency to 6.5% [13]. Once again, stability issues related to perovskite dissolution in electrolyte solution were reported. In 2012, Kim et al. (2012) replaced the liquid electrolyte with a solid state hole transport material, spiro-OMeTAD ($C_{81}H_{68}N_4O_8$), resulting in an efficiency of 9.7% [14]. This change in design revolutionized perovskite solar cells.

The expressive evolution of lead perovskites also comes with growing preoccupation with the environment and health. Lead can leak into the environment during the lifetime of the solar cell or after its disposal, especially because of the high solubility of perovskites in water. According to a report on the issue, some researchers argue that encapsulation and safe recycling can mitigate the risk of contamination [15]. While these methods can be feasible, regulations and/or standards on the management of lead in perovskite solar cells have not yet been established.

In this light, possible substitutes of lead such as Sn, Ge, Bi, Sb have been proposed [16]–[19]. Among elements of group 14, tin makes a better substitute because its ionic radius (1.18 Å) [20] is closer to that of Pb(II) (1.19 Å) [21], which implies minor disruption of the perovskite structure. The optical bandgap of tin-based perovskites (around 1.3 eV) is not very far from the ideal bandgap of 1.34 eV considering Shockley-Queisser parameters for optimum solar absorption [22]. Furthermore, the mobility of electrons in tin perovskites (~2320 $cm^2/V{\cdot}s$) was found to be higher than lead perovskites (~66 $cm^2/V{\cdot}s$) [3].

Despite the advantages, tin perovskites are lagging behind lead perovskites as regards conversion efficiency and stability. In fact, the highest reported efficiency of tin-based solar cell is close to 10% compared to 25.2% of lead perovskites [23][9]. This gap in efficiency is rooted in three major causes: facile oxidation of Sn(II) to Sn (IV), poor film quality and irreproducibility. The instability of tin perovskites is correlated with its intrinsic chemical property. From the electronic configuration of Sn, [Kr] $4d^{10}5s^25p^2$, it can assume 2+ and 4+ charges. The stability of its 2+ charge is determined by the reluctance of s electrons to partake in chemical bonds. This property is known as the inert pair

effect and increases down group 14. Therefore, Sn easily loses its s electrons to form a stable 4+ charge compared to Pb.

Early studies show that the facile oxidation of Sn(II) to Sn(IV) disrupts the chemical stability, functionality and reproducibility of $MASnI_3$ solar cells. Once oxidation of Sn(II) occurs, the stoichiometry of the perovskite is altered, causing the formation of Sn(IV), tin vacancies, tin oxides and tin hydroxides [24][25]. It is expected that the replacement of Sn(II) with Sn(IV) produces extra electrons (n doping) but experimental findings have evidenced the predominance of p doping [26]. This is because charge balance can be easily attained through the formation of tin and/or methylammonium vacancies [27]. Furthermore, Sn(II) species can be lost through simple processes, such as spin coating and thermal evaporation, due to their vapor pressure and low tin vacancy formation energy [26].

In general, hole doping increases carrier density often resulting in metal-like conductivity [28] with grave consequences being high recombination and low efficiency [24]. Since it is very difficult to avoid the oxidation of Sn(II), the synthesis of tin perovskites is limited to an inert environment (glovebox), which is unfavorable for industrial scale production. In addition, Sn(IV) contaminants in tin precursors must be absent or very low [29][30].

The most popular tin precursor is SnI_2, usually available with a 99.99% purity [31]. A study showed that Sn(IV) species in a SnI_2 commercial reagent (99.9%) can be quite high, about 10 wt% [29]. This finding is interesting since the purification of tin precursors prior to their use is not a common practice. Although some brands may offer a purity of 99.999%, it comes at a high cost. For instance in 2019, the price of 1 g of ultra-pure SnI_2 (99.999%) was 150 USD compared to 133 USD for 5 g of the same product with 99.99% purity [31].

Non-halide tin precursors such as tin(II) octoate ($C_{16}H_{30}O_4Sn$) and tin(II) sulfate ($SnSO_4$) are more affordable for industrial scale production. A quick search on Sigma-Aldrich´s website (2019) showed that 5 g of SnI_2 cost 133 USD compared to 30.80 USD for 100 g of $SnSO_4$ [32] and 27 USD for 100 g of $C_{16}H_{30}O_4Sn$ [33]. A second advantage is the ability to store these precursors without the need of a glovebox, highlighting them as stable sources of Sn(II). It should however be mentioned that tin(II) octoate is vulnerable to hydrolysis.

To study these materials as potential replacements of SnI_2, preliminary research must be conducted to verify whether they form perovskites and if they have properties similar to their halide counterparts. Parrott et al. (2016) synthesized tin perovskites from tin(II) acetate in order to study the effect of phase transition on charge-carrier lifetime and defects [34]. The results indicate that tin perovskite synthesized from a non-halide precursor presents similar chemical properties as those synthesized with halide precursors. Besides this study, no research has been conducted on the synthesis of tin perovskite using other non-halide tin precursors, for instance $C_{16}H_{30}O_4Sn$ and $SnSO_4$. Thus, there is scant evidence on the synthesis of tin perovskites using non-halide precursors, which reinforces the importance of undertaking the current research. The study seeks to answer whether it is possible to synthesize tin perovskites with the proposed non-halide precursors.

Going back to the issue of poor stability and efficiency, various strategies have been proposed: organic cation substitution [35], doping with metal cations [36], Sn compensator [37], doping with anions [30] and device architecture [38]. Doping is a very attractive approach because the perovskite structure provides three possible doping sites: organic/inorganic cation site, metal cation site and halide site. Given that the Sn component mostly suffers oxidation, doping at the metal cation site has a greater potential to modify stability of the structure.

A growing interest in this field can be evidenced by the diverse cations utilized so far: Pb [25][39]–[41], In [42], Co [43], Bi [44], Sr [45][46], Mg [46], Ca [46] and Ge [47]–[49]. Some beneficial reports include the reduction of metallic property of tin perovskite through In doping [42], reduced Sn(IV) formation through surface passivation via Ge doping [49] and improved binding energies between Sn and I atoms through Co doping [43]. Clearly, each cation has a distinct contribution and exploring a variety of cations adds to knowledge in the field.

Manganese is an abundant and cheap transition element whose halides are not toxic, aligning with the environmental appeal of tin perovskites [50]. Prior literature indicates that manganese plays a crucial role in the phase stability of $CsPbI_3$ through lattice contraction [51][52], enhanced formation energy [53] and

surface passivation [54]. Despite these findings, manganese has not been tested in tin perovskites. It is hypothesized that the reported tendencies may apply to tin perovskites because of similarity in structure (perovskite) and ionic radius (Pb(II) 1.19 Å [21] vs Sn(II) 1.18 Å [20]). Therefore, the synthesis and characterization of manganese doped tin perovskites are important steps in understanding the effects of manganese on the properties of tin perovskites.

Based on the main issues raised, the thesis seeks to answer the following questions: What effect does manganese have on the properties of tin perovskites? Do they contribute to the stability of tin perovskites?

1.2 TiO_2

TiO_2 is an important metal oxide semiconductor which finds applications across many fields. The potential of TiO_2 in light-mediated processes has been highlighted by water splitting [55].

The bandgap of a semiconductor is the heart of any photo-mediated application. It determines the type of absorbed and/or transmitted photons as well as consequent chemical reactions. Accordingly, the bandgap of TiO_2 (3.2 eV) is feasible with photo-mediated processes activated by UV or more energetic photons. A limitation arises in the use of lower energy light sources. For example, TiO_2 can use only a small fraction of the solar spectrum because the same is formed of 6% UV light and 40% visible light [56].

Another important aspect of light-mediated processes is the recombination of photogenerated charge carriers. When photons promote electrons from the valence band to the conduction band, holes are created in the former and electrons in the latter. The free electron and hole can participate in chemical reactions or can be annihilated through recombination. Recombination represents the lowest energy state of charge carriers, hence its occurrence is inevitable but can be delayed and/or controlled.

Given these main problems, research efforts have been directed towards narrowing the bandgap of TiO_2 with the aim of harnessing visible light as well as prolonging carrier lifetime.

The main strategies for narrowing the bandgap of TiO_2 include doping

(anion/cations) and heterojunction formation [57][58]. A common feature of the mentioned methods is the shift in the highest energy level occupied by electrons at 0 K, also known as Fermi level. For an intrinsic semiconductor, it lies in the middle of the bandgap. With doping, acceptor and donor levels shift the Fermi level towards the valence and conduction bands, respectively.

Defects in TiO_2 can create donor or acceptor levels, which shift the Fermi level, resulting in bandgap narrowing as well as prolonged carrier lifetime [59]. Oxygen vacancy is one of the most important defects in TiO_2. Oxygen-deficient TiO_2 can be synthesized by two main routes: oxidizing lower valent titanium precursors or reducing tetravalent titanium precursors such as titanium isopropoxide, titanium diisopropoxide bis(acetylacetonate), titanium(IV) butoxide and TiO_2 [60]. Reduction is widely utilized due to easy access to tetravalent titanium precursors. Among the reducing methods, annealing/calcination in reducing atmospheres (H_2 [61], H_2-Ar [62], H_2-N_2 [63], H_2 plasma [64]), UV irradiation [65] and reducing agents ($NaBH_4$ [66], Al [67], Zn [68]) can be cited. Majority of these methods are expensive and energy intensive, requiring special synthesis atmospheres as well as complex equipments.

In this regard, calcination in air offers the possibility of using simple equipments and experimental conditions. Because this approach uses an oxidizing environment, its success depends on strategies implemented prior to calcination, which facilitate and/or promote the formation of oxygen vacancies during calcination.

Doping with metal cations (Fe [69], Cu [70], Ag [71] among others) promotes oxygen vacancies through substitutional and/or interstitial doping. However, transition metal dopants are known for low quantum efficiency and recombination [72]. Non-metals including N [73] and C [74] have been shown to induce oxygen vacancies. Nitrogen has been reported to reduce oxygen vacancy formation energy [73]–[75]. Carbon can replace oxygen or titanium atoms in the lattice, resulting in oxygen vacancies [76]. In situations where doping is not an option, strategies that promote in-situ reducing atmosphere during calcination in air must be devised. Kong et al. (2015) produced oxygen-deficient TiO_2 by calcining ethanol-impregnated TiO_2 [77]. Zou et al. (2013) synthesized oxygen-

deficient TiO_2 nanoparticles by calcining an amorphous TiO_2 powder combined with imidazole and hydrochloric acid [78]. Zuo et al. (2010) calcined titanium(IV) isopropoxide containing ethanol, hydrochloric acid and 2-ethylimidazole [79]. Ullattil and Periyat (2016) reported the synthesis of oxygen-deficient TiO_2 by titanium glycolate gel combustion [80].

The processing of titanium(IV) reagents can be tuned to promote in-situ reducing atmospheres. Marqbol et al. (2017) demonstrated that the hydrolysis of titanium tetraisopropoxide with ammonia vapor can produce amorphous TiO_2 microspheres, generating oxygen-deficient TiO_2 upon calcination [81]. The incomplete hydrolysis of titanium isopropoxide can induce the formation of oxygen vacancies [82].

Based on these findings, it is reasonable to assume that other processes associated with hydrolysis such as precipitation can lead to similar outcomes. All these processes partly depend on the properties of titanium ions in solution, thus studying the role of precursor concentration in the formation of oxygen vacancies is relevant.

The thesis seeks to answer whether increasing the concentration of Ti-isopropoxide plays a role in the formation of oxygen vacancies. The properties of oxygen-deficient TiO_2 powders will be characterized in order to propose their future use as electron transport layers in perovskite solar cells.

1.3 Objectives

The objective of this research is to understand the effect of different tin precursors and Mn(II) dopant, barely reported in the literature, on the stability, optical and electronic properties of organic-inorganic tin halide perovskites. Also, to contribute to the comprehension of these factors in relation to the design of novel perovskite solar cells.

To conduct a parallel study about oxygen-deficient TiO_2 as a possible electron transport material for tin perovskite materials.

1.3.1 Specific objectives

a) Synthesize $CH_3NH_3SnI_3$ with different tin precursors (tin(II) halide,

tin(II) octoate and tin(II) sulfate).

b) Determine the effect of temperature and time on the properties of $CH_3NH_3SnI_3$ synthesized from non-halide precursors (tin(II) octoate and tin(II) sulfate).
c) Investigate the effect of Mn(II) on the general properties of $CH_3NH_3SnI_3$.
d) Verify the effect of titanium(IV) isopropoxide concentration on the formation of oxygen-deficient TiO_2.
e) Characterize oxygen-deficient TiO_2.

2 LITERATURE REVIEW

This section contains information regarding the elementary aspects of this project.

2.1 Structural properties

A perovskite is primarily the mineral $CaTiO_3$, but is also a generic term for any compound whose stoichiometry and crystal structure are similar to $CaTiO_3$. Organic-inorganic metal halide structures are classified as perovskites because they have the ABX_3 stoichiometry. Figure 2.1 shows the possible cations and anions that can occupy the A, B and X positions of metal halide perovskites.

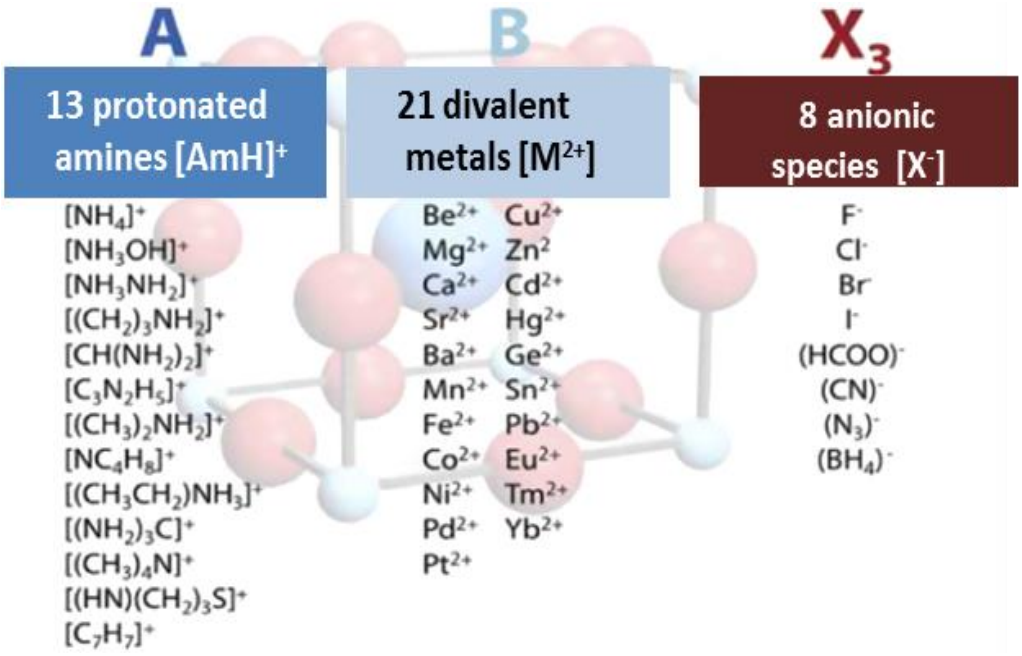

Figure 2.1 - Possible cations and anions that form the perovskite composition. Reproduced from Ref. [83] with permission from The Royal Society of Chemistry.

The A position can be occupied by monovalent organic or inorganic cations (Cs^+, $CH_3NH_3^+$, $CH_5N_2^+$ (Formamidinium, FA)). The B position can be occupied by divalent metal cations such as Sn(II), Pb(II) and Ge(II). Lastly, the X position can be occupied by halides (I^-, Br^-, Cl^-) or other complex anions ($(HCOO)^-$, $(CN)^-$ and $(BH_4)^-$) [83]. To maintain charge balance, the sum of the oxidation states of the A and B cations must be 3, requiring a 3- charge, which is provided by three halide ions. The composition of perovskites allows a wide

variety of options. Kieslich et al. (2015) presented 2352 possible compositions of perovskites based on the permutation of 13 variant protonated amines, 8 anions and 21 divalent metal ions [83]. Examples of common perovskites include $CH_3NH_3SnI_3$, $CsSnI_3$, $CH_3NH_3SnBr_3$, $CH_3NH_3PbI_3$ and $CH_5N_2PbI_3$.

Organic-inorganic metal halide perovskites belong to the family of compounds having crystal structures related to $CaTiO_3$. The ideal perovskite is cubic but can assume lower symmetries, such as tetragonal and orthorhombic structures. The cubic crystal structure of a typical organic inorganic halide perovskites is shown in Figure 2.2.

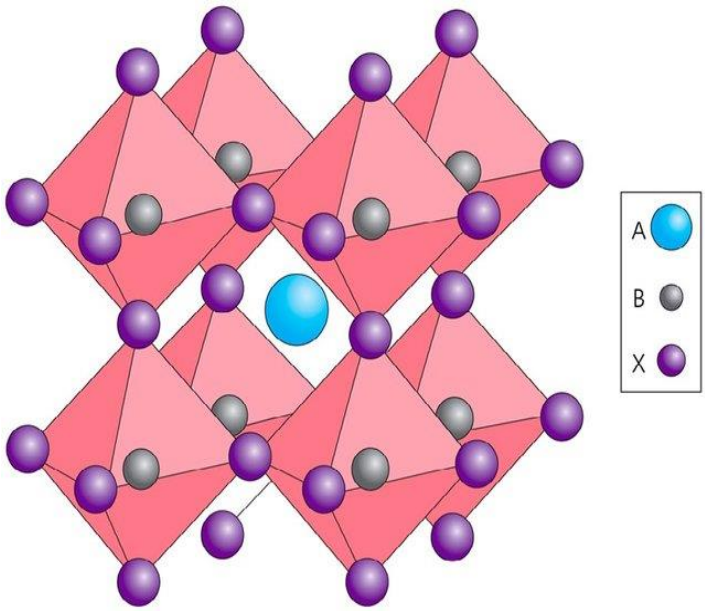

Figure 2.2 - Crystal structure of an organic-inorganic halide perovskite indicating the A organic cation, B metal cation and X halide. Reproduced from Ref. [84] with permission from Springer Nature, copyright 2014.

The A cation ($CH_3NH_3^+$, Cs^+) is located in a cuboctahedral hole and interacts with the inorganic components of the perovskite through hydrogen and dipole interactions [84]–[86]. The corners of the cube are occupied by the B metal cations (Pb(II), Sn(II)) coordinated with six X ions (I^-, Br^-, Cl^-) forming a BX_6 octahedron. The octahedra share corners to form a 3D dimensional network.

High degrees of distortion or tilting can disrupt the perovskite structure. Thus, the selection of ions with adequate ionic radius is very important. Just like any ceramic, the size and coordination number of constituent ions determine structural arrangement. For perovskites, the Goldschmidt tolerance factor (t) and

octahedral factor (μ) predict adequate cation and anion candidates for chemical and structural stability.

Equations 2.1 and 2.2 present the Goldschmidt tolerance factor (t) [87] and octahedral factor (μ) [88], respectively. It can be seen that both equations depend heavily on ionic radius:

$$t = \frac{r_A + r_X}{\sqrt{2}(r_B + r_X)} \quad (2.1)$$

where t, r_A, r_B and r_X are the tolerance factor, radii of the A cation, B cation and X halide, respectively,

$$\mu = \frac{r_B}{r_X} \quad (2.2)$$

where μ, r_B and r_X are the octahedral factor, radius of the B and X ions, respectively.

Most organic metal halide perovskites are in the tolerance range of $0.8 \leq t \leq 1$. A tolerance factor of 1 represents an ideal cubic perovskite structure while values between 0.8 and 1 represent deviation from the ideal cubic structure. Values outside the stability range favor the formation of non-perovskites or 2D perovskites. Considering the ionic radius of methylammonium cation = 1.80 Å, iodide ion = 2.2 Å and Sn(II) cation = 1.18 Å [89], the tolerance factor of tin perovskites is approximately 0.84.

Stability also depends on the octahedra framework. This is accounted for by the octahedral factor (μ). The parameter determines the B metal cation that can fit into the cavity formed by the X anions without disrupting the perovskite structure. The octahedral factor must be greater than 0.414 to ensure the stability of the octahedra units [90].

Tin perovskites present polymorphs according to temperature, rotation and/or distortion of the BX_6 octahedra as well as translation of B and A cations [91]. The three polymorphs of tin perovskite are cubic ($Pm\bar{3}m$), tetragonal phase ($I4/mcm$) and orthorhombic ($Pnma$) [92].

Figure 2.3 shows the polymorphs of lead perovskites similar to tin perovskites, with decreasing temperature and rotation of neighboring octahedra along the c axis.

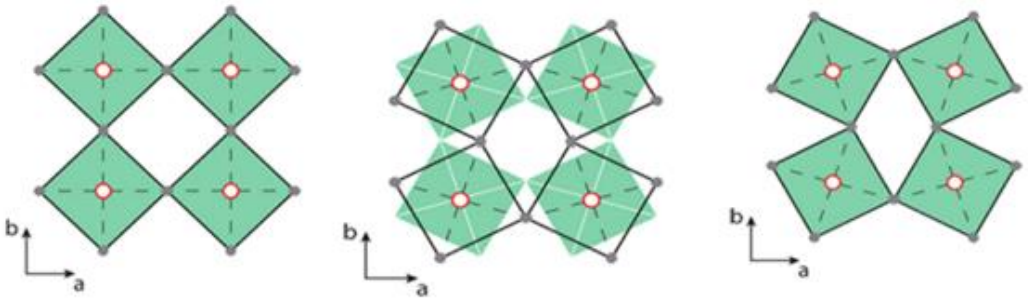

Figure 2.3 - Rotation of neighboring layers of metal halide octahedra along the c axis according to crystal phase. From left to right: cubic, tetragonal and orthorhombic phase. Reproduced from Ref. [86] with permission from Springer Nature, copyright 2016.

Above 295 K (~22 ^{o}C), the cubic phase is stabilized [28]. It is characterized by a $Pm\bar{3}m$ space group. The SnI_6 octahedra do not undergo any rotation but the A cation freely rotates in the cubic cage (Figure 2.3).

With the decrease in temperature, specifically at 275 K (~2 ^{o}C), the cubic phase transforms to tetragonal phase with a *I*4/*mcm* space group [92]. Also, the *P*4*mm* space group has been reported [93]. The SnI_6 octahedra in neighboring planes tilt around the c axis in opposite directions, favoring the tetragonal phase (Figure 2.3) [28]. In this configuration, the motion of the A cation is partially limited.

At lower temperatures, in the range of 108–114 K (-165 ^{o}C to -159 ^{o}C), the orthorhombic phase is stable. The SnI_6 octahedra in the neighboring planes tilt around the c axis in a similar direction (Figure 2.3). In this configuration, there is a complete halt in the rotation of the A cation.

2.1.1 Optical properties

$MASnI_3$ is widely known to be a direct bandgap semiconductor, where the valence band maximum and conduction band minimum coincide in reciprocal space. Typical bandgap values of $MASnI_3$ are in the range of 1.1 to 1.3 eV [3] [24][30][94], enabling absorption in the visible and infra-red regions.

The valence band of $MASnI_3$ consists mainly of Sn (5s) and I (5p) anti-bonding orbitals while the conduction band is formed of Sn (5p) states [28]. In this regard, the SnI_6 octahedron (B and X ions) defines the optical bandgap either

through variation of Sn-I bond length and/or angle [95]. The A site cations can contribute to bandgap tuning through octahedral tilting [96] and lattice distortion [95]. For example, the substitution of methylammonium for a larger cation, formamidinium, can increase bandgap. Bandgaps in the range of 1.4-1.6 eV have been reported for formanidinium tin perovskites [97][98].

Depending on the choice of A cation, the 3D perovskite structure is significantly altered, leading to 2D or 1D structures. This change in structure affects bandgap properties. Lanzetta et al. (2017) observed an increase in bandgap from 3D $MASnI_3$ (1.26 eV) to 2D $(PEA)_2SnI_4$ (1.97 eV) [99], where PEA represents phenethylammonium cation. Coa et al. (2017) reported that the bandgap of $(CH_3(CH_2)_3NH_3)_2(CH_3NH_3)_{n-1}Sn_nI_{3n+1}$ 2D Ruddlesden−Popper perovskites decreased from 1.83 eV (n=1) to 1.42 eV (n=4) with increase in n value, being the lowest (1.2 eV) for n =∞ equivalent to 3D $MASnI_3$ [100]. The replacement of methylammonium by dimethylammonium in $MASnBr_3$ caused a significant increase of the bandgap from 2.05 eV (x = 0) to 2.9 eV for (x=100) [101]. The presence of ethylenediammonium cations in $MASnI_3$ (25%) and $FASnI_3$ (25%) increased the bandgap from 1.25 eV to 1.40 eV [102] in the former, and 1.40 eV to 1.90 eV [103] in the latter.

The B cation influences both the valence and conduction bands, thus modification of this site modifies the B-X bonds and consequently, optoelectronic properties. Given that the valence band maximum is composed of Sn (5s) and I (5p) anti-bonding orbitals, lattice modifications that increase the overlapping of the B-X bond can increase the valence band energy [95]. Accordingly, lattice contraction reduces the bandgap of tin perovskites while tilting of the octahedra has an opposite effect [95].

A study conducted by Dimesso et al. (2018) showed that the bandgap of $MASn_{(1-x)}Mg_xI_3$ decreased with increasing Mg content (x=0 to 0.05). For Mg content greater than 0.05 (X= 0.10 and 0.3%), the bandgap increased compared to the pristine sample [104]. Similarly, $MASn_{(1-x)}Ca_xI_3$ and $MASn_{(1-x)}Sr_xI_3$ presented bandgaps higher and lower than pristine $MASnI_3$ (1.18 eV) depending on dopant content. The authors highlight defects, vacancies, impurities and polarity of dopants as responsible for the changes in bandgap.

Yuan et al. (2017) reported a decrease in the bandgap of $GASn_{1-x}Co_xI_{2-2x}Cl_{1+2x}$ (x=0.025 to 0.15%) from 1.55 eV to 1.51 eV with increase in cobalt content [43]. In this study, the reduction was associated with the replacement of Sn(II) with a smaller cation, Co(II). The bandgap of mixed Ge-Sn perovskite, $FA_{0.75}MA_{0.25}Sn_{1-x}Ge_xI_3$, was found to increase from 1.40 eV to 1.53 eV with increasing Ge content of x=0 to 0.20 [49]. The changes in bandgap were associated with the upshift of the valence and conduction bands. Hasegawa et al. (2017) showed that Bi doping is capable of reducing the bandgap of $MASnI_3$ because the Bi(III) empty 6p orbitals are lower in energy than the Sn(II) empty 5p orbitals, thus the minimum of the conduction band shifts downwards with increase in Bi dopants [44]. Indium doping did not alter the bandgap of $MASnI_3$, although the conduction band minimum should be lowered by indium [42]. The low doping level of indium was cited for this behaviour.

Bandgap tuning through X-site anions is considered a very efficient approach. The replacement of iodide ions with chloride and bromide ions causes a significant shift in bandgap values compared to tuning with cations. In general, the bandgap of $MASnI_3$ increases with choice of halide in the order of I<Br<Cl due to increase in electronegativity [105]. Hao et al. (2014) reported that the bandgap of $MASnI_3$ can be significantly altered from 1.3 eV to 2.5 eV with Br doping in $MASnI_{3-x}Br_x$ (x=0-4) [30]. The effect of chlorine on bandgap modification is highlighted in the work of Kumar et al. (2016), where they show that methylammonium tin chloride perovskite presents a bandgap of 3.7 eV, rendering the perovskite unfeasible for visible light applications [106]. Methylammonium tin chloride perovskites presented bandgaps of 2.63 eV and 2.82 eV, significantly higher than methylammonium tin iodide [107].

2.1.2 Design of perovskite solar cell

There are two main designs of tin perovskite solar cells: the regular (n-i-p) and inverted (p-i-n) designs. The abbreviation p-i-n stands for p semiconductor, intrinsic semiconductor and n semiconductor, respectively. Similarly, n-i-p represents n semiconductor, intrinsic semiconductor and p semiconductors, respectively. In a regular (n-i-p) configuration, a conducting transparent glass

(FTO) functions as a substrate and transparent electrode. The first layer is an n type semiconductor film, usually TiO_2. A compact titanium dioxide film is deposited followed by a second titanium dioxide film, which is mesoporous in nature. In general, TiO_2 serves as an electron transport layer, permitting the movement of electrons and blocking the passage of holes. The mesoscopic layer serves as a base for the nucleation and growth of the perovskite layer, facilitating charge transport and electron collection [108][109].

A solar cell with an n-i-p design is designated mesoscopic or planar depending on the morphology of its electron transport layer (for example, TiO_2). Figure 2.4 presents the regular (n-i-p) design of perovskite cells. For mesoscopic design, the electron transport layer is composed of compact and mesoporous TiO_2 layers according to Figure 2.4 A. For planar designs, the TiO_2 layer is completely compact as shown in Figure 2.4 B.

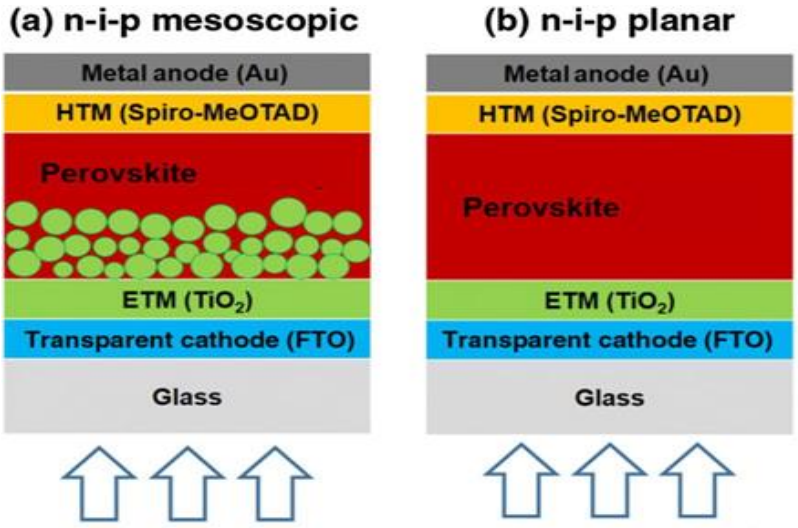

Figure 2.4 - Design of perovskite solar cell A) n-i-p mesoscopic and B) n-i-p planar. Reproduced from Ref. [109].

The hole transport material can be $C_{81}H_{68}N_4O_8$ (Spiro-OMeTAD), or a p-semiconductor. The function of this layer is to transport holes and block electrons. Thus, the hole transport material should have energy levels compatible with the perovskite for the effective extraction of holes.

Spiro-OMeTAD utilized in regular mesoporous devices is usually doped with lithium and cobalt to increase transport properties. These elements were found to increase the degradation of tin perovskites [24][110]. Noel et al. (2014)

replaced lithium bis(trifluoromethanesulfonyl)imide (Li-TFSI), the main lithium salt, with hydrogen bis(trifluoromethanesulfonyl)imide (H-TFSI), which improved stability [24]. Alternative dopant-free hole transport materials such as tetrakis-triphenylamine (TPE) [111], poly(triaryl amine) (PTAA) [112], Poly(3-hexylthiophene) (P3HT) [110] and nickel oxide [113] have been introduced.

Majority of tin perovskite cells adopt the mesoscopic architecture because of the short diffusion length of charge carriers [24]. Another factor is charge buildup at the interface due to inadequate carrier extraction. The reported efficiency are generally low. A study reported a 0.3% efficiency for a planar TiO_2/$MASnI_3$/PTAA device [114]. In relation to a planar design composed of TiO_2/$MASnBr_3$/hole transport material (P3HT, Spiro-OMeTAD and C_{60}), the P3HT-based device presented the highest efficiency (0.35%), followed by C_{60} (0.221%) and Spiro-OMeTAD (0.002%) [110]. For $FASnI_3$ (hollow) perovskite solar cells with a planar design, the use of SnO_2/C_{60} pyrrolidine tris-acid combination as an electron transport material resulted in an exceptional efficiency of 7.40% [115].

Liao et al. (2016) inverted the sequence of the device layers to p-i-n, where the perovskite (intrinsic) is deposited on a hole transport material (dopant-free, PEDOT:PSS), promoting stability [38]. Figure 2.5 shows the inverted (p-i-n) design.

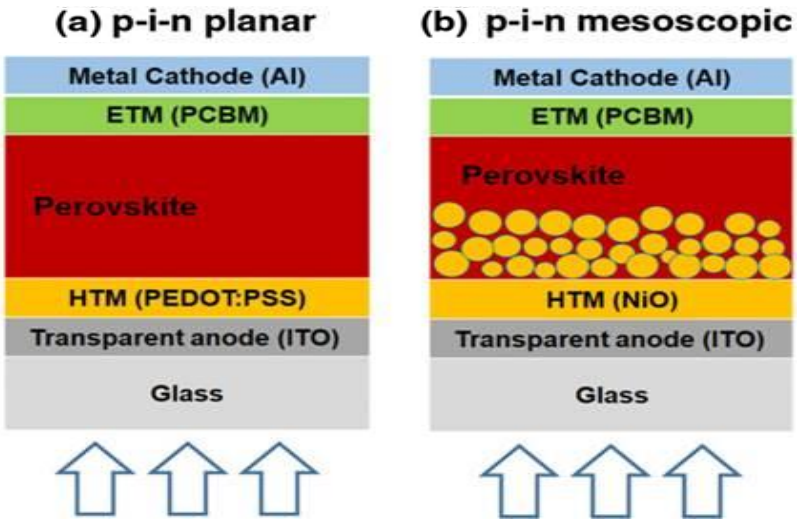

Figure 2.5 - Design of perovskite solar cell A) p-i-n planar and B) p-i-n mesoscopic. Reproduced from Ref. [97].

For the inverted design, the hole transport material is deposited on a glass

substrate (Indium tin oxide, ITO), followed by the perovskite, electron transport material and then, a metal cathode usually Al or Ca. Poly(3,4-ethylenedioxythiophene (PEDOT:PSS) [116] and nickel oxide [113] are examples of some traditional hole transport materials compatible with the p-i-n design. Regarding electron transport materials, [6,6]-Phenyl C_{61} butyric acid methyl ester (PCBM) [117] and C_{60} [38] can be cited.

2.2 Operation of perovskite solar cell

The operation of perovskite solar cells is simplified in three steps: photogeneration of charge carriers, charge transport/separation and charge extraction. The low bandgap of tin perovskites (1.1-1.3 eV) allows absorption of the visible and infra-red portions of the solar spectrum. The excitation of perovskites produces free electrons and holes as well as excitons. Tin perovskites due to their dielectric nature are more likely to produce Wannier-Mott excitons compared to Frenkel excitons [118].

The exciton energy of metal halide perovskites was estimated to be a few millielectronvolts at room temperature indicating the facile production of photogenerated carriers [119]. Other studies reported 12 meV [120] and 16 meV [121] at room temperature. These values are lower than the mean thermal energy at the operation temperature of photovoltaic devices, hence free charge carriers are predominately produced [121].

Once the carriers are generated, they must be separated. The driving force for the selective carrier transport of holes (from perovskite to hole transport material) and electrons (from perovskite to electron transport material) is the band alignment of the transport materials with the perovskite.

Perovskite solar cells work on an n-i-p or p-i-n junction configuration for the separation of charges. For the sake of brevity, only the charge separation mechanism for a n-i-p solar cell composed mainly of an electron transport material (TiO_2), an intrinsic semiconductor (tin perovskite) and a hole transport material (Spiro-OMeTAD) is shown (Figure 2.6). Electrons from the perovskite material can be injected into the electron transport material if there is suitable band alignment. This means that the conduction band energy of the perovskite

should be slightly higher than that of the electron transport material for energetically favorable and efficient electron transport. Examples of electron transport materials are wide bandgap semiconductors such as TiO_2, ZnO, Al_2O_3, SnO_2 et cetera.

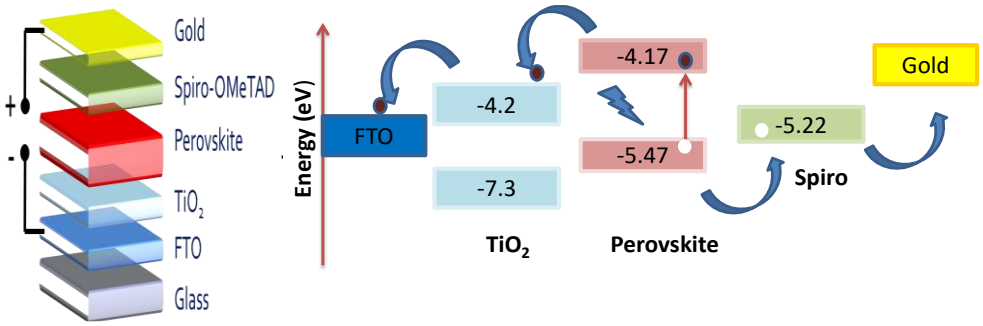

Figure 2.6 - Electron and hole injection at the perovskite-electron transport material interface (TiO_2) and perovskite-hole transport material interface (spiro-OMeTAD), respectively. Design reprinted with permission from ZSW [122].

In a similar way, holes created in a valence band with lower energy (perovskite) can be transferred to a material with a higher energy valence band (hole transport material). Hole transport materials are mainly small molecules and polymers such as Spiro-OMeTAD, P3HT, PTAA among others. Inorganic compounds such as Cu_2O and CuSCN have also been successfully utilized [123].

Figure 2.7 present possible hole and transport materials for tin perovskites with their respective energy levels.

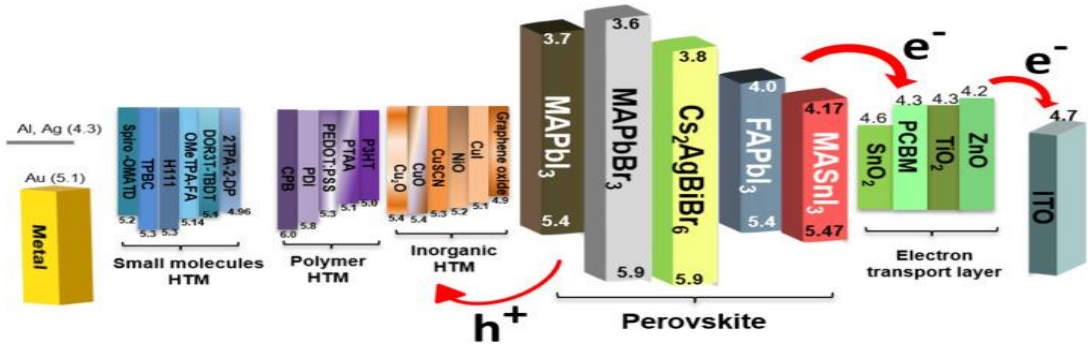

Figure 2.7 - Energy levels of hole and electron transport materials [123]. Reprinted from Advances in hole transport materials engineering for stable and efficient perovskite solar cells, Vol 34, Zinab H. Bakr,Qamar Wali,Azhar Fakharuddin,Lukas Schmidt-Mende,Thomas M. Brown, Rajan Jose, Pages No. 271-305, Copyright (2017), with permission from Elsevier.

The aforementioned transport scenarios are idealized; in fact, holes and

electrons can recombine even before they are transferred at the interface. Radiative recombination occurs in the form of band to band transitions while non-radiative recombination occurs via impurity centers and crystal defects. Another form of recombination between the interface layers of the solar cell is possible.

Besides carrier annihilation through recombination, the dynamics of the carriers determine the efficiency of charge separation and collection. From the point at which they are generated, the carriers must travel a determined pathway (carrier diffusion length) for a specific time (carrier lifetime) in order to be separated and collected. It is desired that the carrier diffusion length be greater than the thickness of the perovskite absorber so that carriers generated within this area can be collected before they recombine [124]. In this case, collection efficiency is higher and recombination rate is lowered.

On the other hand, shorter diffusion length implies that recombination takes place before charge transfer. The pace at which the carriers drift through the semiconductor to the collection interface is controlled by their mobility and effective mass. Scattering due to impurities and lattice defects reduce the mobility of electrons and holes. The diffusion length of carriers in tin perovskites can be as long as 550 nm, which increases charge separation efficiency [114]. The holes in tin perovskites tend to have a lighter effective mass compared to electrons, resulting in high hole mobility and unbalanced charge carrier transport [125].

The next stage of the photovoltaic process involves the collection of electrons and holes by the cathode and anode, respectively. The final stage of the solar cell is characterized by the conversion of the collected charges into current.

2.3 I-V Characterization of solar cells

The relationship between voltage and current in a solar cell can be described by Equation 2.3, the ideal diode equation [126]:

$$I = I_o \left(e^{\frac{qV}{KT}} - 1 \right) \tag{2.3}$$

where I = net current; I_o = dark saturated current; V = applied voltage; q = electron charge; k = Boltzmann's constant and T = absolute temperature.

When a p-n junction is reverse biased without illumination, resistance increases and only a small current crosses the junction. This current is known as the saturated dark current and is represented by $I = -I_o$ [127].

Under illumination, Equation 2.3 becomes Equation 2.4 due to photocurrent generation [126]. The p-n junction then functions as a solar cell:

$$I = I_o \left(e^{\frac{qV}{KT}} - 1\right) - I_{ph} \quad (2.4)$$

where I is net current; I_o is the dark saturated current; V is the voltage applied across the terminals of the diode; q is electron charge; k is the Boltzmann's constant; T is absolute temperature; and I_{ph} is photocurrent.

Figure 2.8 shows the I-V curve of a solar cell in the dark equivalent to a diode. Under illumination, the I-V curve in the dark shifts into the second right quadrant where current is negative and voltage is positive, generating power. When current is analyzed based on a specific cross-sectional area, current density (J) is utilized.

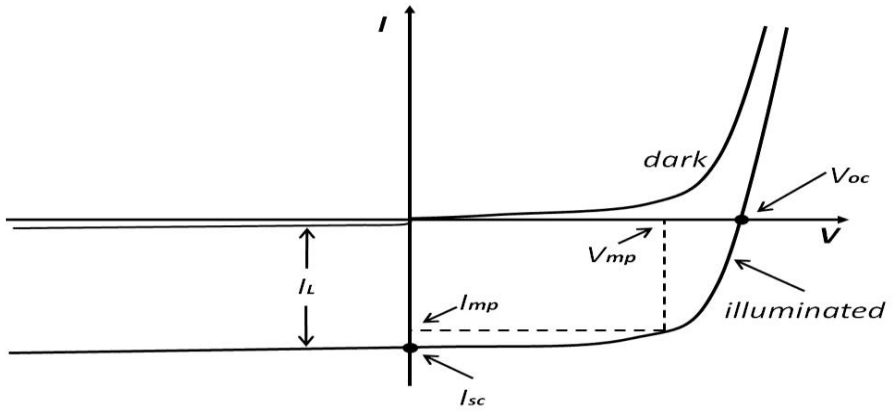

Figure 2.8 - Dislocation of the I-V curve of a solar cell under illumination showing short circuit current (Isc), voltage at maximum power (Vmp), current at maximum power (Imp) and open-circuit voltage (Voc) [128].

In the absence of voltage across the cell, a maximum photocurrent is produced. This current is the short circuit current (Isc) in Figure 2.8. It depends on the optical properties of the material, light intensity, design of the solar cell and collection probability [128]. Open-circuit voltage (Voc) (Figure 2.8) is the maximum voltage a solar cell can provide to an external circuit when current is zero. It is represented by Equation 2.5 [128]:

$$V_{oc} = \frac{nkT}{q} \ln\left(\frac{I_{ph}}{I_o} + 1\right) \quad (2.5)$$

where V_{oc} is the open-circuit voltage; I_o is the dark saturated current; I_{ph} is photocurrent; n is ideality factor 1; q is electron charge; k is the Boltzmann's constant; and T is absolute temperature.

The ratio of light generated and saturation current is an important aspect of the open-circuit voltage. Thus, it can represent the level of recombination in the device [129]. The design of a solar cell and choice of solar absorber influence the built-in potential and consequently, the open-circuit voltage [130]. A higher bandgap is associated with greater potential energy of charge carriers and greater open-circuit voltage.

The maximum power P derived from a cell is the product of the maximum current (Imp) and maximum voltage (Vmp) as shown in Figure 2.8. It is the area of the maximum rectangle that can fit into the I-V curve and this rectangle intersects the curve at the maximum power point. The efficiency of a solar cell depends on the combination of the open-circuit voltage, the short circuit current and the fill factor.

The fill factor (FF) is the ratio of the maximum power to the product of the open-circuit voltage and short circuit current (Equation 2.6):

$$FF = \frac{I_m V_m}{I_{sc} V_{oc}} \quad (2.6)$$

where V_{oc} is the open-circuit voltage; V_m is the voltage at maximum power; Isc is the short circuit current and Im is the current at maximum power.

Efficiency (η) or power conversion efficiency (PCE) is the fraction of incident light that is converted to electricity. In other words, it is the ratio of the maximum power to the incident power where the maximum power is the product of the open-circuit voltage, short circuit current and fill factor according to Equation 2.7:

$$\eta = \frac{\mathrm{I_{sc}V_{oc}FF}}{\mathrm{P_{in}}} \quad (2.7)$$

where Voc is open-circuit voltage; Isc is short circuit current; FF is fill factor; η is conversion efficiency or power conversion efficiency (PCE) and P_{in} is incident power taken as air mass of 1.5 global (AM 1.5G) which is 1000 W/m^2 or 1 sun.

2.4 Synthesis of tin perovskites

Important film properties that affect the functioning of perovskite solar cells include substrate coverage, film thickness, morphology, crystal phase, optical and transport properties. These properties can be manipulated by choice of synthesis method, precursor concentration, solvent, humidity, temperature/time conditions et cetera.

To form $CH_3NH_3SnI_3$ perovskite precursor films, a ratio of 1:1 of tin(II) iodide precursor to methylammonium iodide is utilized. In the case of tin precursors with chlorine or non-halide precursors, a ratio of 1:3 of tin(II) precursor to methylammonium iodide can be employed [131]. Tin perovskites present a fast crystallization behavior evidenced by their formation at room temperature during spin coating. Thus, film quality mainly depends on the kinetics of the reaction between precursors, nucleation density and crystal growth [37][132][133].

Tin perovskite can be synthesized by two main methods: solution and vacuum/vapor processing methods. Depending on the sequence of deposition, the method can be divided into one-step and two-steps [134]. In the one-step method, the precursors (for example, tin precursor plus methylammonium iodide) are deposited in a single step. For the two-step method, each precursor is deposited separately.

2.5 Solution processing

In the one-step method, halide precursors of tin and methylammonium are dissolved in an appropriate solvent. The pioneers of tin perovskites used N,N-dimethylformamide (DMF), a polar aprotic solvent, whose boiling point and vapor pressure is 153 ^oC and 0.49 kPa (25 ^oC) respectively [24][30]. Other polar aprotic solvents include: Dimethyl sulfoxide (DMSO), g-butyrolactone (GBL) and N-Methyl-2-pyrrolidone (NMP). The resultant solution with the precursors is deposited and subsequently annealed for phase formation.

The deposition methods can be spin coating, drop casting and doctor blade, among others. Films produced by the one-step method present variable morphology and non-uniform properties due to fast reaction.

Many methods have been proposed to control the kinetics of film

formation. Solvent engineering plays a major role in controlling the crystallization of tin perovskites through the selection of solvents and the manipulation of their properties for specific interests. Solvents such as DMSO compared to DMF strongly coordinate with tin salts, forming intermediates that slow the crystallization process [132]. As regards DMSO, a solvent with a relatively higher boiling point (189 °C) and a lower vapor pressure (0.056 kPa at 20 °C) compared to DMF, there is the formation of $SnI_2 \cdot 3DMSO$ intermediate phase which controls the rate of crystallization, ensuring highly uniform and pinhole-free perovskite films [132]. The utilization of NMP also results in a controlled crystallization process compared to DMF [132].

To gain balance between the properties of the solvents, they are sometimes mixed. For instance, the combination of DMF and DMSO has been tested in tin perovskites [37][38]. When the combination of solvents is employed, anti-solvents are crucial for good morphology and coverage.

Anti-solvents are solvents that do not dissolve the perovskite but dissolve the perovskite precursors. Some examples are diethyl ether, toluene, chlorobenzene, benzene among others. In the anti-solvent dripping method, an anti-solvent is dropped on the perovskite during spin coating. The function of the anti-solvent is to reduce solubility and thereby promote supersaturation, fast nucleation and growth [135][136]. It also extracts the precursor solvent, usually DMF.

A pyrazine/SnF_2 anti-solvent was adopted for a DMF plus DMSO mixture [37]. A study tested various anti-solvents (chlorobenzene, toluene, and diethyl ether) among tin perovskites prepared with DMF and DMSO solvents containing SnF_2 [38], being diethyl ether coupled with SnF_2 additive produced the most uniform and pinhole-free perovskite.

Anti-solvents applied to a one-solvent solution have also been reported. Fujihara et al. (2013) prepared tin perovskites using a precursor solution with DMSO [137]. In order to obtain a uniform morphology, they dipped the perovskite film in a solution composed of two anti-solvents (toluene and hexane, controlled temperature) which have different miscibilities with DMSO. This process enabled the extraction of DMSO to be controlled and consequently, film formation. Xiao

et al. (2014) proposed the fast crystallization-deposition (FDC) method [135]. In this method, the $MAPbI_3$/DMF solution is spin coated on a substrate and after a specific delay time (e.g. 6 s) and an anti-solvent such as chlorobenzene (CBZ), toluene, is quickly added to the substrate to promote rapid nucleation and growth. Hot anti-solvent dripping was found to improve film coverage by inducing a greater number of nucleation sites [138]. Anti-solvent dripping combined with rapid solvent evaporation was reported to promote higher density of nucleation sites, which results in dense films [139].

Burschka et al. (2013) proposed the two-step method for the controlled synthesis of lead perovskites, which can be adapted for tin perovskites [140]. In the two-step solution process, a separate solution of each precursor, methylammonium iodide and lead iodide, is prepared in an appropriate solvent such as dimethyl sulfoxide (DMSO), N-methyl-2-pyrrolidone(NMP), N,Ndimethylformamide (DMF) and γ-butyrolactone (GBL).

The tin precursor solution is first deposited and annealed. Then, the substrate with the tin precursor is dipped in an isopropanol solution containing methylammonium iodide to form the perovskite. Despite the success of the method among lead perovskites, it is not frequently employed for tin perovskites due to solubility problems [132]. However, sequential deposition using gas phases has been reported. Yokoyama et al. (2016) devised the vapor assisted method where the SnI_2 film on mesoporous TiO_2 substrate reacts with MAI gas to form the perovskite phase [94]. Jung et al. (2016) obtained uniform perovskite film by sequential vacuum deposition of $SnBr_2$ and MABr [110].

Annealing under vapor pressure has been shown to be an effective method for the fabrication of uniform and dense perovskite films. Methylammonium chloride provided a vapor pressure for the synthesis of tin perovskites in the work of Chowdhury et al. (2019) and an efficiency of 6.3% was reported [141]. Liu et al. (2018) employed DMSO vapor and achieved efficiencies over 7% [138]. The vacuum extraction of solvents before annealing improves film morphology by preventing phase segregation, especially when solvents of different volatilization rates are involved [142]. Through one-step flash method, $MASnI_3$ powders were deposited as thin films [143]. Physical vapor deposition of

tin perovskites present advantages such as high reproducibility and lower formation of pinholes [144].

2.6 Advent of tin perovskites

Early reports on the synthesis of organic-inorganic tin halide perovskites dates back to 1978 by Weber et al. (1978) [145]. Scientists became fascinated about their structures, physical properties and conductivity in the 90s and beyond. Using 127I-NQR and 119Sn Mössbauer spectroscopy, Yamada et al. (1990) highlighted the dependence of electrical properties on temperature [146]. Mitza et al. (1994) showed that tin perovskites can assume layered structural configuration with the formula, $(C_4H_9NH_3)_2(CH_3NH_3)_{n-1}Sn_nI_{3n+1}$, as well as crystallize at near room temperature [147]. They can transition from semiconducting to metallic behavior by tuning the dimension of the perovskite layers with increasing n, where (n=∞) forms a tridimensional frame.

Mitza et al. (1995) classified $MASnI_3$ as a low carrier density p-type metal with a Hall hole density ($\simeq 2 \times 10^{19}$ cm^{-3}) and whose resistivity decreases with decrease in temperature [148]. Takahashi et al. (2011) proved that $MASnI_3$ is not a semi-metal as generally perceived but a p-doped semiconductor [28]. Spontaneous hole doping is responsible for metallic transport observed in these materials.

In the midst of all these characterizations, an overlooked detail was the possible application of these materials as solar absorbers. Ogomi et al. (2014) reported a mixed Sn-Pb perovskite solar cell. They observed that pure tin perovskites showed null efficiency due to the oxidation of Sn(II) [149]. However, the addition of Pb in different quantities improved efficiency. An optimum efficiency of 4.18% was obtained with $MASn_{0.5}Pb_{0.5}I_3$. Noel et al. (2014) synthesized the first mesoporous $MASnI_3$ solar cell with an efficiency of 6.4% [24]. The protocols followed were the modification of spiro-OMeTAD with hydrogen bis(tri-fluoromethanesulfonyl)imide (H-TFSI) instead of oxidizing lithium bis(-trifluoromethylsulfonyl)imide salt (Li-TFSI) and encapsulation with epoxy. The authors highlighted the need to suppress the oxidation of Sn(II) so as to reduce background holes density and improve diffusion length of charge carriers. Hao et

al. (2014) synthesized mesoporous $CH_3NH_3SnI_3$ and $CH_3NH_3SnI_{3-x}Br$ perovskites solar cells having conventional spiro-OMeTAD as a hole transport material [30]. An efficiency of 5.7% was achieved by tuning the bandgap through Br doping aimed at improving the open-circuit voltage. Performance loss was mainly attributed to decrease in photocurrent density, poor film coverage and fill factor, arising from p-type doping via Sn(II) oxidation.

2.6.1 Sn compensators

Based on these initial works, efforts were directed towards the control of oxidation. One of the major approach is the use of Sn(II) compensators. They are Sn(II) precursors utilized as extra sources of Sn(II) to self-compensate for the oxidation of Sn(II), impair tin vacancy/Sn(IV) formation and/or act as reducing agents. One can cite SnI_2 [150], $SnBr_2$ [151], $SnCl_2$ [151], SnF_2 [152][37][98], and Sn metal [153] as examples.

Kumar et al. (2014) introduced SnF_2 as a possible solution to reduce the carrier density related to tin oxidation and vacancies in $CsSnI_3$ [152]. In the proposal, SnF_2 will make up for tin vacancies created by oxidation, thereby controlling intrinsic carrier density. Koh et al. (2015) incorporated SnF_2 in formamidinium tin-based perovskites and observed an improvement in stability at optimum amounts through the retarding of Sn(II) oxidation [98]. However, excess SnF_2 promoted segregation and poor morphology, motivating Lee et al. (2016) to introduce pyrazine-SnF_2 complex to mitigate the problem [37]. The versatility of SnF_2 was highlighted by Liao et al. (2016) through its positive effects on morphology and stability [38]. Xiao et al. (2018) revealed that SnF_2 serves as a nucleation site for the formation of uniform films [154].

With the success of SnF_2, alternative tin halide additives such as SnI_2, $SnBr_2$, $SnCl_2$ and Sn metal, have been tested. Marshall et al. (2016) co-doped tin precursors with $SnCl_2$ for the synthesis of $CsSnI_3$ perovskites and reported improved stability compared to $SnBr_2$ and SnF_2 [151]. Song et al. (2017) utilized excess SnI_2 combined with a hydrazine reducing atmosphere for the stabilization of Sn(II) in Cs-based tin perovskites [150]. Nakamura et al. (2020) scavenged Sn(IV) in tin precursor solution using Sn(0) nanoparticles formed from the

reduction of SnF_2 [153].

2.6.2 Reducing agents

Apart from the use of tin compensators, the prevention of oxidation through reducing agents is popular. Dang et al. (2016) synthesized $FASnI_3$ and $MASnI_3$ single crystals from solution using H_3PO_2 as a reducing agent to stabilize Sn(II) [97]. Sn(II) in the $FASnI_3$ sample remained stable for a month in ambient atmosphere. 5-ammonium valeric acid iodide (5-AVAI) has been reported as an efficient additive for the stabilization of methylammonium tin perovskites [155]. The produced powders maintained their oxidation properties for 46.1 hours before total decomposition. The authors attributed the formation of a layer of 5-AVAI to stability.

A study utilized Sn metal as a tin reducing agent in formamidinium iodide precursor solution. The metal acted as a compensator of Sn(II) and reducing agent, leading to a champion efficiency of 6.75% [156]. Ascorbic acid served as a reducing agent for $MA_{0.5}FA_{0.5}Pb_{0.5}Sn_{0.5}I_3$ perovskites. Besides being a reducing agent, it modulates crystallization through intermediate complexes [157]. Song et al. (2017) created a reducing hydrazine vapor atmosphere in a spin coating chamber during the synthesis of tin perovskite, resulting in an efficiency of 3.89% [158].

The mentioned studies show that the efficiency of tin perovskites mainly lies in stabilizing Sn(II). It can be deduced that the synthesis of perovskites has room for a wide range of additives which directly reduce or control the oxidation of Sn(II). The additives do not only reduce oxidation but also act in controlling morphology, perhaps because they slow down the crystallization energy of tin perovskites.

The partial substitution of methylammonium with hydrazine ions improved the stability of $MASnI_3$ against light-induced oxidation of Sn(II) to Sn(IV) and Sn(0) [159]. Li et al. (2019) synthesized $MASnI_3$ by organic cation displacement mediated by hydrazinium tin iodide. Hydrazine produced during the reaction acts as a reducing agent [160]. Kayesh et al. (2018) reported the reducing potential of hydrazinium chloride (N_2H_5Cl) additive in $FASnI_3$ film [161]. The concentration of

Sn(IV) content was reduced by 20% and a high efficiency of 5.4% was attained. Trihydrazine dihydriodide suppressed Sn(IV) levels in $FASnI_3$ films through the formation of hydrazine, which also improved morphology. A high efficiency of 8.48% was reported [162].

2.6.3 Morphology control

Since the application of tin perovskites in solar cells, the importance of film quality has been a subject of concern. For good conversion efficiency, large grain perovskites and good coverage without pinholes are desired. Pioneering studies on tin perovskites utilized the one-step synthesis method [24][30]. In this method, perovskite films are synthesized with a solution containing both organic and inorganic perovskite precursors. The major problems with this method is the fast reactivity between the halide precursors (Sn and methylammonium) and poor solvent evaporation, leading to reduced coverage and pinholes [132].

Hao et al. (2015) modified the one-step method of synthesizing tin perovskites [132]. They found that the reaction kinetics of methylammonium iodide with tin iodide can be controlled by solvent selection. Solvents that have a strong coordination with tin such as dimethyl sulfoxide (DMSO) can form a $SnI_2{\cdot}3DMSO$ intermediate which reacts with methylammonium iodide in a controlled way compared to uncoordinated SnI_2. A power conversion of 3.5% was achieved.

Lee et al. (2016) adapted a solvent method known for being successful for perovskites [37]. In this method, all the precursors are dissolved in N,N-Dimethylformamide (DMF) : DMSO (4:1 volume ratio). During the spin-coating step, an anti-solvent is dropped onto the film. The authors added SnF_2 and pyrazine to reduce phase separation and poor morphology. An efficiency of 4.8% was reported.

Yokoyama et al. (2016) introduced a kinetically controlled gas-solid reaction as a solution to poor morphology [94]. Methylammonium vapor was reacted with SnI_2 film to form tin perovskite, which provided good film coverage and efficiency of 1.89%. Yu et al. (2016) improved the morphology of tin perovskite through a hybrid thermal evaporation [163]. Tin iodide (SnI_2) and

methylammonium iodide (MAI) were heated in crucibles and the vapors were co-deposited to form a film with good coverage and without pinholes. The authors reported an efficiency of 1.7%.

Zhu et al. (2018) synthesized uniform $FASnI_3$ film by sequential deposition of a tin precursor solution (trimethylamine, SnI_2 and SnF_2) followed by formamidinium iodide solution. Efficiencies of 4.34% and 7.09% were achieved for both n-i-p design and inverted solar cells [164]. The formula for success was the addition of trimethylamine in the ethanol/SnI_2 precursor solution. Trimethylamine and SnF_2 form complexes, which slow down the synthesis reaction with formamidinium iodide.

Weiss et al. (2016) deposited SnI_2 by thermal evaporation and subsequently, MAI was deposited [165]. The resultant films were homogeneous and had higher surface coverage than solution-processed films. According to Xiao et al. (2018), precipitates of SnF_2 formed during spin coating can serve as nucleation sites for the homogenous growth of $MASnIBr_2$ [154]. The strategy resulted in an efficiency of 3.7%.

Annealing under vapor pressure has been shown to be an effective method for the fabrication of uniform and dense perovskite films and associated efficiencies were quite higher compared to normal annealing. Methylammonium chloride provided a vapor pressure for the synthesis of tin perovskites in the work of Chowdhury et al. (2019) and an efficiency of 6.3% was reported [141]. Liu et al. (2018) employed dimethyl sulfoxide vapor and achieved efficiencies above 7% [138].

2.7 Doping of tin perovskite

Mixed lead-tin perovskites are one of the pioneering subjects on metal cation doping. The benefits of lead doping include improved efficiency and stability. Ogami et al. (2014) found that adding only 30% of PbI_2 to tin perovskite was sufficient to increase efficiency from 0 to 2% [149]. They also observed an increase in the binding energy of Sn with increase in Pb, pointing to stability.

In another study, the efficiency of tin perovskite increased from 0.04% to 0.11% with 50% increase in Pb [166]. Leijtens et al. (2017) proved that the

oxidation kinetics of tin perovskite is reduced by Pb through the formation of I_2, instead of SnI_4, known to induce the loss of Sn [25].

A 50%-based tin perovskite ($MASn_{0.5}Pb_{0.5}I_3$) presented an efficiency of 13.6%, the highest so far for a tin-based solar cell [39]. The success of the device was reported to be the improvement of morphology through the reduction of crystallization kinetics.

The stability of $FA_{0.75}Cs_{0.25}Sn_{0.5}Pb_{0.5}I_3$ was associated with the contribution of both Sn and Pb orbitals to the valence band minimum which may reduce the propensity of Sn(II) oxidation [167].

Other metal cations have been utilized. Yaun et al. (2017) proposed that cobalt can increase the binding energy of Sn 3d and I 3d bonds, a possible reason for stability against oxidation [43]. The perovskite in the form of $GASn_{1-x}Co_xI_{2-2x}Cl_{1+2x}$ presented interesting properties such as redshift in absorption, bandgap of 1.5 eV and improved stability [43]. Indium decreased the metallic conductivity of tin perovskites while maintaining charge carrier density and bandgap, thus serves as a method of controlling conductivity [42].

Doping of tin perovskites with bismuth has been reported to shift the bottom of the conduction band downwards without increasing the level of charge carriers [44]. Tin perovskites doped with alkali-earth metals have been studied [104]. Sr doping was shown to stabilize Sn(II) oxidation state and cause an energetically favorable distortion of the SnI_6 octahedra through Sr-I bonds. Mg doping increased the thermal stability of tin perovskites through Mg-I bonds. Germanium doping in the form of $FA_{0.75}MA_{0.25}Sn_{1-x}Ge_xI_3$ was shown to reduce the probability of Sn(IV) doping through surface passivation. In this process, Ge fills the defects and vacancies on the surface [49].

2.8 Stability

The main drawback of tin perovskites is their poor stability against moisture, oxygen, temperature and UV radiation. All these factors form part of a solar cell environment, thus tackling instability is relevant to advancing the field of tin perovskites. The oxidation of tin perovskites can be controlled but not eliminated completely because of the thermodynamics involved.

At the moment, there is no standard protocol on stability tests of perovskites, hence reports on stability cannot be compared. Some levels of Sn(IV) are always present, indicating partial stability. When perovskites are in contact with oxygen, Sn(II) oxidizes to Sn(IV). According to Takahashi et al. (2013), the perovskite composition ($CH_3NH_3SnI_3$) becomes $(CH_3NH_3)_{1-2x}Sn^2_{1-x}Sn^4_xI_3$ or $(CH_3NH_3)Sn^2_{1-x}Sn^4_{x/2}I_3$ with oxidation, thus originating $CH_3NH_3^+$ or Sn deficiencies [92]. This process is known as self-doping and the resultant tin vacancies elevate the concentration of holes, reducing resistivity [92]. Noel et al. (2014) reported that oxidation tempers with charge neutrality, culminating in the formation of Sn oxides/hydroxides and methylammonium iodide (MAI) [24].

From experiments, it has been shown that decreasing the concentration of holes to $10^{15}/cm^3$ could increase the diffusion length of $MASnI_3$ from 30 nm to more than a micron compared to lead perovskites [24]. Quenching of photoluminescence through non-radiative recombination is one of the detrimental effects of Sn(IV) species. Several studies have reported the deterioration of crystalline structure, photoluminescence, optical properties and efficiency associated with oxidation [35][24].

Some studies have shown that compounds with the same chemical structure as oxidized perovskites can present interesting properties. Cs_2SnI_6 and MA_2SnI_6 perovskites intentionally prepared with Sn(IV) have been developed as air stable alternatives. Cs_2SnI_6 has a high absorption coefficient (above $10^5/cm$ from 1.7 eV) and a bandgap of 1.48 eV [168] while MA_2SnI_6 presents a bandgap of 1.81 eV and a strong absorption coefficient of $7\times10^4/cm$ [169], properties that make them suitable for solar applications. In this case, oxidized perovskites can be useful if the compound still has all its chemical constituents.

Leijtens et al. (2017) proposed a mechanism behind the oxidation of tin perovskites using thermogravimetric analysis and in-situ X-ray diffraction technique [25]. The oxidation of tin perovskite involves the cooperative breaking of few SnI_2 bonds to form SnI_4 and SnO_2 (Equation 2.8). This route requires a lower energy and loss of tin through the evaporation of SnI_4. For oxidation to occur in the presence of lead, all six SnI_2 bonds must be broken, requiring more energy. In this case, different by-products are formed such as I_2, SnO_2 and PbI_2,

leading to the loss of I_2 instead of Sn (Equation 2.9)[25].

$$2CH_3NH_3SnI_3 + O_2 \rightarrow SnO_2 + 2(CH_3NH_3) + SnI_4 \quad (2.8)$$

$$2CH_3NH_3Sn_{0.5}Pb_{0.5}I_3 + O_2 \rightarrow SnO_2 + 2(CH_3NH_3) + PbI_2 + I_2 \quad (2.9)$$

2.8.1 Humidity

A few numbers of authors have associated humidity with positive effects in lead perovskites. Zhou et al. (2014) reported that films grown in an environment with 30% humidity showed good optoelectrical properties compared to films prepared in dry air due to improved dissolution of the reactants and effective mass transport [170]. Bass et al. (2014) highlighted the effect of moisture on crystallization utilizing $CH_3NH_3PbI_3$ and $CH_3NH_3PbBr_3$ films. In their study, moisture was found to induce rapid crystallization and oriented growth [171]. Moisture assisted crystallization at room temperature was shown by Dubey et al. (2016) to promote nanorods with improved optical, charge transport properties and high performance [172]. The hazardous effects associated with humidity far outweigh the benefits.

When a perovskite film is exposed to humidity or water vapor, it undergoes series of chemical and physical changes that result in degradation. The degradation process usually takes place in two steps and can be reversible. The first step involves the hydration of the perovskite to form an intermediate phase $CH_3NH_3PbI_3 \cdot H_2O$ according to Equation 2.10 [173].

$$CH_3NH_3PbI_3 + H_2O \leftrightarrow CH_3NH_3PbI_3 \cdot H_2O \quad (2.10)$$

The perovskite in its hydrated state is metastable. It transforms into a stable perovskite at 24.85 ^oC depending on the number of water molecules attached to it [174]. Two or more water molecules tend to space out the components of the perovskite, thus preventing any reversible transformation [175]. Li et al. (2016) observed a 6% expansion of the lattice for monohydrate lead perovskite [176]. The hydrated perovskite can take another variant form, $(CH_3NH_3)_4PbI_6 \cdot 2H_2O$, under long exposure to water vapor [177][178].

In the second step, the hydrated perovskite can decompose into PbI_6, CH_3NH_3I and water as shown in Equation 2.11.

$$CH_3NH_3PbI_3 \cdot H_2O \leftrightarrow PbI_2 + CH_3NH_3I + H_2O \quad (2.11)$$

The products of the reaction can be transformed back into a perovskite when dried in the dark or under sunlight provided the products do not suffer further dissociation. The transformation of $(CH_3NH_3)_4PbI_6 \cdot 2H_2O$ is fully reversible under conditions where no volatile products are formed coupled with the absence of phase separation induced by the precipitation of PbI_2 [177][178].

Zhao et al. (2016) observed that an aqueous solution of $CH_3NH_3PbI_3$ powder contained PbI_2 precipitates and a liquid phase of CH_3NH_3I [173]. They therefore concluded that reversibility of the second stage of degradation is also controlled by the solubility of the species in water. Excess water molecules can completely degrade the material compared to a single water molecule due to the dissolution of HI and CH_3NH_2 [179].

2.8.2 Ultraviolet (UV) radiation

The components of the perovskite solar cell can react differently to the absorption of UV light, causing degradation. The perovskite can be destroyed by radiation according to Equation 2.12 [180]. The transport layer, TiO_2, can oxidize iodide ions to iodine according to Equation 2.13 [180]. Methylammonium ion can lose a proton, transforming into methylamine gas (Equation 2.14) [180]. Another possibility is the formation of HI according to Equation 2.15 [180].

$$\mathrm{CH_3NH_3PbI_3} \overset{\mathrm{hv}}{\leftrightarrow} \mathrm{PbI_2} + \mathrm{HI}\uparrow + \mathrm{CH_3NH_2(g)}\uparrow \tag{2.12}$$

$$2I^- \overset{\mathrm{hv}}{\leftrightarrow} \mathrm{I_2} + 2e^- \tag{2.13}$$

$$3\mathrm{CH_3}NH_3{}^+ \overset{\mathrm{hv}}{\leftrightarrow} 3H^+ + 3\mathrm{CH_3NH_2}\uparrow \tag{2.14}$$

$$\mathrm{I_2} + I^- + 3H^+ + 2e^- \overset{\mathrm{hv}}{\leftrightarrow} 3\mathrm{HI}\uparrow \tag{2.15}$$

2.9 Oxygen-deficient TiO_2

Oxygen vacancy is one of the most important defects in TiO_2 which affects optical, physical and chemical properties. It has been reported to promote ferromagnetism, conductivity, photocatalytic activity, resistive switching and photoelectrochemical performance [181]–[183]. The removal of an oxygen atom from the lattice disrupts the electroneutrality of TiO_2 by forming oxygen vacancies

(V_o). Thus, two electrons are bound to the vacant position to restore neutrality. This type of vacancy is known as a neutral oxygen vacancy (F) (Equation 2.16).

$$V_0 + 2e^- \rightarrow F \quad (2.16)$$

The electrons bound to the neutral vacancy can be ionized, generating single positively (F^+ center) charged oxygen vacancy or double positively charged oxygen vacancy (F^{2+} center) [184] as in Equations 2.17 and 2.18, respectively.

$$V_0 + e^- \rightarrow F^+ \quad (2.17)$$

$$V_0 \rightarrow F^{2+} \quad (2.18)$$

Also, the electrons in the neutral oxygen vacancy can reduce Ti^{4+} species to Ti^{3+}. The F^o, F^+ and F^{2+} are known as color centers because they can absorb certain wavelengths, delivering color to their occupant. For example, oxygen-deficient TiO_2 varies in color: gray, black, blue among others [185][186][80]. Oxygen vacancies can reside in the bulk and/or on the surface in the form of a disordered shell [61]. Surface oxygen vacancies are not stable, often oxidizing in air or water [187]. Thus, bulk oxygen vacancies are advantageous in this regard but susceptible to recombination [188].

Oxygen vacancies and Ti^{3+} can be introduced into TiO_2 by calcining in reducing atmospheres such as hydrogen, argon and vacuum [189]. The direct reduction of Ti(IV) can be very expensive, as regards the use of energy, sophisticated equipments and special types of gases. Metal and non-metal doping can promote the formation of oxygen vacancies by calcination in air. This approach uses in-situ reduction by substitutional/interstitial doping, thus the calcination environment is not a determinant. In cases where the system studied is sensitive to dopants, one has to devise strategies to provide an in-situ reducing atmosphere. The process of creating oxygen vacancies through the introduction of Ti^{3+} without any external dopant is termed self-doping [190].

Self-doping through the hydrolysis and/or precipitation of titanium precursors is an emerging field in the synthesis of oxygen-deficient TiO_2 in air. Through the hydrolysis of titanium tetraisopropoxide, Marqbol et al. (2017) were able to obtain oxygen-deficient TiO_2 upon calcination [81]. Karthik et al. (2019) employed the incomplete hydrolysis of titanium isopropoxide as a route for the synthesis of oxygen-deficient TiO_2 [82]. Nawaz et al. (2019) formed precipitates

by adding NH_3 to a solution of $TiCl_4$, glycerol and water [191]. The precipitates were calcined in air to produce oxygen-deficient TiO_2. Precipitation and hydrolysis depend on the concentration of titanium ions in solution, therefore studying their effect on the formation of oxygen vacancies is important.

2.9.1 Role of oxygen vacancies

Oxygen vacancies in TiO_2 enhance visible light adsorption through the formation of states in the bandgap [192]. The oxygen vacancies states are located at 0.75–1.18 eV below the conduction band [193]. Figure 2.9 shows the energy level of oxygen vacancies. The concentration of oxygen vacancies must be sufficient to form a continuous state just below the conduction band instead of localized states [190]. Localized states are detrimental to visible light activity because they act to decrease mobility as well as promote recombination. Thus, having the right concentration of oxygen defects is important [190]. Oxygen vacancies can act as recombination centers as well as promote separation of photoinduced charge carriers and photodegradation.

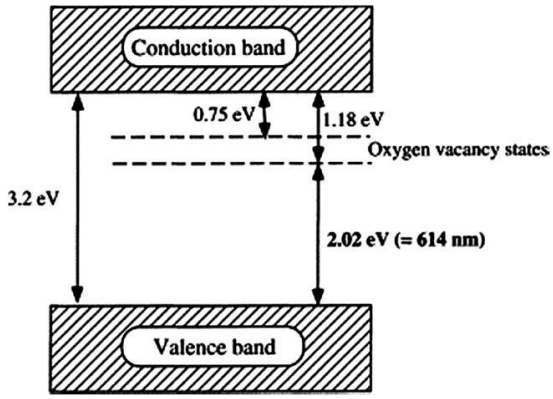

Figure 2.9 - Bandgap model of TiO_2 containing oxygen vacancies[193]. Reprinted from Role of oxygen vacancy in the plasma-treated TiO_2 photocatalyst with visible light activity for NO removal, Vol 161, Isao Nakamura,Nobuaki Negishi,Shuzo Kutsuna,Tatsuhiko Ihara,Shinichi Sugihara,Koji Takeuchi, Pages No. 205-212, Copyright (2000), with permission from Elsevier.

Pan et al. (2013) did not observe satisfactory photocurrent generation among oxygen-deficient samples [194]. The poor performance was attributed to high recombination and poor charge separation. Hole-mediated photo-oxidation

of trimethyl acetate was impaired on oxygen vacancy sites due to recombination between excess electrons and photoexcited holes [195].

Defective TiO_2 presented a photocurrent 10 times higher than normal TiO_2. The improvement in photocurrent was assigned to high absorption of visible light and generation of charge carriers due to the high concentration of oxygen vacancies [186]. Xia et al. (2014) reported that the photocatalytic activity of oxygen-deficient TiO_2 increased with increase in oxygen vacancies regardless of optical absorption [196].

Photogenerated holes react with oxygen absorbed in vacant sites to produce superoxide radicals responsible for the photodegradation of organic species [197]. Also, donor electrons associated with oxygen vacancies can enhance conductivity [198]. Liu et al. (2011) reported that Ti(III) reduced photocatalytic activity through recombination [199].

From the above studies, oxygen vacancies can be beneficial when an optimum level is introduced into the material.

2.10 Summary

Tin halide perovskites have great potential for solar cell applications, but the facile oxidation of Sn(II) is detrimental to their chemical stability and functioning. Among solutions to curb this problem, metal cation doping is versatile due to the numerous options of cations. Prior literature shows that Mn has not been explored in tin perovskites.

In the traditional synthesis of tin perovskites, tin halide precursors, SnI_2 and $SnCl_2$, are mostly used. SnI_2 was shown to contain traces of Sn(IV) depending on its purity. Using high purity levels such as 99.999 % can mitigate this problem, however it comes at a high cost, especially considering large scale production. The application of non-halide tin precursors for the synthesis of tin perovskites is an alternative route for the synthesis of tin perovskite since these precursors are less expensive and can be stable sources of Sn(II).

TiO_2 is one of the most important components of tin perovskite solar cells and functions as a hole transport material. Oxygen defects in TiO_2 materials improve visible light response, photocurrent, surface properties and carrier

lifetime. However, the role of oxygen-deficient TiO_2 in perovskite solar cells is not clear. Thus, there is the need to apply these materials in tin perovskite solar cells.

Oxygen-deficient TiO_2 can be synthesized by oxidizing lower valent titanium precursors or reducing tetravalent titanium precursors including TiO_2. The reduction approach is widely utilized due to easy access to tetravalent titanium precursors. Majority of these methods are expensive and energy intensive, requiring special synthesis atmospheres as well as complex equipments. In this regard, the synthesis of oxygen-deficient TiO_2 based on calcination in air offers the possibility of using simple equipments and experimental conditions.

3 MATERIALS AND METHODS

This section presents the reagents, methods and equipments utilized. Tin perovskites were synthesized using three tin precursors and the one-step method: tin(II) iodide, tin(II) octoate and tin(II) sulfate. The perovskite prepared with tin(II) iodide was doped with manganese (2% and 10% mol).

The samples were characterized by various techniques: X-ray diffraction (XRD), diffuse reflectance spectroscopy (DRS), micro-Raman spectroscopy, photoluminescence spectroscopy, Fourier-transform infrared spectroscopy (FTIR)/attenuated total reflectance (ATR), scanning electron microscopy (SEM), Field emission gun scanning electron microscopy (FEG-SEM), cross-sectional scanning electron microscopy, transmission electron microscopy (TEM) and Energy-dispersive X-ray spectroscopy (EDX).

The electrochemical properties of the tin perovskite (tin(II) iodide precursor) and Mn doped samples were verified in aqueous and non-aqueous media. The photovoltaic properties of the samples were measured.

A part of the chapter covers the synthesis and characterization of oxygen-deficient TiO_2.

3.1 Materials

All the chemical reagents, solvents, substrate and tape were purchased. They were utilized without purification unless otherwise stated. Table 3.1 contains a list (alphabetical order) of the reagents, solvents and substrate as well as a summary of their properties.

Table 3.1 - Reagents, solvents and substrate information.

Reagent/Substrate/ Solvent/Tape	**Chemical formula**	**Manufacturer**	**Properties**
Acetylacetone	$C_5H_8O_2$	Sigma-Aldrich	≥99.9%
Amiloride hydrochloride hydrate	$C_6H_9Cl_2N_7O \cdot 2H_2O$	Sigma-Aldrich	Pharmaceutical Secondary Standard

Chlorobenzene	C_6H_5Cl	Sigma-Aldrich	Anhydrous, 99.8%
Dichloromethane	CH_2Cl_2	Synth	100%
Dimethylformamide (DMF)	C_3H_7NO	Sigma-Aldrich; Panreac	Anhydrous, 99.8%; ASC, 99.8%
Dimethyl sulfoxide (DMSO)	$(CH_3)_2SO$	Sigma-Aldrich	Anhydrous, ≥99.9%
Ethanol	C_2H_6O	Synth	99%
Extran detergent	-	Merck	-
Fluorine-doped tin oxide (FTO)	SnO_2:F	Sigma-Aldrich	Surface resistivity ~7 Ω/sq
Hellmanex detergent	-	Hellma Analytics	-
Hydrochloric acid	HCl	Sigma-Aldrich	37%
Hydrogen peroxide	H_2O_2	Synth	35%
Iodine	I_2	Sigma-Aldrich	≥99.99%
Isopropanol	C_3H_7OH	LCS	100%
Kapton polyimide tape	$C_{22}H_{16}N_2O_3$	Hikari	Resistant to heat, acids and solvents
Manganese chloride	$MnCl_2$	Sigma-Aldrich	≥99%
Methylammonium iodide	CH_3NH_3I	Sigma-Aldrich	98%
Polylactic acid (PLA)	$(C_3H_4O_2)_n$	Nature Works	66000g/mol
Poly(3-hexylthiophene-2,5-diyl) (P3HT)	$(C_{10}H_{14}S)_n$	Sigma-Aldrich	Mw=70,000 kDa kegioregular
Sodium sulfate	Na_2SO_4	Dinamica	99%
Sulfuric acid	H_2SO_4	Synth	98%

Tin(II) iodide	SnI_2	Sigma-Aldrich	Anhydrous, 99.99%
Tin(II) octoate	$C_{16}H_{30}O_4Sn$	Sigma-Aldrich	92.5-100%
Tin(II) sulfate	$SnSO_4$	Sigma-Aldrich	97%
Titanium diisopropoxide bis(acetylacetonate)	$C_{16}H_{28}O_6Ti$	Sigma-Aldrich	75 wt. %
Titanium dioxide paste	TiO_2	Dyesol	Transparent, Mean particle size (20 nm)
Titanium(IV) Isopropoxide	$Ti(OC_3H_7)$	Sigma-Aldrich	97%
Zinc powder	Zn	Sigma-Aldrich	9.99% trace metals basis

3.1.1 Spin coater

A home-made spin coater was designed and constructed to produce the perovskite films. The set-up consists of a 12 V DC motor, which runs up to 12500 rpm. The motor was connected to an AC/DC convertor and a potentiometer to adjust the rotation speed.

3.1.2 Conductive glass

A glass slide coated with fluorine-doped tin oxide film (FTO) served as a substrate for the growth of the perovskite films. The size of the FTO substrates was 3 cm x 1 cm for general characterization. However, the active area was limited to 1 cm^2 for electrochemical measurements. For the photovoltaic devices, a size of approximately 1.25 cm x 1.88 cm was adopted. Note that this area contains four cells.

3.1.3 Amiloride Hydrochloride

Amiloride hydrochloride dihydrate was utilized as a model pharmaceutical for the photocatalytic evaluation of the TiO_2 samples under visible light irradiation.

Amiloride hydrochloride is a salt of amiloride in the class of medications called diuretics. They reduce water retention through the excretion of water and sodium (urine). Accordingly, amiloride is prescribed for the treatment of high blood pressure, congestive heart disease and edema. The use of amiloride is bound to increase given the continuous increase in the prevalence of cardiovascular diseases.

Amiloride is not broken down by the liver, which in turn is excreted from the body in its original form [200]. When released into sewage, it can transform into various metabolites according to pH changes and photo-induced processes. Guanidine, a nitrogen-based metabolite, is known to be very stable and toxic [201]. This property increases the propensity of Amiloride to cause pharmaceutical pollution. Furthermore, in relation to aquatic risk, amiloride is considered harmful with long term effects (Category 3 Chronic Aquatic risk).

The chemical structure of Amiloride is shown in Figure 3.1. It consists of a pyrazine ring with two attached amino groups, one chlorine atom and a acylguanidine side chain [202].

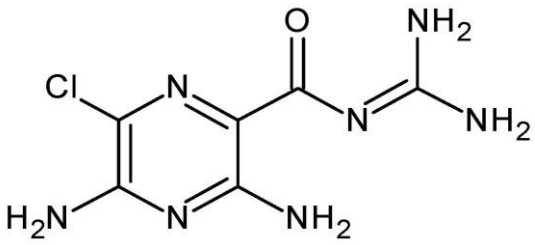

Figure 3.1 - The chemical structure of Amiloride [202].

3.1.4 Tin(II) octoate

Tin(II) octoate also known as tin(II) 2-ethylhexanoate, is an organo-tin(II) compound. It is mostly utilized as a polymerization catalyst for the ring opening of cyclic carboxylic esters (lactones) necessary for polyester formation [203]. In addition, it finds application in the polymer industry as a crosslinking catalyst for polyurethane production [204].

Tin(II) octoate is commercially available as a viscous liquid. It is noted for its feasibility with non-aqueous medium. Therefore, it can be a useful source for the synthesis of tin perovskites. Figure 3.2 shows the structure of tin(II) octoate

marked with tin(II) coordinated with 2-ethylhexanoates chains.

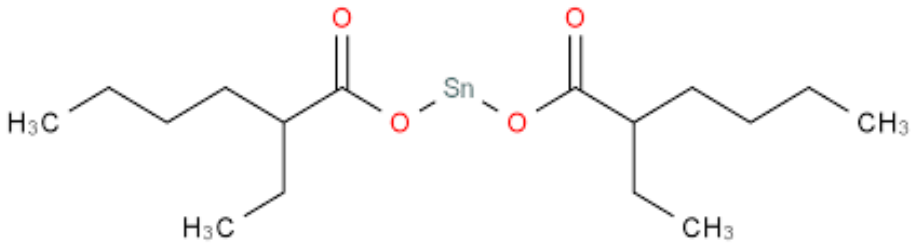

Figure 3.2 - Chemical structure of tin(II) octoate [205].

With the use of adequate non-polar organic solvents, the chains dissociate into Sn(II) and 2-ethylhexanoates.

3.1.5 Polylactic acid

Polylactic acid (PLA) is a biodegradable aliphatic polyester. PLA is usually utilized for 3D printing and presents a relatively low glass transition temperature (60 ºC). Figure 3.3 presents the structure of PLA.

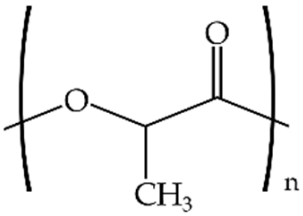

Figure 3.3 - Chemical structure of PLA [206].

PLA was chosen because of its high solubility in dichloromethane, ease of spin coating and crystallization without the need for high temperature.

3.1.6 Substrate cleaning

The cleaning process of the FTO substrates utilized for the films with the exception of the solar cells is presented here. The substrates were immersed in an alkaline detergent, Extran (10% V/V), and ultrasonicated for 15 min. After, they were thoroughly washed with distilled water and subsequently ultra-sonicated in distilled water for 15 min. The substrates were transferred for further sonication (15 min) in ethanol followed by distilled water. They were again ultrasonicated in isopropanol for another 15 min. Finally, the substrates were ultrasonicated in distilled water for 15 min. After, they were dried with nitrogen gas.

3.1.7 Preparation of perovskite solution

Perovskites are sensitive to moisture and oxygen. Therefore, the films were prepared in a MBraun nitrogen filled-glovebox (Embrapa Instrumentation, São Carlos).

The chemical equation governing the production of $MASnI_3$ is shown in Equation 3.1. The use of tin(II) iodide is mostly preferred due to the 1:1 mole ratio of reagents, which eliminates residues.

$$CH_3NH_3I + SnI_2 \rightarrow CH_3NH_3SnI_3 \quad (3.1)$$

To prepare the $CH_3NH_3SnI_3$ solution, besides respecting a mole ratio of 1:1, a 45% weight in 1 mL of DMF was considered. 232.40 mg of methylammonium iodide was dissolved in 0.7 mL DMF under magnetic stirring. After, 544.70 mg of anhydrous tin(II) iodide was dissolved in the methylammonium iodide solution under agitation and the remaining 0.3 mL of DMF was added.

In a separate synthesis, Mn doped films were prepared. $MnCl_2$ (Sigma-Aldrich) was used as a source of Mn because it is cost-effective compared to MnI_2. Two types of doped samples were synthesized: 2 mol % Mn and 10 mol % Mn.

To dope the perovskite with 2% Mn, 232.40 mg of methylammonium iodide (CH_3NH_3I) was completely dissolved in 0.7 mL under magnetic stirring. Then, 533.80 mg of anhydrous tin(II) iodide was dissolved in the solution under magnetic stirring. After the complete dissolution of tin(II) iodide, 3.68 mg of $MnCl_2$ was added followed by the addition of 0.3 mL DMF.

For 10% Mn, 232.40 mg of methylammonium iodide (CH_3NH_3I) was dissolved in 0.7 mL under magnetic stirring. Then, 490.23 mg of anhydrous tin(II) iodide was dissolved in the solution under magnetic stirring. After the complete dissolution of tin(II) iodide, 18.40 mg of $MnCl_2$ was added followed by the addition of 0.3 mL of DMF.

$MASnI_3$ solutions were prepared with two different precursors: tin(II) octoate and tin(II) sulfate. When using non-halide precursors, sufficient iodide ions must be provided through methylammonium iodide. Thus, usually the methylammonium content is relatively higher unlike halide tin precursors. Also,

there can be associated residues when using non-halide precursors.

Equation 3.2 presents the chemical reaction governing the perovskite synthesis using tin octoate.

$$C_{16}H_{30}O_4Sn + 3CH_3NH_3I \rightarrow \ CH_3NH_3SnI_3 \ + \ 2(CH_3NH_3) + C_{16}H_{30}O_4 \qquad (3.2)$$

Methylammonium iodide (700 mg) was dissolved in 0.8 mL of DMF. Subsequently, 0.5 mL of tin(II) octoate was added to the solution to form the precursor solution.

The preparation of the $MASnI_3$ precursor containing $SnSO_4$ followed Equation 3.3. Methylammonium iodide (500 mg) was dissolved in 1 mL DMF. Subsequently, 225 mg of $SnSO_4$ was added to form the precursor solution. $SnSO_4$ did not dissolve completely so the supernatant was utilized.

$$SnSO_4 + 3CH_3NH_3I \rightarrow CH_3NH_3SnI_3 \ + 2(CH_3NH_2) \uparrow \ + H_2SO_4 \qquad (3.3)$$

Figure 3.4 presents the freshly prepared solution from $SnSO_4$. The solution changes to yellow after a day.

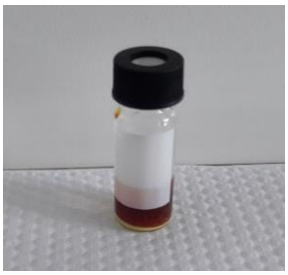

Figure 3.4 - Freshly prepared solution showing undissolved $SnSO_4$.

3.1.8 Deposition of films

The perovskite precursor solutions were deposited by the one-step deposition method. The solutions containing both methylammonium iodide and tin iodide precursors were deposited on previously cleaned FTO by spin coating. Figure 3.5 shows the sequence of the deposition process.

Figure 3.5 - Sequence of film deposition by the one-step method (1000 rpm/30 s and temperatu150 ºC /10 min) [207].

The solution was deposited on the FTO substrate and spun at 1000 rpm for 30 s. After, it was heated on a hotplate at 150 ^{o}C for 10 min. The color of the as-prepared film was black.

Figure 3.6 shows a photograph of the tin perovskite films prepared with tin iodide precursor. The manganese doped films were deposited with the same deposition and annealing parameters. For the solar cells, a different condition was utilized and will be stated later.

Figure 3.6 - Photograph of a tin perovskite sample (1 cm x 3 cm).

The sample synthesized with tin iodide will be referred to as $CH_3NH_3SnI_3$ or $MASnI_3$ throughout the thesis. The same applies to the doped samples prepared with tin iodide precursor: 2% Mn and 10% Mn.

Variant tin perovskites films were prepared using two non-halide precursors: tin(II) sulfate and tin(II) octoate. They were deposited by drop casting. The reason for using drop casting was to ensure the stability of the films during calcination. It was observed that when the films were spin coated using the halide perovskite conditions, their thermal stability was poor. Thus, the effects of temperature and time on the properties of these perovskites were studied: 110 ^{o}C/10 min, 150 ^{o}C/10 min and 150 ^{o}C/20 min.

The samples were named $CH_3NH_3SnI_3$ (sulfate) or $MASnI_3$ (sulfate) and $CH_3NH_3SnI_3$ (octoate) or $MASnI_3$ (octoate).

3.1.9 Preparation of the perovskite electrodes

For the electrochemical analysis of the Mn doped and pristine perovskite samples (tin iodide precursor), electrodes were prepared using one-step method (1000 rpm/ 30 s). The electrode area was limited to 1 cm^2. Two types of electrodes were prepared according to type of electrochemical measurement (aqueous and non-aqueous).

For aqueous medium, the films were protected by a polylactic acid film.

For this purpose, 245 mg of polylactic acid (PLA) was dissolved in 4 mL of dichloromethane at room temperature. This solvent was chosen because it dissolves PLA but does not dissolve the perovskite. The PLA solution was deposited and spin coated onto the perovskite film at 1000 rpm/30 s in a glovebox. In total, two layers were deposited and the films were dried at room temperature.

No PLA solution was deposited on the films utilized for the non-aqueous test. The films for the non-aqueous electrochemical analysis were deposited by drop casting instead of spin coating due to their high susceptibility of dissolving when in contact with the electrolyte solution. Therefore, drop casting guarantees a greater film thickness and stability. To ensure that all the non-aqueous films present the same width, a constant volume was utilized.

3.1.10 Fabrication of solar cells

Photovoltaic devices were fabricated in the Nanotechnology and Solar Energy Laboratory (LNES), University of Campinas. They were formed of multiple film layers: dense TiO_2, mesoporous TiO_2, perovskite layer, poly (3-hexylthiophene) and gold contact. Figure 3.7 shows the configuration of the solar cell.

Figure 3.7 - Design of the photovoltaic cell.

3.1.10.1 Etching of FTO

A part of the conductive FTO film was etched to prevent direct contact between the anode and cathode contacts during device testing. When this happens, the cell is short-circuited.

In order to perform the etch, four-fifth of the conductive layer was masked with a Kapton tape known for its high chemical and heat resistance. One-fifth was

exposed for etching. Zinc powder was mixed with distilled water to form a paste, which facilitates painting of the desired area. The paste was spread on the exposed surface and 2 M of hydrochloric acid was dropped on the surface. The etching process produced visible bubbles (hydrogen). After the reaction was complete, the substrate was washed off any zinc powder residue with distilled water. Then, the etching process was confirmed by a voltmeter.

The substrate was thoroughly cleaned by a soft bristle brush and Hellmanex detergent solution. A different procedure was adopted for the cleaning of the solar cell substrates because they are highly sensitive to residues. They were initially immersed in a piranha solution (3:1, H_2SO_4:H_2O_2) for 10 min to ensure the complete removal of organic residues. Although there exists a possibility of etching the FTO substrates, studies that used the method did not report any associated problems [208]–[210]. The substrate was washed with distilled water followed by ethanol and isopropanol. Finally, the cleaned substrate was submitted to UV-ozone cleaning for 30 min.

3.1.10.2 Dense TiO_2 layer

The first layer of the electron transport layer was TiO_2. Dense TiO_2 films were deposited by spray pyrolysis (oxygen). The precursor solution was composed of acetylacetone, titanium diisopropoxide bis(acetylacetonate) and ethanol. For the preparation, acetylacetone (0.4 mL) was added to ethanol (9 mL). Subsequently, titanium diisopropoxide bis(acetylacetonate) (0.6 mL) was added to the mixture to form the precursor solution [211]. After the precursor was deposited, a cotton swab soaked with isopropanol was swiped to remove a portion of the deposited film on the FTO glass. The as-prepared film was heated on a hotplate at 125 ^oC for 10 min, then cooled to room temperature.

3.1.10.3 Porous TiO_2 layer

The second layer of the electron transport layer was mesoporous TiO_2. To deposit the porous layer, a solution of 150 mg of titanium paste in 1 mL of ethanol was utilized. The solution was spin coated onto the dense TiO_2 layer at 4000 rpm for 60 s. Once again, a portion of the deposited film was wiped off from the FTO

glass. The substrate was dried at 120 ºC and was later calcined according to the conditions reported by Saliba et al. (2018) and are summarized in Table 3.2 [211].

Table 3.2 - Temperature and time conditions utilized for the calcination [211].

Ramp (min)	5	15	5	5
Temperature (ºC)	125	325	375	450
Hold (min)	5	5	30	5

3.1.10.4 Perovskite layer

The films were deposited by the one-step method. The precursor solutions for the cells were modified compared to the original solutions. Instead of DMF, a mixture of DMF and DMSO (4:1) in volume was utilized in order to improve the morphology and coverage of the films. The prepared precursor solutions were deposited on the TiO_2 assembly (porous and dense films) by spin coating.

The parameters of the spin coating process were: a slow step (10 s at 1000 rpm) which guarantees the coverage of the substrates and a fast step (20 s at 6000 rpm). Chlorobenzene was dropped casted on the actively rotating substrate at 5 s into the end of the 6000 rpm rotation. The films were heated at 100 ºC for 5 min instead of 150 ºC/10 min due to film degradation. Degradation was not previously observed for the condition of 150 ºC/10 min in the films not utilized for the solar cells and prepared with low spin coating speed (1000 rpm). Thus, degradation could be associated with film thickness.

3.1.10.5 Hole transport material

Poly(3-hexylthiophene) was utilized as a hole transport material instead of spiro-OMeTAD because Li reagents used as dopants have been reported to degrade perovskites. The solution was prepared by dissolving 10 mg of P3HT in 1 mL chlorobenzene. It was left overnight under agitation at 60 ºC and was deposited at room temperature. The hole transport material was deposited following the same spin coating conditions of the perovskite films. A cotton swab soaked with isopropanol was employed to remove a portion of the deposited film on the FTO glass.

3.1.10.6 Anode

Gold was used as a back contact to complete the device. The gold layer was deposited in two steps: the first was 2 nm layer at 0.1 Å/s, which was increased to 80 nm at 1.2 Å/s [211]. Figure 3.8 shows the as-prepared photovoltaic cell.

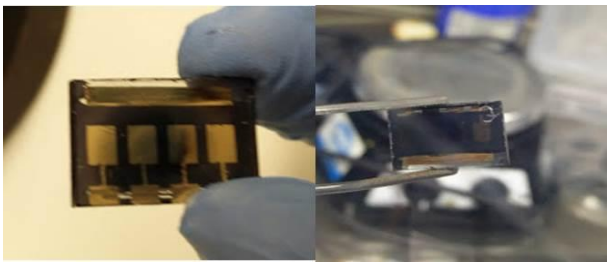

Figure 3.8 - The photograph of the as-prepared photovoltaic cell.

3.1.11 Sythesis of oxygen-deficient

The effect of titanium isopropoxide volume on the synthesis of oxygen-deficient TiO_2 was analyzed. For this purpose, 5 mL of titanium isopropoxide was dissolved in 60 mL of isopropanol under vigorous stirring at room temperature. Subsequently, 0.4 mL of 2 M HCl was added to the mixture and stirred for 20 min. The sample was designated 5Ti. The method was modified using 10 mL, 20 mL and 40 mL and the samples were named accordingly: 10Ti, 20Ti and 40Ti. Figure 3.9 shows the dispersions containing different volumes of titanium isopropoxide.

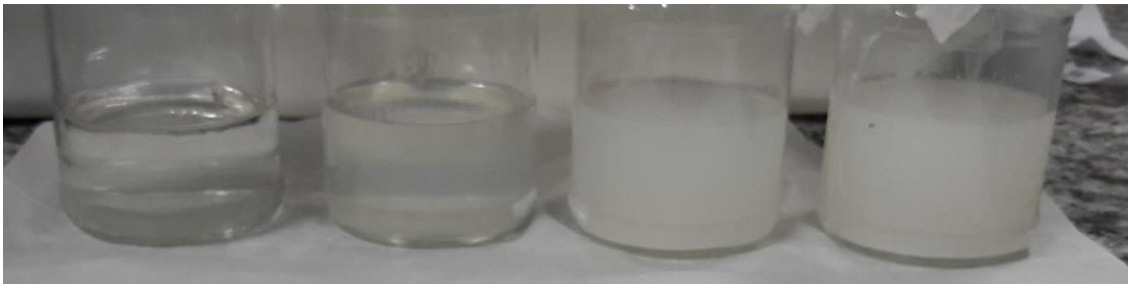

Figure 3.9 - Photograph of TiO_2 dispersion in ascending order of titanium isopropoxide volume (5-40 mL).

It can be seen that the samples undergo different degrees of hydrolysis/precipitation as the volume of titanium isopropoxide increases from 5 mL to 40 mL. Each dispersion was calcined separately in air using a two-step program: 150 ^oC/4h and 500 ^oC/4h in air with a ramp of 2 ^oC/min.

Part of the as-prepared sample 40Ti was separated and additional 3 step

heat treatments were carried out: 300 ºC/2h, 500 ºC/2h and 800 ºC/4h. This sample was named 40Ti_W due to its white color and served as a comparison.

3.1.12 TiO_2 electrodes

In order to measure the electrochemical properties of the powders, electrodes were fabricated through electrophoretic deposition. In this method, particles are deposited on a conductive surface such as FTO substrate under the influence of an applied potential. A stock suspension was prepared containing TiO_2 powder, ethanol and iodine with the proportion of 50 mg, 30 mL and 20 mg, respectively. Iodine increases the charge of the particles, facilitating deposition.

Two FTO substrates were immersed in the stock solution, one connected as an anode and the other, a cathode. A voltage of 12 V was applied for 15 min and then the charged particles were deposited on the cathode. Figure 3.10 shows the electrodes prepared by electrophoretic deposition.

Figure 3.10 - Photograph of the films deposited by electrophoresis. Left to right (5Ti-40Ti_W).

3.1.13 Characterization of perovskites and oxygen-deficient TiO_2

3.1.13.1 X-ray diffraction

The structural phases of the perovskite films and TiO_2 powders were identified by X-ray diffraction using a Shimadzu XRD 6000 diffractometer (Embrapa Instrumentation, São Carlos) equipped with a Cu anode (λCu-Kα = 0.154 nm). The films were scanned in the 2theta range of 10-70 degrees at a scan rate of 2 degrees per minute. The patterns were indexed with the help of a crystallographic database (Joint Committee on Powder Diffraction Files-JCPDF), Match software and CIF files. The lattice parameters of the TiO_2 samples were obtained through Rietveld analysis using the General Structure Analysis System

(GSAS) software [212] and the EXPGUI interface [213]. The data utilized for the analysis was obtained by a fixed time scan mode, a preset time of 4 s and scan rate of 2 degrees per minute.

The as-synthesized samples (doped and pristine $MASnI_3$) were left on a laboratory counter for 24 hours. The diffraction patterns of the samples were taken after this period to verify stability.

3.1.13.2 Micro-Raman spectroscopy

Micro-Raman spectra of all samples were collected with a Horiba Jobin Yvon HR550 model spectrometer (LIEC, UFSCar) whose wavelength and radiation power is 514 nm and 7 mW, respectively. This technique allows the chemical composition and identification of the samples through vibrational modes.

3.1.13.3 Photoluminescence spectroscopy

Photoluminescence provides information on defect states, recombination and bandgap of materials. The photoluminescence spectra of the perovskite samples were collected by Shimadzu RF-5301 PC spectrofluorophotometer (Embrapa Instrumentation) in the spectral range of 650 to 900 nm at an excitation wavelength of 550 nm. For the oxygen-deficient TiO_2, a 355 nm laser beam (Cobolt/Zouk) was utilized. The luminescence of the samples were dispersed by a 19.3 cm spectrometer and analyzed by a Silicon Charged Coupled Deviced (Andor Kymera) (Department of Physics, UFSCar).

3.1.14 Fourier-transform infrared spectroscopy/Attenuated total reflection

The chemical properties of the surface of the perovskite samples were measured by Fourier transform infrared (FTIR) spectroscopy. The spectra were recorded from 4000 to 500 cm^{-1} range, at a resolution of 4 cm^{-1}, using a Bruker Vertex 70 spectrophotometer (Embrapa Instrumentation).

The susceptibility of the perovskite samples to degradation motivated the use of attenuated total reflectance (ATR) technique instead of KBr pellets.

For TiO_2 samples, KBr pellets were prepared. One (1) mg of TiO_2 powder was blended with 100 mg of KBr and the mixture was pressed into pellets for the measurements.

3.1.14.1 Transmission electron microscopy

Crystallographic, compositional and morphological information was obtained by Transmission electron microscopy (TEM), using a FEI Tecnai G2 F20 microscope operated at 200 kV (LCE, UFSCar). The perovskites analyzed were $MASnI_3$ and 10% Mn. For sample preparation, the prepared film on FTO glass was scrapped and dispersed in dichloromethane. Drops of the suspension were deposited on a copper grade followed by drying in a desiccator. High resolution transmission electron micrographs were obtained and Energy-dispersive X-ray analysis was performed.

Given the high propensity of perovskites for degradation, an alternative deposition method was tested. Here, instead of dissolving the samples in dichloromethane, the films were scrapped and ground. After, the grid was placed in contact with the perovskite powder to pick debris for analysis. The new samples were analyzed in a Philip CM-120 transmission electron microscope. Selected area diffractions for crystallographic analysis were obtained.

To prepare the TiO_2 samples, they were dissolved in acetone and ultrassonicated for 10 min. The solution was then drop casted on the grid and dried. The d spacings were estimated with ImageJ software.

3.1.14.2 Diffuse reflectance spectroscopy

Diffuse reflectance spectroscopy (DRS) measurements were conducted with a UV-Vis spectrophotometer (UV-2700 Shimadzu, Embrapa Instrumentation and Department of Physics, UFSCar) in the range of 200 to 800 nm. MgO powder was used as a reflectance standard. The data were transformed to a Kubelka-Munk function using the Shimadzu software. The function is represented in Equation 3.4:

$$F(R) = \frac{(1-R)^2}{2R} = \frac{K}{S} \tag{3.4}$$

where R = reflectance, K = absorption coefficient and S = scattering factor.

The Kubelka-Munk function is almost identical to absorbance. The function can be modified by exponents depending on type of bandgap, where direct and indirect types are defined as 2 and 0.5, respectively. The bandgap value can be extrapolated from the x intercept of the plot.

3.1.14.3 Scanning electron microscopy

The morphology of the perovskites and TiO_2 samples was verified by Scanning electron microscopy (JEOL 6510, Embrapa Instrumentation) and Field Emission Gun Scanning microscopy (JEOL 6700, Embrapa Instrumentation), respectively. The TiO_2 powders were deposited in acetone and ultrasonicated for 10 min. After, an aliquot was dropped on the grid and dried.

The perovskite films were analyzed directly on their substrates. EDX elemental analysis was conducted for the perovskites samples ($MASnI_3$, 10% Mn, $MASnI_3$(Octoate) and $MASnI_3$(Sulfate)).The width of the 10% Mn/PLA film was measured by cross-sectional SEM using JSM7500F model microscope (Unesp, Araraquara).

3.1.14.4 Electrochemical analysis

A three-electrode system was utilized for the electrochemical tests, which consisted of a Pt counter electrode, Ag/AgCl/saturated KCl reference electrode and perovskite working electrodes (1 cm^2). Figure 3.11 shows the electrochemical cell with a volume capacity of 8 mL.

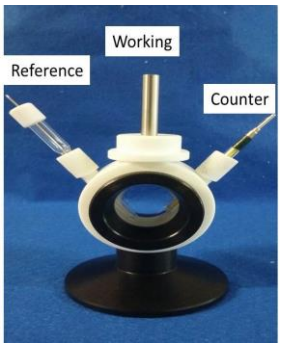

Figure 3.11 - Design of the photovoltaic cell and positions of the working, reference and counter electrodes.

Its configuration provides an air-tight environment. The electrolyte utilized was 0.1 M $NaSO_4$ in distilled water. The experiments were run without a redox pair to facilitate the observation of the pristine character of the perovskite.

For the non-aqueous measurements, a three-electrode system was utilized, however the reference electrode was a pseudo Ag wire immersed in tetrabutylammonium hexafluorophosphate ($TBAPF_6$)/dichloromethane solution and the working electrode was perovskite electrodes without PLA coating (1 cm^2). The electrolyte was 0.1 M $TBAPF_6$ /dichloromethane solution. The electrolyte solution was nitrogen saturated before any experiment and the solutions were changed for each electrode.

To determine the behavior of the samples under the application of different potentials as well as stability, cyclic voltammetry of the perovskite films was carried out from -0.8 V to 0.8 V at a rate of 0.1 V/s and -0.07 V applied potential. The measurement consisted of three cycles, however only the first cycle was analyzed as it truly represents the perovskite film. The IUPAC convention for oxidation and reduction was applied.

To study the effect of Mn on electron transfer, impedance measurements in the range of 10^5 Hz to 1 Hz was conducted. The applied potential was selected from a region in the cyclic voltammetry graph where no oxidation and reduction processes took place. The light source was an Osram halogen lamp at 110 W. Figure 3.12 shows the spectrum of the lamp utilized for the experiments.

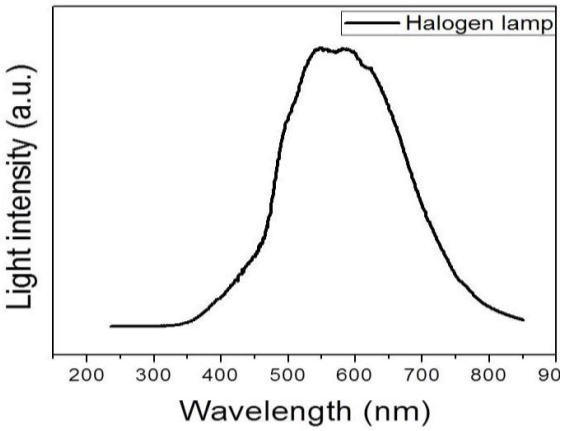

Figure 3.12 - Emission spectrum of the halogen light source.

The current and voltage needed for the analysis were provided by a potentiostat (AUTOLAB PGSTAT® 30) available at Embrapa Instrumentation.

Linear sweep voltammetry under dark and light conditions was conducted in two directions (negative and positive). Also, transient photocurrent measurements were conducted with intervals of 10 s for a period of 90 s. Finally, chronoamperometry measurements (300 s) were conducted to verify the stability of the films.

For the TiO_2 electrodes, impedance measurements in the frequency range of 10^5 Hz to 0.1 Hz and transient photocurrent measurements (90 s) in light and dark conditions were carried. A three-electrode system was utilized consisting of a Pt counter electrode, Ag/AgCl/saturated KCl reference electrode and TiO_2 working electrodes (1 cm^2). The electrolyte utilized was 0.1 M $NaSO_4$ in distilled water.

3.1.14.5 Contact angle

The wettability of the PLA polymer was tested by contact angle measurement using water in a CAM 101 Optical Contact Meter (System (KSV Instruments, Embrapa Instrumentation). Five (5) µL of water was dropped onto the films and the contact angle was measured automatically at a time interval of 60 s.

3.1.14.6 Electron paramagnetic Spectroscopy

To verify the presence of paramagnetic species related to oxygen vacancies, EPR measurement were taken in a Bruker EMS EPR Spectrometer. The powder samples were placed in individual tubes and filled to the same volume. The microwave frequency and power utilized was 9.51 GHz and 1.01 µW, respectively.

3.1.14.7 X-ray photoelectron spectroscopy

The surface chemical analyses of selected TiO_2 samples (5Ti, 20Ti, 40Ti and 40Ti _W) were performed with a PHOIBOS 150 spectrometer equipped with a XR-50 twin anode X-ray source (Mg/AI, 1.2-1.4 KeV). Wide survey and high resolution spectra (C 1s, O 1s and Ti 2p) were recorded. Fifteen scans were used for the survey spectra, while high-resolution spectra were recorded with 25 scans.

They were fitted and quantified using Casa XPS software. The C1s peak at 286.4 eV for hydrocarbon contamination was used as a reference. The measurement was carried out at INT Nanotechnology Characterization Center, Rio de Janeiro.

3.1.14.8 J-V curves

The J-V curves of the perovskite solar cells were obtained using a Keithley 2400 SourceMeter under AM 1.5G (100 mW/cm^2) illumination inside a glovebox maintained at room temperature. The illumination intensity was set with a Sciencetech Class AAA simulator and calibrated with a KG5 filtered silicon reference cell. The J-V curves were obtained in the forward and reverse modes with a step of 10 mV and delay time of 0.25 s. However, only the reverse scan was presented because of hysteresis. The values of the open-circuit voltage (Voc), current density (Jsc) and fill factor (FF) were extracted from the curves. After, the power conversion efficiency (PCE) was estimated.

3.2 Photocatalytic test

The TiO_2 samples were tested for their ability to degrade aqueous Amiloride solution. All photocatalytic tests were conducted in a photocatalytic reactor available at Embrapa Instrumentation, São Carlos (Figure 3.13). The photoreactor is equipped with six lamps (interior) and connected to a thermostatic bath and fan for temperature regulation. The efficiency of the films in degrading Amiloride under visible light was evaluated.

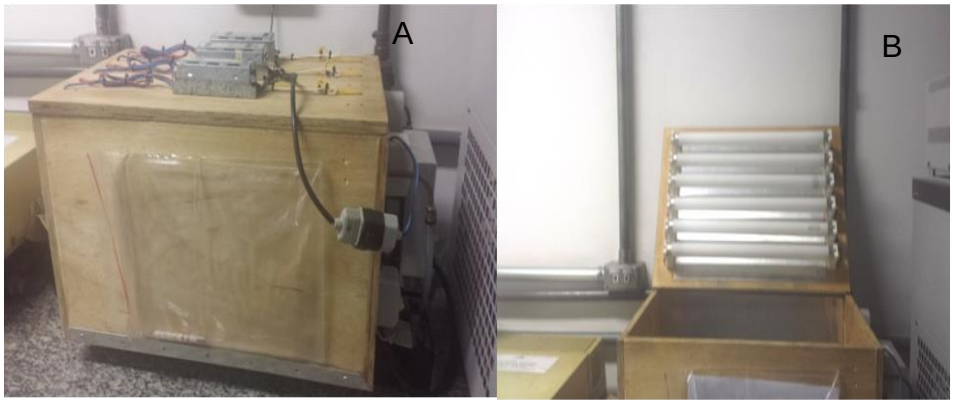

Figure 3.13 - Photoreactor A) closed and B) open.

The test solution was Amiloride solution (5 mg/L). Each sample (10 mg)

was placed in a beaker containing 20 mL solution of Amiloride (5 mg/L). A similar solution was also prepared however without TiO_2, which served as a blank.

The solutions were placed in the photoreactor and irradiated with visible light (6 Quality 15 W lamps, with maximum intensity at 440 nm). The measurement time was 4 hours. Aliquots of 3 mL were taken from each solution in intervals of 1 hour for UV-vis measurements (Shimadzu-UV-1601 PC spectrophotometer). After the runs, the aliquots were returned into the beakers for further irradiation. Amiloride has three principal peaks and the peak at 363 nm was monitored.

4 RESULTS AND DISCUSSION

4.1 Tin and Mn doped perovskites

4.1.1 Phase analysis

Figure 4.1 shows the X-ray diffraction patterns of FTO, $CH_3NH_3SnI_3$ ($MASnI_3$), 2% and 10% Mn doped $CH_3NH_3SnI_3$ and their respective precursors, CH_3NH_3I and $MnCl_2$.

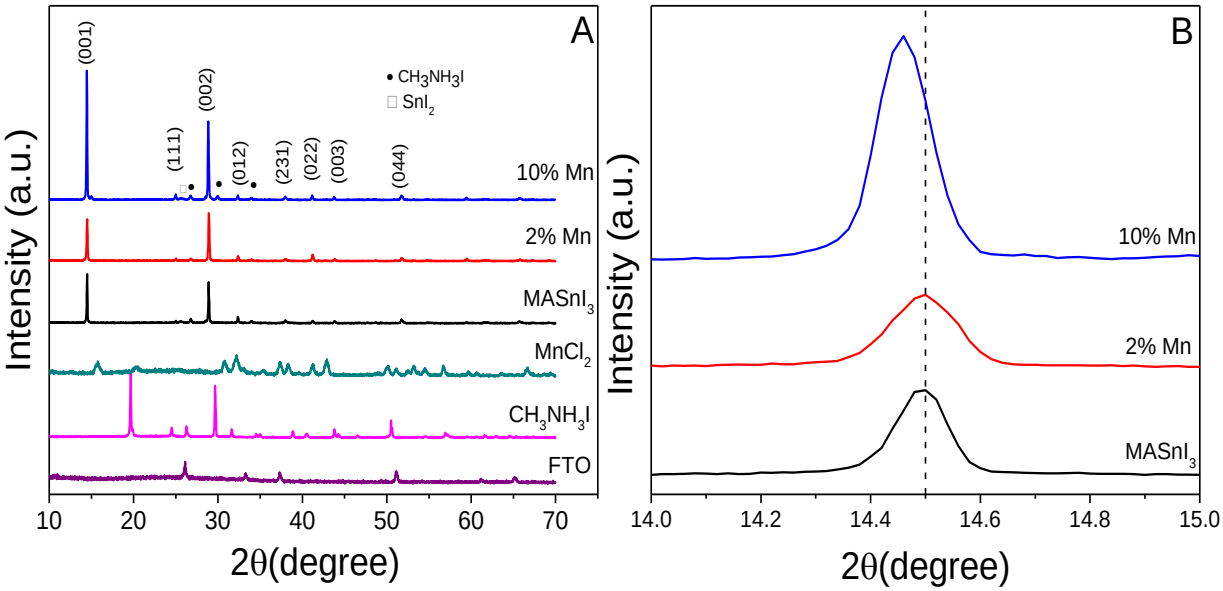

Figure 4.1 - X-ray diffraction patterns of the precursors ($MnCl_2$, CH_3NH_3I), FTO and $MASnI_3$, 2% and 10% Mn doped $MASnI_3$ annealed at 150 °C/ 10 min.

The diffraction patterns reveal that $MASnI_3$ is composed of the pseudocubic phase [3][94][214]. The intensities of the (001) and (002) peaks were higher as expected but that of the remaining peaks were distinctively low, which point to a form of preferential orientation parallel to the substrate surface, similar to other studies [163][29].

The deposition of the films on bare FTO substrate compared to TiO_2 might favor specific planes [140]. Kim et al. (2016) found that annealing temperature and the amount of residual solvent after spin coating influenced the growth of (100)-oriented lead perovskite films [215]. Thus, it is possible that the low rotational speed used in the present experiment may be associated with the nature of the diffraction patterns. Minor traces of unreacted methylammonium iodide and SnI_2 can be seen but did not affect phase formation. The diffraction patterns of $MASnI_3$ did not alter significantly with the incorporation of Mn. In fact,

the doped films were crystalline and the pseudocubic phase was retained. According to the XRD resolution, $MnCl_2$ peaks or associated secondary phases were absent, strengthening the assumption that doping does not disrupt the stoichiometry and structure of the perovskite, considering the compositions studied.

To back this assumption, the Goldschmidt tolerance factor (Equation 4.1) was calculated using the weight fraction of the Mn and Sn constituents according to Equation 4.2, where r_{MA}, r_I, r_{Sn} and r_{Mn} represent the radius of methylammonium cation, iodide ion and B cations (Sn(II) and Mn(II)), respectively [216]. For the calculation, the following ionic radii were considered: Mn(II) (0.8 Å) [21], methylammonium (1.80 Å) [217], iodide ion (2.2 Å) [83] and Sn(II) (1.18 Å) [20].

$$t = \frac{r_{MA} + r_I}{\sqrt{2}(r_B + r_I)} \quad (4.1)$$

$$r_B = Xr_{Mn} + (1 - X)r_{Sn} \quad (4.2)$$

The values were 0.84, 0.84 and 0.85 for $MASnI_3$, 2% Mn and 10% Mn, respectively. In this range, the perovskite is stable. Also, there is a subtle increase in stability when $MASnI_3$ is doped with 10 % Mn. To probe the effect of Mn doping on the octahedral structure of $MASnI_3$, the octahedral factor was also calculated. The ratio of the ionic radius of the metal cation to halide, deduced by Equations 4.3 and 4.4, must be equal or greater than 0.414 [88].

$$\mu = \frac{r_B}{r_I} \quad (4.3)$$

$$r_B = Xr_{Mn} + (1 - X)r_{Sn} \quad (4.4)$$

From the calculations, the octahedral factors were 0.54, 0.53 and 0.52 for $MASnI_3$, 2% and 10% Mn doped $MASnI_3$, respectively. The octahedral factor decreases as Mn content increases from 2 to 10 mol% Mn, representing a distortion of the crystal structure. To analyze the distortion induced by Mn doping, the (001) plane was considered.

Figure 4.1 B presents the (001) peak of the pristine and Mn doped perovskites. A negligible peak shift can be seen for 2% Mn compared to $MASnI_3$, indicating subtle changes in crystal structure. For 10% Mn doped $MASnI_3$, the (001) peak shifted to a lower theta value. A shift to lower theta angles implies increase in d spacing, in other words, lattice expansion. Lattice expansion in

some Mn doped lead perovskites was associated with Mn in interstitial positions [218][219]. A major source of unreliability as regards predicting the position of Mn (0.8 Å) is the rapid oxidation of Sn(II) (1.18 Å) to Sn(IV) (0.69 Å), which opens the possibility of Mn occupying both substitutional and interstitial positions.

In this work, X-ray diffraction patterns were taken of fresh and aged films (24 hours in air) (Figure 4.2). In general, the broadening of the peaks after 24 h depicts the loss of phase crystallinity associated with degradation.

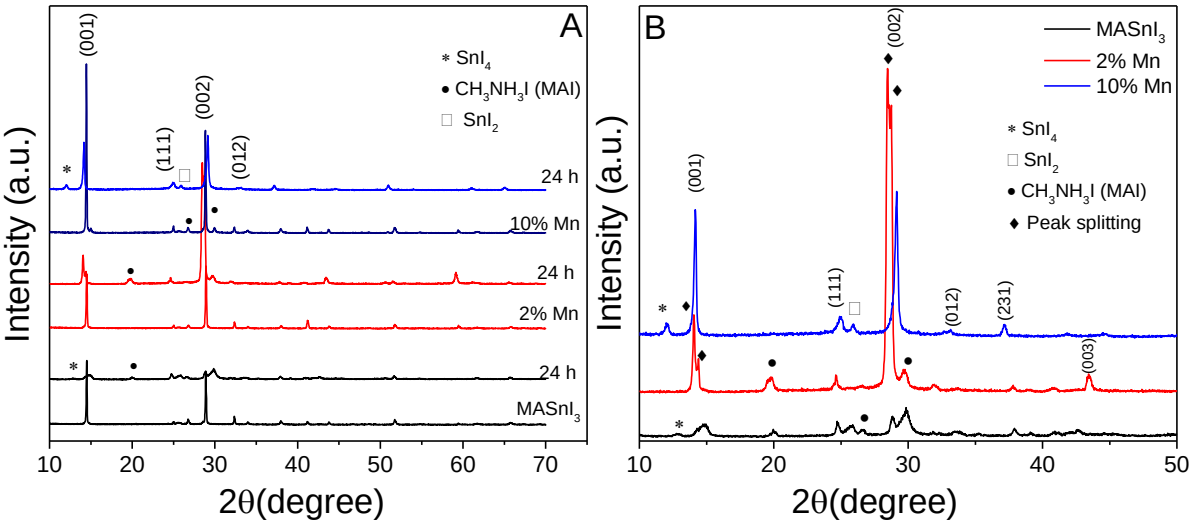

Figure 4.2 - X-ray diffraction patterns of the fresh and aged (24 hours) samples ($MASnI_3$, 2% Mn and 10% Mn).

The main mechanism behind phase degradation among the samples is considered oxidation as evidenced by the presence of SnI_4. After 24 h in air, there was a decrease in the intensity of the (001) peak for all samples: $MASnI_3$ (~94 %), 2% Mn (~80%) and 10% Mn (~74%). The reduction can be associated with the loss of crystallinity via phase degradation. Given that the main degradation mechanism of tin perovskites is Sn oxidation compared to methylammonium degradation, the reduction of the principal (001) and (002) peaks is presumed to be controlled by Sn oxidation. As a result of oxidation, tin vacancies can be formed to maintain charge balance [26][27]. The lower intensity of the (001) principal peak observed for $MASnI_3$ compared to the Mn doped samples shows that Mn can improve phase stability through tin compensation [26][27]. For 2% Mn, (001) peak splitting is observed. It can be associated with changes in symmetry and phase transformation [220]–[222]. The result suggests that 2% Mn

adopts a lower symmetry phase to reduce the extent of degradation.

In relation to the (002) peak, its intensity decreased in $MASnI_3$ (~88%) and 10% Mn (~54%), pointing to lower crystallinity due to phase degradation. In contrast, the intensity increased for 2% Mn (~82%) and peak splitting (♦) was observed. Assuming that the Mn content of the doped perovskites is maintained during degradation, it can aid in the formation of secondary phases and/or stabilization of some planes (002) as observed for 2% Mn compared to the pristine sample. The peak splitting of the (002) peak in 2% Mn reinforces changes in symmetry and possible phase transformation with degradation.

The (001) and (002) peaks in 10% Mn did not undergo splitting compared to 2% Mn. It is probable that a higher level of $MnCl_2$ may have compensated for tin vacancies, inhibiting the reduction of symmetry. Another possibility is the increased bond strength between methylammonium and the inorganic cage with increased Mn levels.

4.1.2 Micro-Raman

Figure 4.3 shows the micro-Raman spectra of $MASnI_3$, 2% Mn and 10% Mn doped $MASnI_3$.

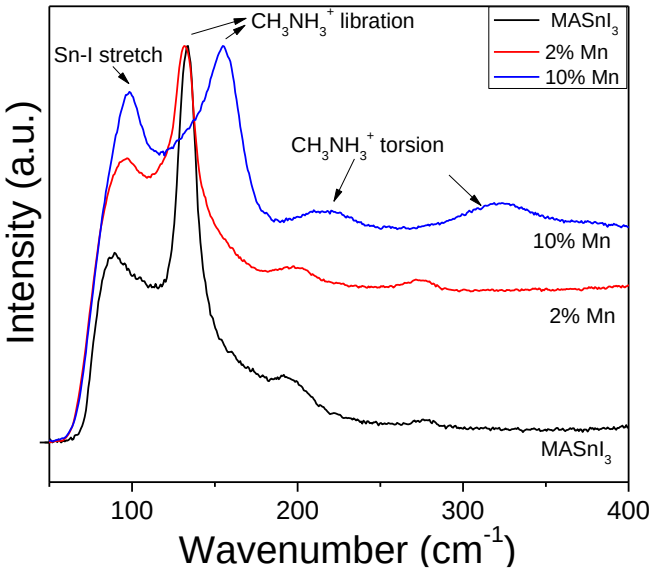

Figure 4.3 - Micro-Raman spectra of $MASnI_3$, 2% and 10% Mn doped $MASnI_3$.

Peaks at 89, 96 and 98 cm^{-1} can be seen in $MASnI_3$, 2% and 10% Mn, respectively. They were assigned to Sn-I vibration and the shift to higher

frequencies highlights the influence of Mn doping on the SnI_6 octahedra [223][224]. The substitution of Sn for Mn, a lighter atom, tends to increase vibrational frequency. Alternatively, the shift could be related to compression of the inorganic cage, which supports distortion as predicted by the change in octahedral factor.

Three peaks can be seen in the region above 120 to 350 cm^{-1} and are ascribed to the librational and torsional modes of methylammonium cations [225][226]. For $MASnI_3$ and 2% Mn, the methylammonium librational modes centered around 134 and 131 cm^{-1}, respectively, are comparable [226]. This emphasizes that Mn doping at 2 mol% did not significantly modify the properties of the perovskite. However, the librational mode peak in 2% Mn perovskite appears broader than that of $MASnI_3$, pointing to an increase in disorder. Thus, the presence of Mn can induce bond modification which may contribute to stability.

For 10% Mn, the librational mode is at 150 cm^{-1}, which is higher compared to the $MASnI_3$ and 2% Mn samples. Considering that methylammonium is connected to the inorganic Sn-I cage through N-H bonds, atoms such as Mn and/or chlorine (from $MnCl_2$) can cause the distortion of the Sn-I octahedral with consequent shift in the librational mode [85][227]. The regions above 200 cm^{-1} are known for torsional modes of methylammonium [226]. In general, the modes shift to higher frequencies with Mn doping. The broader nature of the peaks in the doped samples compared to the pristine perovskite highlights higher disorder due to Mn doping.

4.1.3 Fourier-transform infrared spectroscopy/Attenuated total reflection

Figure 4.4 shows the spectra of $MASnI_3$, Mn doped $MASnI_3$ (2 and 10% Mn) and methylammonium iodide (CH_3NH_3I) in the range of 400-4000 cm^{-1} . All the vibrational modes were associated with the organic component of the perovskite. The bands corresponding to the inorganic component appear at very low wavelengths, below 100 cm^{-1}, which were not covered in the analysis [224].

In the functional region, three main bands were identified for $MASnI_3$: two broad peaks (3421 and 3088 cm^{-1}) and a sharp peak (1645 cm^{-1}). They were

assigned to symmetric N-H stretching and/or O-H stretching, asymmetric N-H stretching and NH_2 bending, respectively [224][228][229].

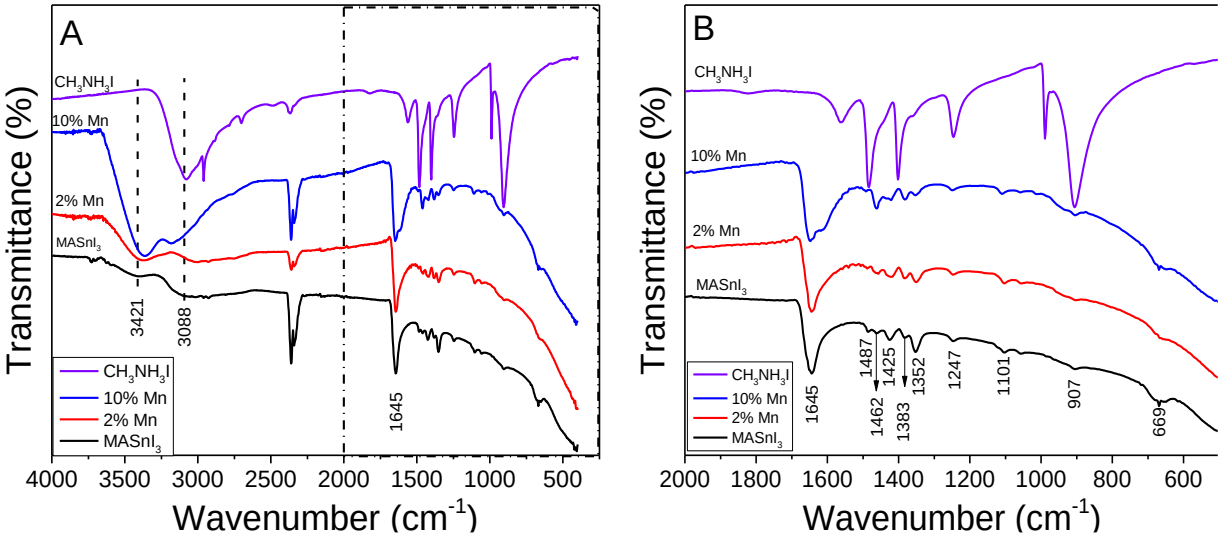

Figure 4.4 - A) FTIR-ATR spectra of methylammonium iodide (CH_3NH_3I, $MASnI_3$, 2% and 10% Mn doped $MASnI_3$ and B) Extended view of the region from 2000 and 500 cm^{-1}.

The N-H and/or O-H stretch band shifts to lower values with increase in Mn doping, a sign of changes in hydrogen bond. The presence of these bands in the perovskites compared to methylammonium iodide suggests changes in bonding associated with perovskite formation. The assymetric N-H and/or O-H band is located at a lower and higher frequency for 2 and 10% Mn, respectively, compared to the undoped perovskite. The shift to a higher frequency with 10% Mn can be correlated with increase in bond strength. The N-H bending band (1645 cm^{-1}) in both the pristine and doped samples is absent in methylammonium iodide, indicating its association with perovskite formation.

In the fingerprint region (1500-400 cm^{-1}), both the pristine and Mn doped perovskites have similar vibrational modes suggesting minimal changes in the with Mn doping: C-H deformation (1487 cm^{-1}), NH_3 bending (1462 and 1425 cm^{-1}), CH_3 bending (1383 and 1352 cm^{-1}), CH_3NH_3 rocking (1247 and 907 cm^{-1}), C-H wagging (1101 cm^{-1}) and N-H wagging (669 cm^{-1})[224][230]–[232]. Bands such as 1462 and 1425 cm^{-1} can be related to perovskite formation because they are absent in methylammonium iodide. The peaks and their respective assignments are presented in Table 4.1.

Table 4.1 - List of principal peaks and assignment.

Band (cm^{-1})	Assignment
3428	Symmetric N-H stretching and/or O-H stretching [228][229]
3088	Asymmetric N-H stretching [224]
1647	NH_2 bending [229]
1487	C-H deformation [231]
1462	Symmetric NH_3 bending [230][231]
1425	Symmetric NH_3 bending [224]
1383	Asymmetric CH_3 bending [224]
1352	Symmetric CH_3 bending [224]
1247	CH_3NH_3 rocking [224]
1106	C-H wagging [232]
907	CH_3NH_3 rocking [224]
667	N-H wagging [232]

The characteristic peaks in the fingerprint region were more pronounced for methylammonium iodide compared to the samples, once again demonstrating changes in surface bonds with perovskite formation. In general, the vibrational modes of the pristine perovskite were not significantly altered with doping.

4.1.4 Scanning electron microscopy

Figure 4.5 shows the morphology of $MASnI_3$ deposited by spin coating and annealed at 150 ^oC/10 min.

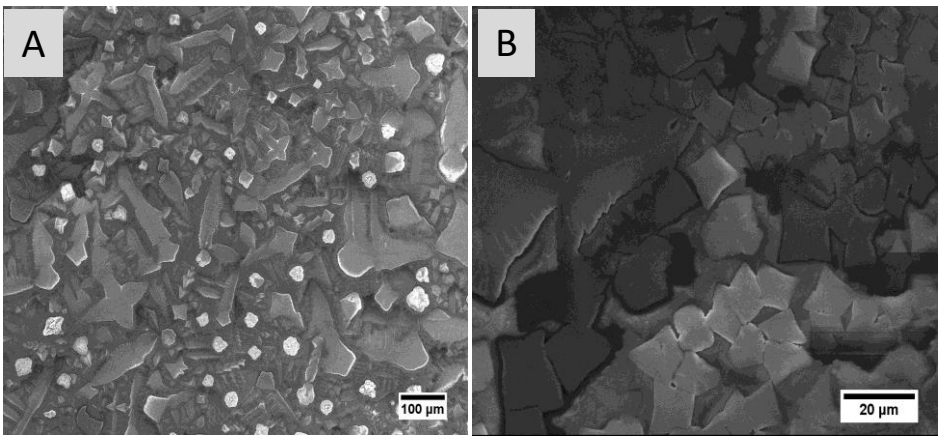

Figure 4.5 - A) SEM micrograph of $MASnI_3$ and B) Higher magnification.

The morphology is undefined and is composed of circular (bleached), cubic and cross-like grains. A reason for the undefined morphology is the inherent rapid crystallization of tin perovskites. The use of the one-step method without antisolvent dripping can accelerate the nucleation and crystallization of the perovskite from solution, leading to the formation of individual particles instead of grains. Grain boundaries are one of the main scattering point of charge carries, thus large grains are desired [233]. Figure 4.6 shows the EDX elemental mapping of the bleached region in the micrograph.

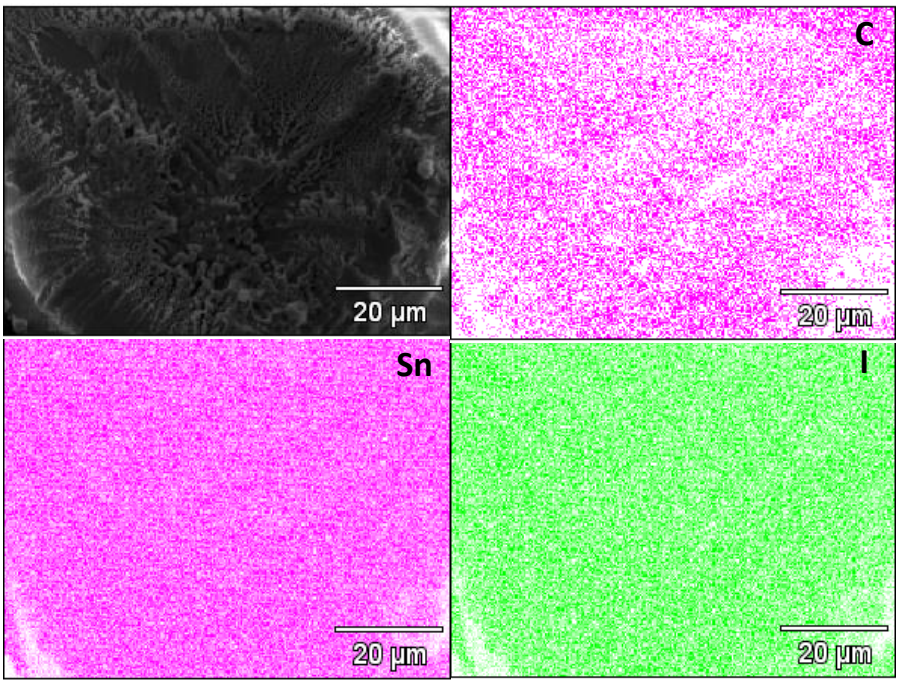

Figure 4.6 - EDX elemental mapping of $MASnI_3$ indicating the distribution of Sn, I and C at a selected region suspected of degradation.

The regions of the micrograph that appear bleached were investigated by energy dispersive X-ray (EDX) mapping. The distribution of Sn and I is satisfactory but carbon distribution is sparse, which can be related to the loss of the same.This shows that electron beams can induce perovskite degradation through carbon loss. Electron irradiation during TEM experiments was reported to cause the loss of halides [234].

Figure 4.7 presents the morphology of the 2% Mn doped perovskite. The morphology of $MASnI_3$ appear to improve with Mn doping because the cross-like morphology is visible but they are broader, resulting in grain boundaries. Thus, Mn may play a role in controlling nucleation and growth. The cross-like grains

appear to grow until they touch each other, intertwining into grain boundaries. It is interesting to note that the cross-like grains are formed by dentrite growth as shown in Figure 4.7 B.

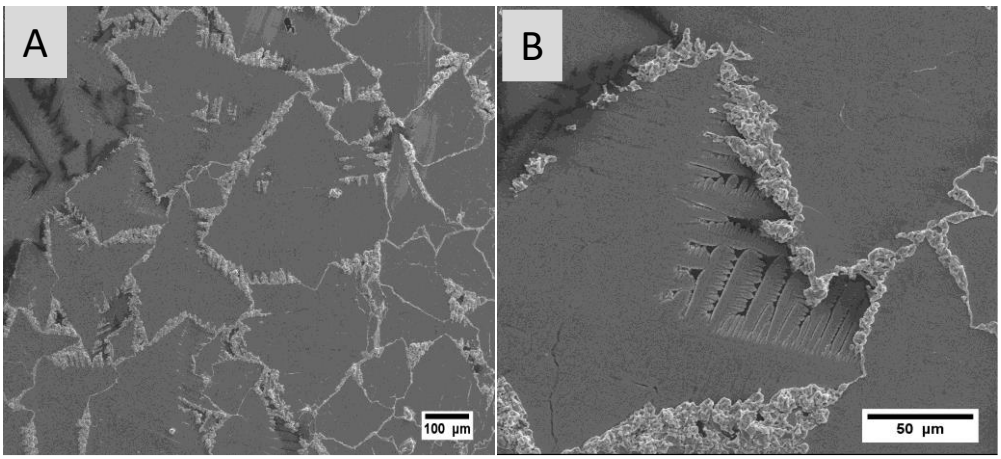

Figure 4.7 - A) Micrograph of 2% Mn doped $MASnI_3$ and B) magnification showing dendrites.

Dendrite formation have been observed in perovskites synthesized with the one-step synthesis method [235] and for conditions where solvent evaporation was slow [139][236]. The distribution of I, Sn and Mn in 2% Mn as per EDX mapping was satisfactory, highlighting the efficiency of the doping method (Figure 4.8). Furthermore, there was no apparent phase segregation.

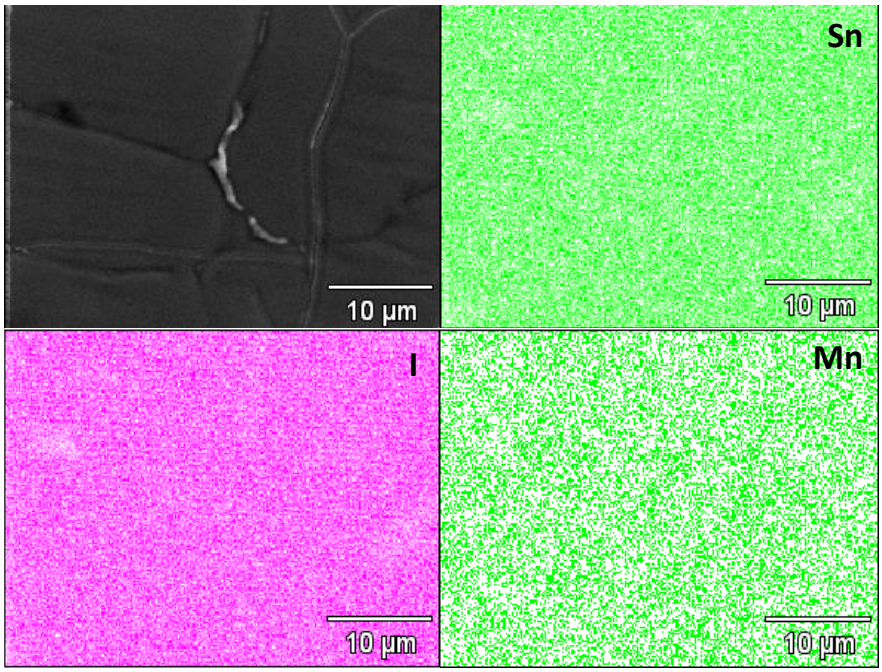

Figure 4.8 - Elemental mapping of 2% Mn doped perovskite showing the distribution of Sn, Mn and I.

The morphology of 10% Mn is shown in Figure 4.9. Similar to the micrograph of 2% Mn, the cross-like morphology is dominant but an increased number of dendrites can be seen, which implies that Mn may induce dendrite formation. The dendrites can be detrimental to efficiency since they can scatter electrons or serve as recombination centers.

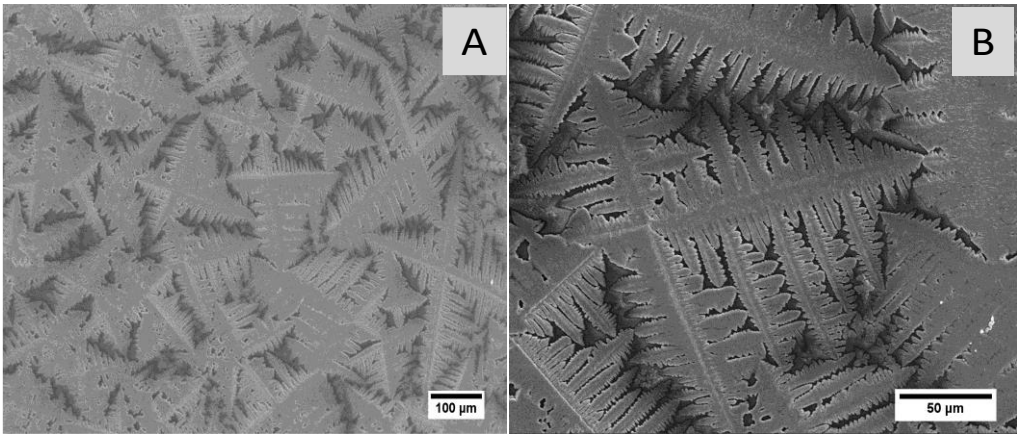

Figure 4.9 - A) Micrograph of 10% Mn doped $MASnI_3$ B) magnification showing dendrites.

An EDX mapping of the sample was performed to verify the distribution of Sn, I, C, Mn, I and Cl (Figure 4.10).

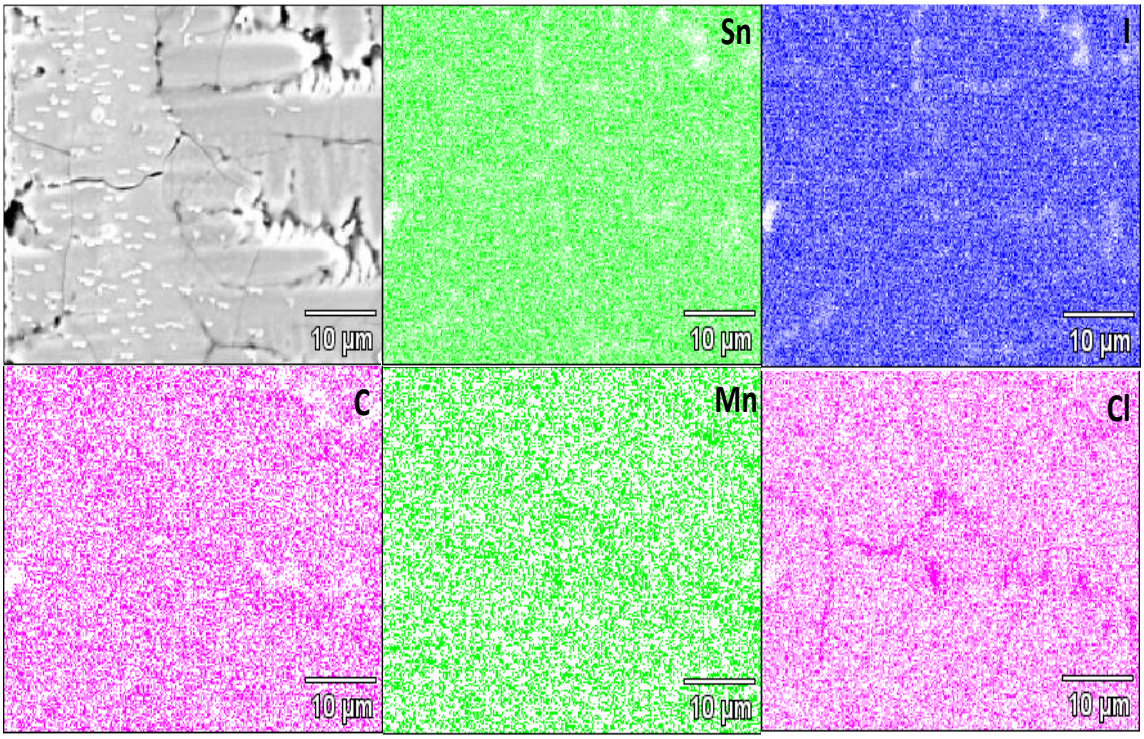

Figure 4.10 - Elemental mapping of 10% Mn doped perovskite showing the distribution of Sn, I, C, Mn and Cl.

The distribution of Sn, Mn, C and I is satisfactory despite the increase in Mn content. The absence of Mn segregation in the grain boundaries reinforce the doping method as simple and efficient. For chlorine, it was found that the same was not completely eliminated with the annealing conditions employed. Furthermore, it segregated around the grain boundaries. It is important to note that the level of Cl deemed detrimental or beneficial was not within the scope of the thesis. Thus, it is important to consider this fact when opting for $MnCl_2$ as a precursor for Mn doping.

4.1.5 Transmission electron microscopy

Figure 4.11 presents a dark field scanning transmission electron micrograph, high resolution transmission electron micrograph (HRTEM) and EDX spectrum of $MASnI_3$ prepared using dispersed powder in dichloromethane.

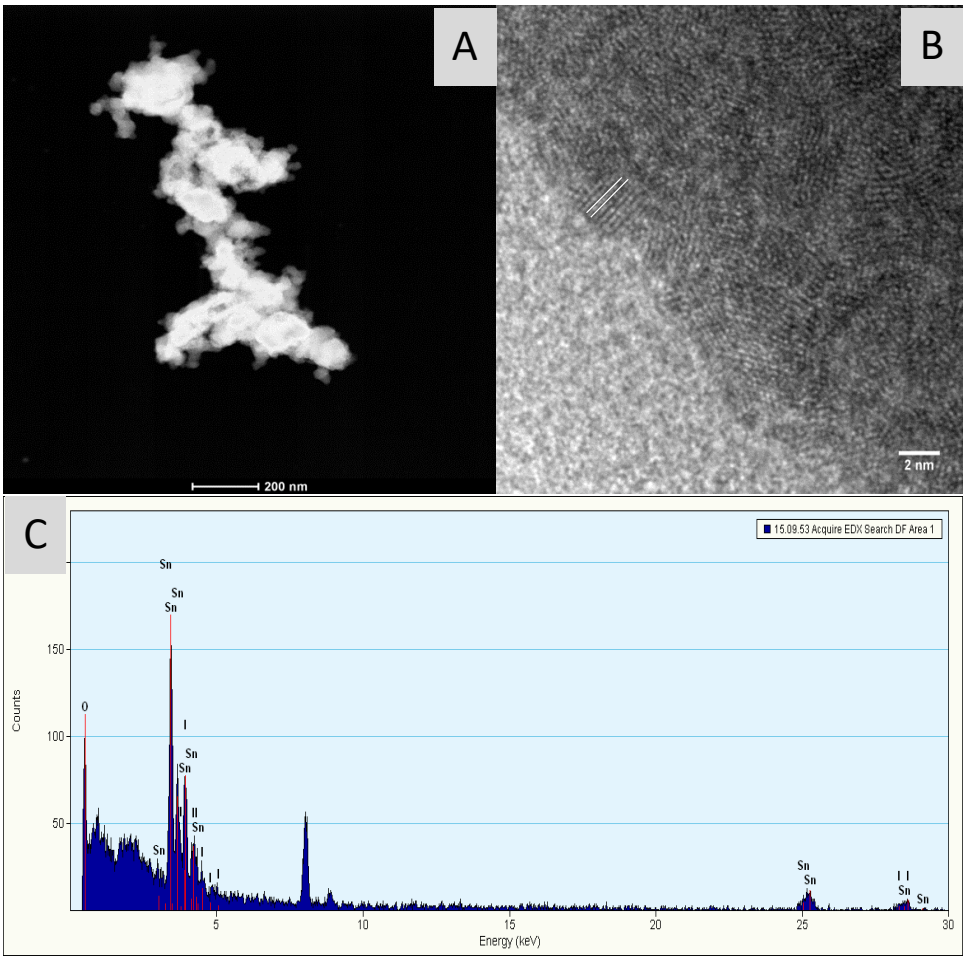

Figure 4.11 - A) Dark field image B) HRTEM image and C) EDX of $MASnI_3$.

The dark field image shows that the $MASnI_3$ powder is composed of

agglomerates of different sizes, ranging from as small as 30 nm to as large as 200 nm. The sample is considered partially crystalline due to the lattice fringes in Figure 4.11 A. The d spacing of the marked lattice fringe corresponds to 0.205 nm which is closer in value (0.208 nm) to the (122) plane [28]. The result confirms that the perovskite analyzed is not completely degraded by the electron beam.

From the EDX analysis, the presence of Sn and I atoms can be verified, however it is not a guarantee of the integrity of the perovskite. Although the sensitivity of EDX for quantification is limited, the atomic mass % of Sn and I was 17.32% and 3.39%, respectively, which suggests that the ratio of Sn: I is far from 1:3 as expected ($CH_3NH_3SnI_3$). In this case, there is the loss of I and Sn.

Figure 4.12 A shows the TEM micrograph of 10% Mn, where a contrast of tone can be observed.

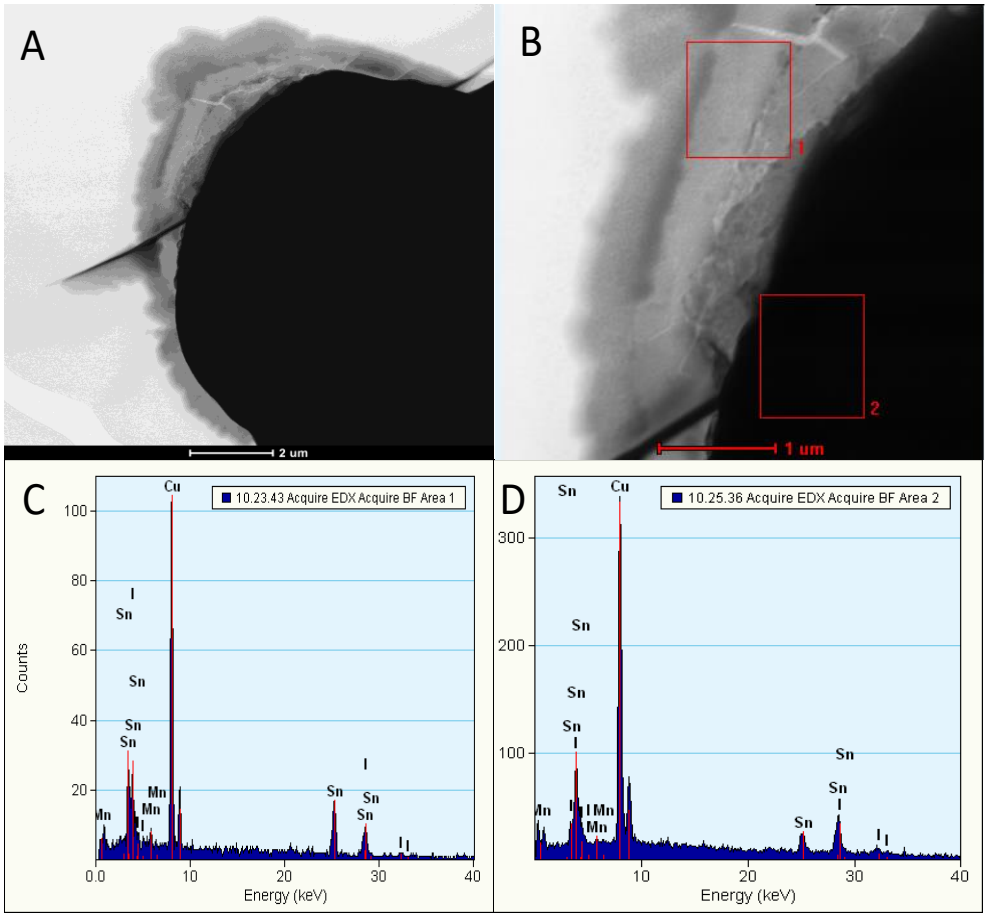

Figure 4.12 - A) Bright field image of 10% Mn, B) Bright field image with selected areas for EDX analysis, C) EDX spectrum of 10% Mn (Area 1) and D) EDX spectrum of 10% Mn (Area 2).

Figure 4.12 C and D presents the EDX of 10% Mn. The presence of Cu is

associated with copper from the TEM support grid. As can be seen from the spectra, both Sn and Mn are present in areas 1 and 2. The difference in contrast can be associated with crystallinity and/or thickness variation. The quantification (atomic %) of the elements shows that the bright region contains 4.17% of Mn, while the dark region contains no Mn atoms despite its presence in the spectrum.

This discrepancy is associated with the semi-quantitative nature of the technique. The quantity of Sn and I in atomic% is 41.48 and 54.35%, respectively. Thus, the ratio of Sn:I is 1:1.3. Contrary to the Sn perovskite, the loss of I and Sn seems to be closer in magnitude. Therefore, Mn could have a positive effect on the binding of Sn to I.

Diffraction images of the samples ($MASnI_3$ and 10% Mn) were obtained in a second attempt to analyze them by TEM. This time, the grid was passed over a ground powder sample to pick debris which can be analyzed.

Figure 4.13 shows the bright field image and diffraction image of $MASnI_3$. The morphology of the sample is more uniform with dispersed particles compared to when prepared with dichloromethane as previously shown in Figure 4.12. This could be because the powder was ground. A selected area diffraction of $MASnI_3$ presents rings indicative of a crystalline sample composed of many particles.

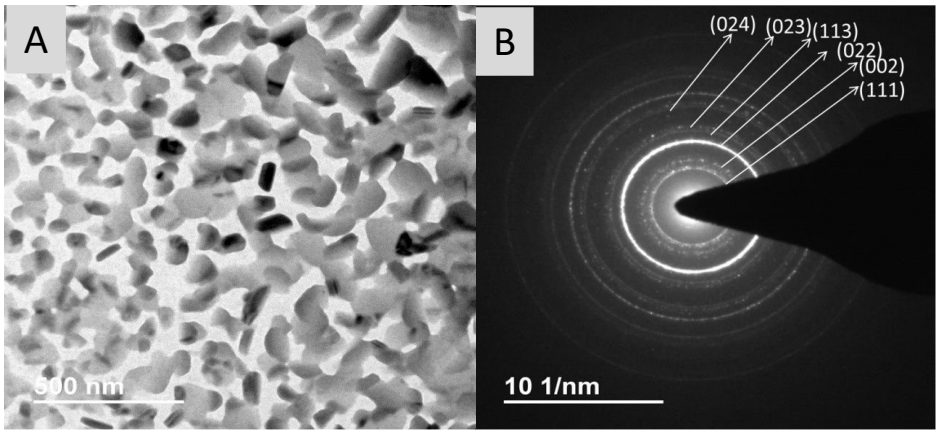

Figure 4.13 - A) Bright-field image and B) Ring diffraction pattern of $MASnI_3$.

The rings were indexed to the following planes in the order of decreasing d spacing according to specific crystallographic Information Files (CIF) of tin perovskites [3]: 0.36, 0.31, 0.22, 0.19, 0.17, 0.14 nm associated with (111), (002), (022), (113), (023) and (024), respectively. The unidentified rings had d spacings outside the range provided by the CIF documents. Based on the identified rings, it is plausible that the dry method of sample preparation contributes to sample

preservation.

Sample 10% Mn was analyzed by TEM. The bright field and diffraction images of 10% Mn are presented in Figure 4.14. The morphology of 10% Mn is different from the pristine perovskite, presenting a branch-like morphology (Figure 4.14 B). It is possible that Mn induces some form of directional growth of tin as speculated from the SEM images. The diffraction ring of the sample is presented in Figure 4.14 B.

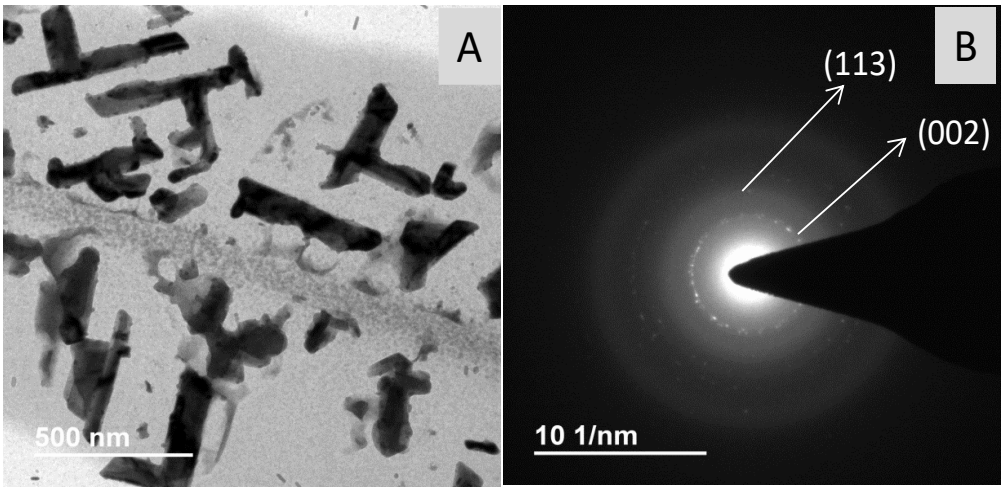

Figure 4.14 - A) Bright-field image and B) Ring diffraction pattern of the 10% Mn perovskite.

The image shows diffused rings as well as rings formed of particles. Therefore, the material is semicrystalline compared to the pristine perovskite. A d spacing of 0.29 nm was estimated from the first inner ring. It is closest in value to the (002) plane with a d spacing of 0.31 nm [3]. The second diffused ring was estimated to have a d spacing of 0.20 nm closest in value to the (113) plane with a d spacing of 0.19 nm [3].

The identified planes in the doped sample (10% Mn) are also present in the pristine sample. Thus, Mn doping does not disrupt the perovskite structure but modifies the d spacing of the planes.

4.1.6 Diffuse Reflectance

To study the optical properties of the samples, reflectance data were obtained by diffuse reflectance spectroscopy. Subsequently, they were transformed into Kubelka-Munk function which allows the extrapolation of

bandgaps. Figure 4.15 A and B shows the maximum absorption of the samples and their extrapolated bandgaps based on Kubelka-Munk plots, respectively.

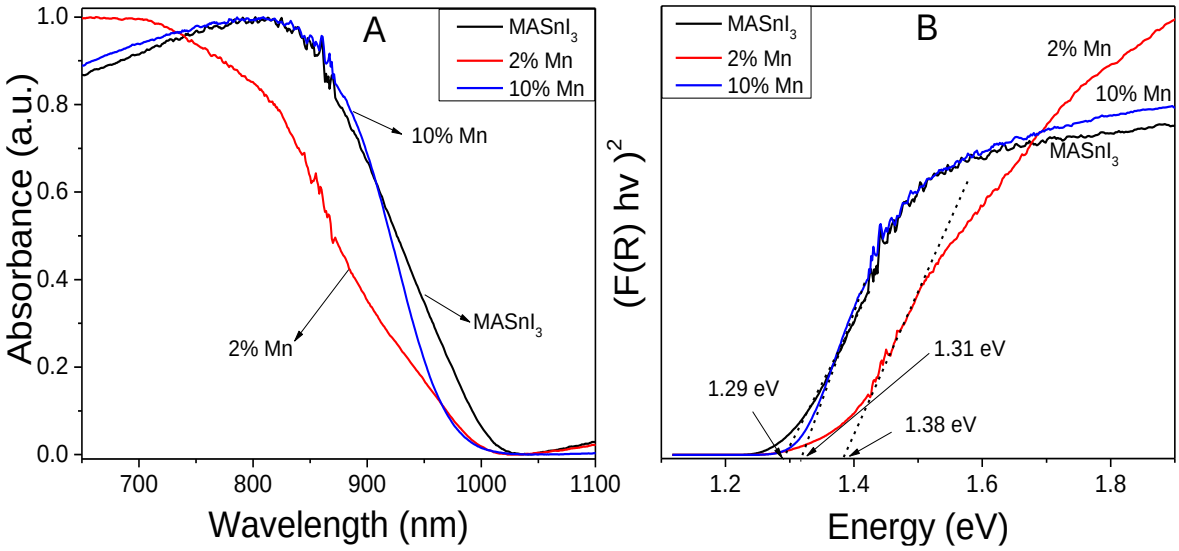

Figure 4.15 - A) Absorption spectra of the perovskites ($MASnI_3$ and Mn doped) and B) Kubelka-Munk function plots (direct bandgap). Extrapolation of bandgap based on the intersection of the linear part of the absorption edge with the x-axis.

From the absorption spectra, all the samples can absorb light in the visible and infra-red regions. Since the infra-red region of the solar spectrum is broad, extension into this region is advantageous. On the other hand, a high absorption of above-band photons can generate excess electrons which are lost through heat and lattice vibration.

The bandgaps of $MASnI_3$, 2% Mn and 10% Mn doped $MASnI_3$ were determined to be 1.29, 1.38 and 1.31 eV, respectively, and are typical of tin perovskites [3][30]. $MASnI_3$ had the lowest bandgap which is expected because of the precursor utilized (tin iodide) and the intrinsic properties of its band structure. The valence band is composed of Sn 5s and I 5p anti-bonding orbitals while the conduction band is made up of Sn 5p orbitals [28].

In general, the valence electrons in the 5s orbital of tin have a greater tendency to participate in bonding and as a consequence, there is greater interaction between the 5s and I 5p orbitals, shifting the valence band upwards, which reflects in the lower bandgap of tin perovskites compared to lead perovskites [95][8]. Thus, it is assumed that the replacement of a fraction of Sn atoms with Mn can reduce the orbital overlap of the Sn-I bonds, which lowers the

valence band energy and consequently, increases the bandgap compared to the pristine sample [95].

In general, the bandgaps of the Mn doped samples were higher compared to the pristine perovskite, being 1.38 eV for 2% Mn and 1.31 eV for 10% Mn. For higher Mn levels (10% Mn), discrete levels can be formed, which may contribute to the lower bandgap of 10% Mn compared to 2% Mn [237].

The contribution of chlorine from the $MnCl_2$ dopant can not be ignored. Castelli et al. (2014) found a correlation between increase in the electronegativity of halides and increase in bandgap [105]. From the Pauling´s scale, the electronegativity of Cl is 3.16 compared to 2.66 for I, which is consistent with the increase in bandgap observed for the doped samples compared to pristine $MASnI_3$.

The increase in bandgap of the doped samples can be beneficial since thermalization from excess electrons may be reduced and most importantly, open-circuit voltage can be improved [238]. On the other hand, the short circuit current decreases when the bandgap increases due to reduced absorption of photons.

4.1.7 Photoluminescence

Figure 4.16 presents the room temperature emission spectra of the pristine and doped samples (excitation wavelength 550 nm).

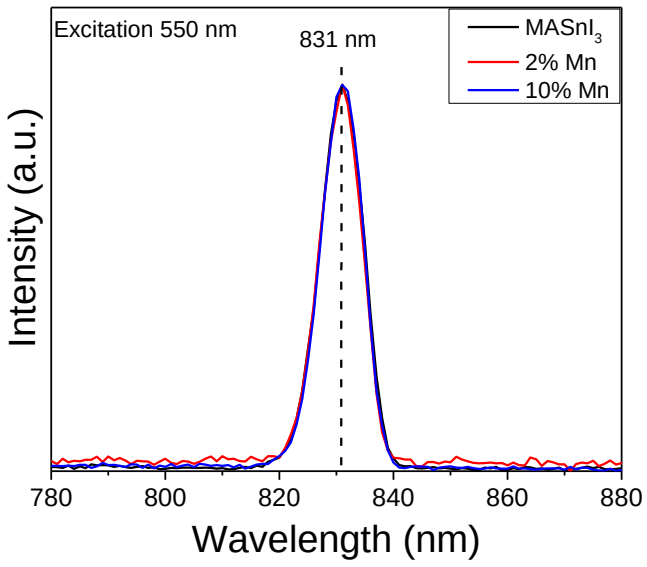

Figure 4.16 - Emission spectra of the pristine and Mn doped samples (550 nm).

All the samples present an emission centered at 831 nm (1.49 eV), which is not close to the bandgap values measured for the samples in the range of 1.29 to 1.38 eV. In direct bandgap semiconductors such as $MASnI_3$, defects, film quality among others can be responsible for shifts in expected PL values. For the samples, the observed emission can be ascribed to traps in the form of tin vacancies due to their low formation energy compared to other defects such as halide vacancies and anti-sites, where Sn occupies an iodide position or vice versa [239].

Since the doped samples presented identical emission values as the pristine sample, it can be presumed that they present defects intrinsic to the pristine perovskite.

4.1.8 Contact angle

For the electrochemical analysis of the perovskite samples, electrodes were prepared using PLA as a protective layer. To prove that the PLA film is to some extent permeable to water, its contact angle was measured. Figure 4.17 shows the water droplet on the PLA film at first contact and 60 s.

The average contact angle at the first drop and 60 s is 79 and 78 º, respectively. Since the angles are lower than 90 º and happen to decrease with time, the PLA film is hydrophilic and prone to water absorption with time. These properties can aid in electrochemical analysis.

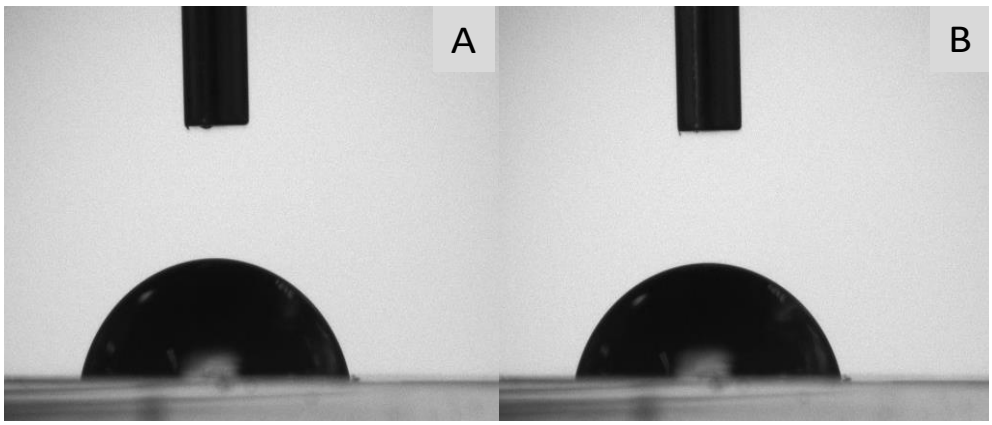

Figure 4.17 - A) Photo of water droplet in the beginning of test and B) at 60 s.

Figure 4.18 A shows the cross-section of the stripped PLA/10% Mn doped perovskite film. The width of both components (PLA plus perovskite) is 33 µm.

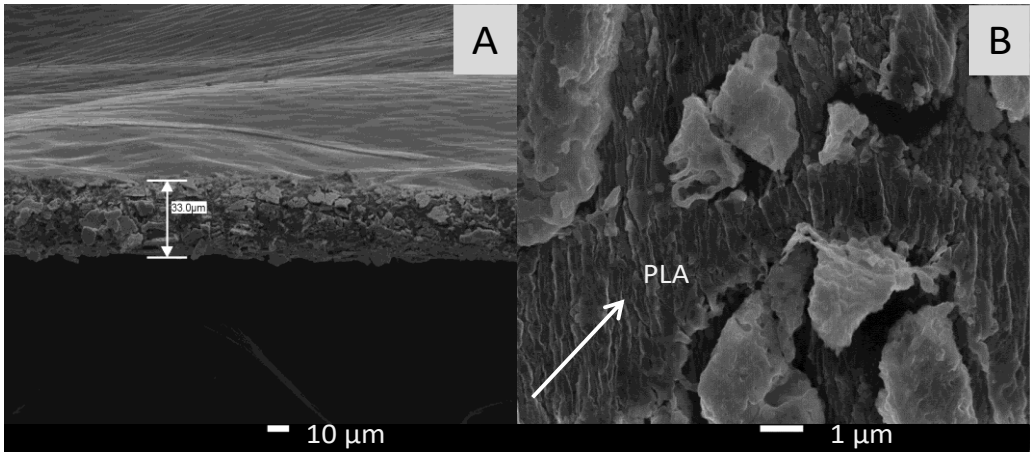

Figure 4.18 - A) Stripped PLA/10% Mn perovskite film indicating width and B) blending of perovskite with PLA.

Although one can see the PLA plane, it is difficult to demarcate its width. A closer look at the cross-section of the PLA/10% Mn doped film (Figure 4.18 B) shows that the polymer does not only cover the perovskite but blends with it. The large particles are the perovskite while the strand-like morphology is of PLA.

Figure 4.19 A shows the cross-sectional SEM-FEG image of a cut section of 10% Mn film on FTO substrate. Curling of the perovskite film is evident due to poor fracture.

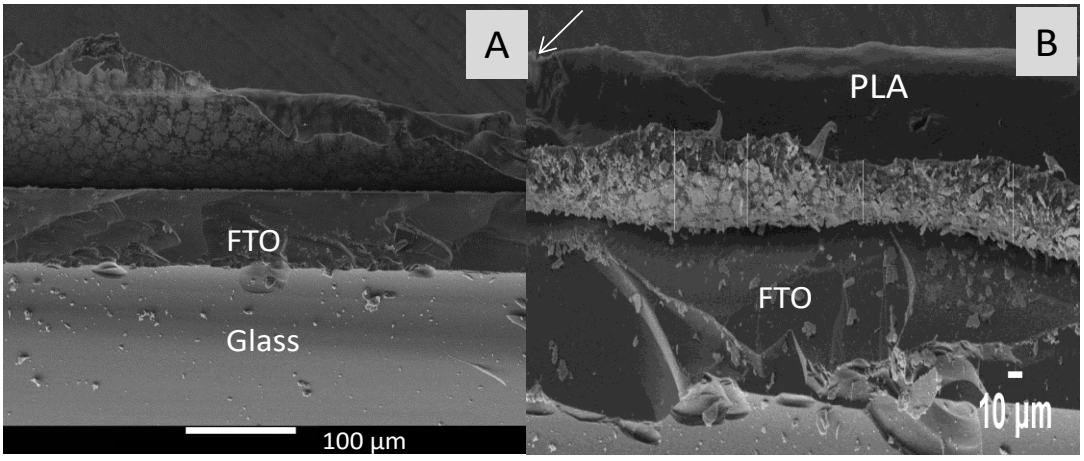

Figure 4.19 - A) Cross-section of PLA/10%Mn perovskite film indicating curling of the film and B) Cross-sectional image showing the 10% Mn perovskite/PLA layer.

Despite the top layer in Figure 4.19 B being marked as PLA, a closer look at the left corner (marked by an arrow) shows perovskite particles. This suggests that the area contains both materials but is on another plane. Thus, the film is not uniform due to poor fracture and its width (PLA/perovskite) was estimated as a

single entity. The width of the PLA/perovskite was estimated to be 30.25 µm based on the average of four different sections located above the FTO glass.

4.1.9 Electrochemical analysis

4.1.9.1 Aqueous measurements

Figure 4.20 shows the cyclic voltammograms of $MASnI_3$ and the Mn doped $MASnI_3$ electrodes (3 scans). The arrows represent the direction of the scans for conversion. It is possible to see that the samples suffer significant changes as the number of scan increases. Thus, the analysis of the samples was based on the first cycle.

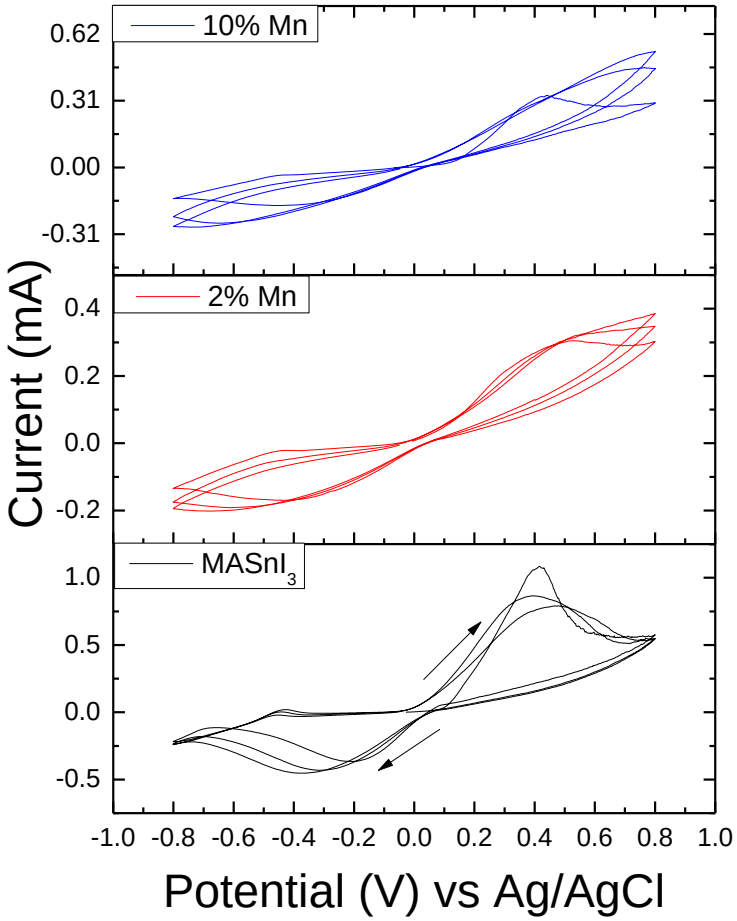

Figure 4.20 - Cyclic voltammogram of $MASnI_3$ and the Mn doped $MASnI_3$ electrodes obtained in 0.1 M aqueous Na_2SO_4 solution (0.1 V/s).

The first scans of the samples and PLA are shown in Figure 4.21. It can be seen that PLA presents negligible faradic events in the electrochemical

window analyzed and its profile is distinct. In other words, the properties of the measured samples can be considered as intrinsic of the perovskites.

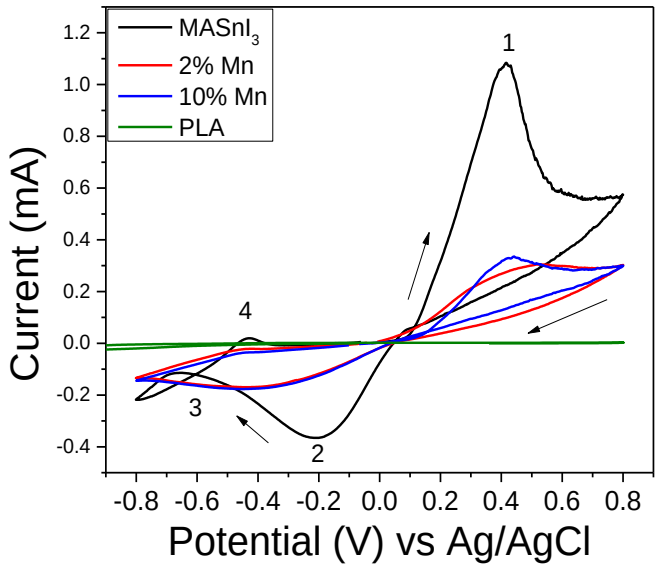

Figure 4.21 - Cyclic voltammogram of PLA, $MASnI_3$ and the Mn doped $MASnI_3$ electrodes obtained in 0.1 M aqueous Na_2SO_4 solution (0.1 V/s).

Faradic events of interest are observed in all the voltammograms indicating that the potential range adopted (-0.8 V to 0.8 V vs Ag/AgCl) is sufficient for the analysis. The forward scan highlights oxidation events (position 1) at 0.41 V, 0.52 V and 0.44 V vs Ag/AgCl for $MASnI_3$, 2% and 10% Mn electrodes, respectively. The event can be assigned to the oxidation of iodide ion (Equation 4.5) [240].

$$3I^- \rightarrow I_3^- + 2e \qquad (4.5)$$

The doped samples present higher oxidation potentials compared to $MASnI_3$, which shows that Mn increases resistance to oxidation. By comparing the peak current of the samples, $MASnI_3$ presented the highest current (1.08 mA) followed by 10% Mn doped (0.33 mA) and 2% Mn doped (0.30 mA). The high peak current of $MASnI_3$ may be related to the facile reaction of iodide ions in the $MASnI_3$ structure either due to the applied potential or contact with water. The doped samples were more resistive as seen from their low peak currents. Thus, although the oxidation potential of 10% Mn was slightly higher than 2% Mn, both samples have comparable resistance to oxidation.

A reduction peak was found at position (2) of Figure 4.21 corresponding to -0.20 V, -0.37 V and -0.37 V for $MASnI_3$, 2% and 10% Mn doped $MASnI_3$,

respectively. The peak can be assigned to the reduction of triiodide ions, Equation 4.6 [241].

$$I_3^- + 2e \rightarrow 3I^- \quad (4.6)$$

The reduction potentials shift to lower values with doping, which mean lower potentials are needed for reduction. A crossover (position 3) between the anodic and cathodic sweeps is observed for $MASnI_3$. This feature was observed by Yang et al. (2018) when they performed cyclic voltammetry of lead perovskite crystals in non-aqueous media [242]. This striking similarity is an indication that the PLA layer does not mask the properties of the perovskite.

A possible cause of the crossover is the nucleation or deposition of a new compound due to the degradation of the perovskite structure [243][244]. Thus, the absence of the event in the doped samples may suggest that Mn has a protective function. A second oxidation event at position (3) is evident in all samples at -0.44 V, -0.45 V and -0.46 V for $MASnI_3$, 2% and 10% Mn doped $MASnI_3$, respectively. The event was associated with the re-oxidation of iodide ions (Equation 4.7) [240].

$$3I^- \rightarrow I_3^- + 2e \quad (4.7)$$

The effect of doping on charge transfer mechanisms was evaluated by electrochemical impedance spectroscopy. The resultant Nyquist plot is shown in Figure 4.22.

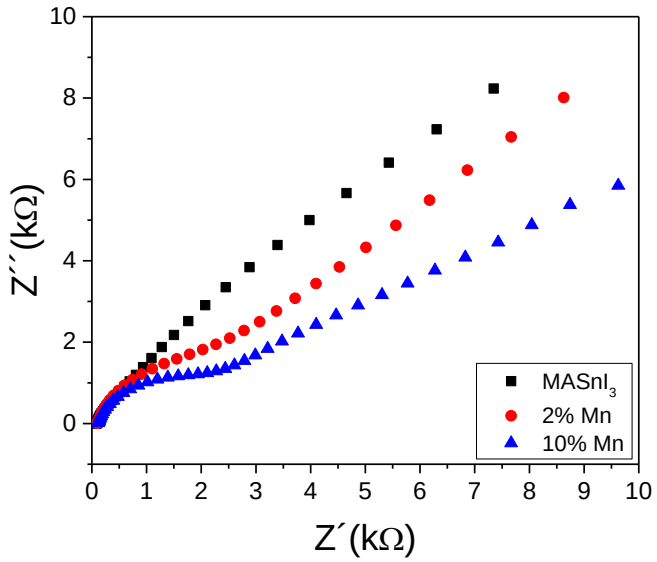

Figure 4.22 - Nyquist plot of $MASnI_3$ and the Mn doped $MASnI_3$ electrodes obtained in 0.1 M aqueous Na_2SO_4 solution (applied potential -0.15 V).

The resistance to charge transfer is affected by the PLA layer and the properties of the perovskite. In order to analyze the electrochemical properties of the samples, the Nyquist data were fitted using Nova software for the best Randles circuit which represents the profile of the samples. The Randles circuit for $MASnI_3$ was a RCW model, where R, C, W is solution resistance (48.1 Ω), capacitance (11.5 µF) and Warburg impedance (admittance (Yo) = 1.24 $mMho*s^{0.5}$), respectively. In relation to 2% Mn, its Randles circuit was [R(CRct)W] where R, C, Rct is solution resistance (81.1 Ω), capacitance (952 nF), charge transfer resistance (1.80 kΩ) and Warburg impedance (admittance (Yo) = 66 $µMho*s^{0.5}$), respectively.

For 10% Mn, the same circuit [R(CRct)W] for 2% Mn was utilized, where R, C, Rct is solution resistance (79 Ω), capacitance (469 nF), charge transfer resistance (1.55 kΩ) and Warburg impedance (admittance (Yo) = 41 $µMho*s^{0.5}$). The Randels circuits for all the samples are presented in Figure 4.23.

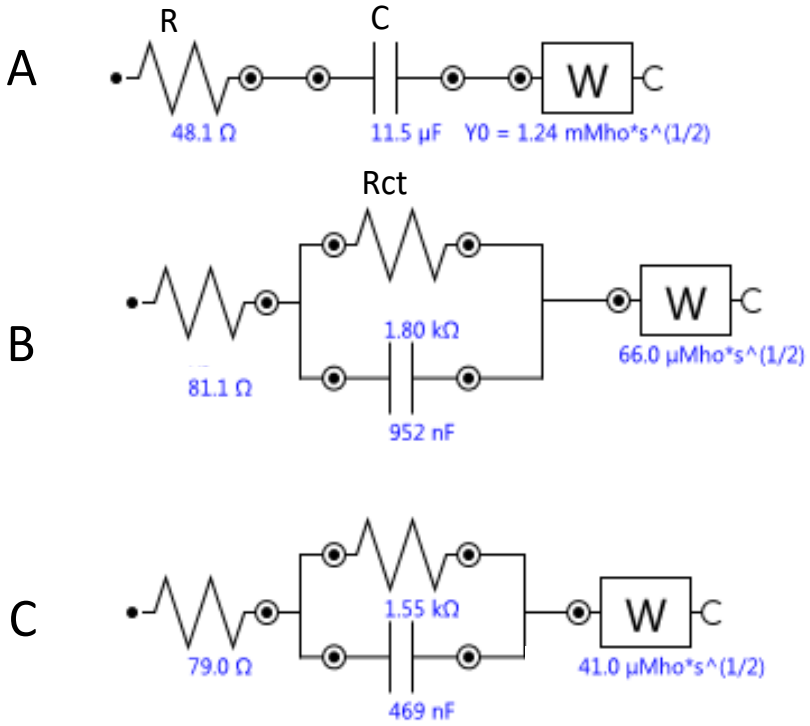

Figure 4.23 - Randles circuit of A) $MASnI_3$ (RCW), B) 2% Mn [R(CRct)W] and C) 10% Mn [R(CRct)W].

The solution resistance of $MASnI_3$ differed significantly from the doped samples although the electrolyte solutions were similar. Thus, it is presumed that the use of different models may have affected this parameter. Processes that

occur in the high frequency region (low to intermediate Z´ values) can be used to probe the kinetics of charge transfer at the surface of an electrode. $MASnI_3$ was considered to have negligible resistance to the transfer of electrons due to its profile and mainly because this parameter was not in the fitted model. This result is in agreement with the cyclic voltammetry results. The doped samples present semicircles, whose diameters determine the degree of resistance to the flow of electrons in general. From the Randles circuits, the resistance of 2% Mn was higher than 10% Mn, thus Mn at a higher level could improve electron transfer.

At low frequencies (high Z´ values), the behavior of the samples is controlled by diffusive processes and these processes are modelled by the Warburg element. Based on Equation 4.8 and the admittance (Yo) values, the Warburg coefficient (σ) can be calculated:

$$\sigma = \frac{1}{Y_o\sqrt{2}} \tag{4.8}$$

where σ is the Warburg coefficient and Yo is admittance.

It was 0.57, 10.71 and 17.25 kohm·$s^{-0.5}$ respectively, for $MASnI_3$, 2% and 10% Mn. The Warburg coefficient can be related to ion diffusion coefficient (D) through Equation 4.9 [245]:

$$\sigma = \frac{RT}{F^2AC\sqrt{2}D^{0.5}} \tag{4.9}$$

where R is the gas constant, T is the absolute temperature, F is the Faraday constant, A is electrode surface area, C is electrolyte concentration and D is diffusion coefficient.

Therefore, the higher the Warburg coefficient (σ), the lower the diffusion coefficient. Given that hysteresis in perovskites is associated with the migration of ions, the lower diffusion coefficients of the doped samples can be associated with stability [246]. Furthermore, a higher level of Mn (10%) seems to be beneficial for stability.

Figure 4.24 A shows the linear sweep voltammograms of the samples under dark and light conditions. From the cathodic sweep, the dark current of the samples was higher than the photocurrent, which is common for p semiconductors [247][248]. This means that the perovskite may be partially oxidized.

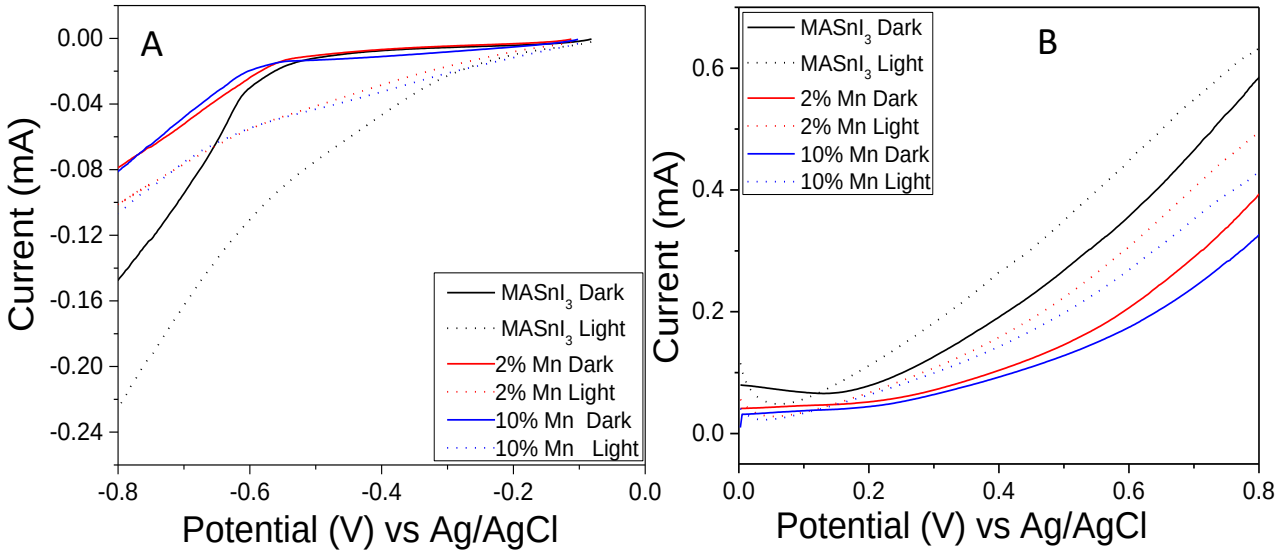

Figure 4.24 - A) Linear sweep voltammograms of $MASnI_3$, 2% and 10% Mn electrodes obtained in 0.1 M aqueous Na_2SO_4 under a negative starting potential (-0.08 V) and B) under a positive starting potential (0.02 V).

Thus, under negative potential and dark conditions, the concentration of holes surpasses electrons such that the conduction of the latter are suppressed with illumination. The difference between the light and dark current was more accentuated for $MASnI_3$ compared to the doped samples, suggesting that the concentration of holes could be lowered with doping. The variation among the doped samples was similar.

Figure 4.24 B shows the linear sweep voltammogram under dark and light conditions when a positive potential was used as a starting potential. Here, the samples behaved as photoactive semiconductors, where the photocurrent is greater than the dark current. As expected, $MASnI_3$ presented the highest photocurrent (0.62 mA) followed by 2% Mn doped (0.49 mA) and 10% Mn doped (0.43 mA). Mn appears to reduce the photocurrent of the perovskites, which implies lower reactivity and higher stability. On the other hand, this property is not beneficial for photovoltaic applications.

Figure 4.25 shows the photocurrent of the samples under negative and positive applied potentials. Similar to the linear sweep measurements, $MASnI_3$ presented the highest photocurrent under a negative applied potential. The photocurrents were negative indicating conduction was induced by holes. Among the doped samples, 10% Mn doped presented the second highest photocurrent

and 2% Mn doped presented the least current.

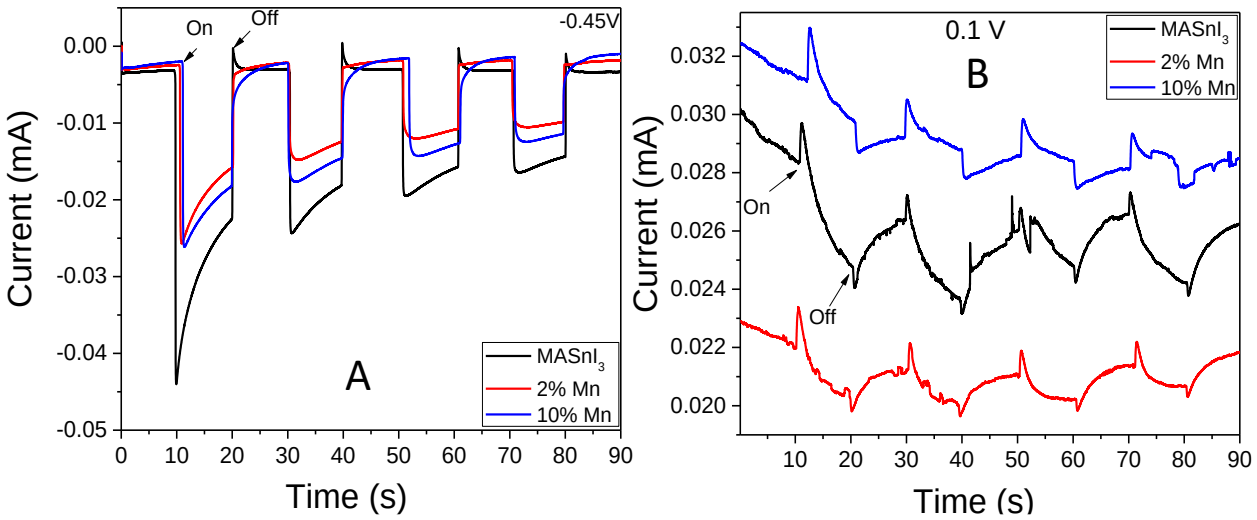

Figure 4.25 - A) Photocurrent of $MASnI_3$ and the Mn doped $MASnI_3$ electrodes in 0.1 M aqueous Na_2SO_4 under a negative applied potential (-0.45 V) and B) under positive applied potential (0.1 V).

The variation of photocurrent with time point to the poor photostability of the samples, especially the pristine perovskite. When a positive potential was applied as presented in Figure 4.25 B, the samples presented positive photocurrent but underwent severe photodegradation. This could be related to ionic migration induced by light [249].

Chronoamperometry measurements were conducted for 300 s under a positive potential (0.1 V) and the results are shown in Figure 4.26.

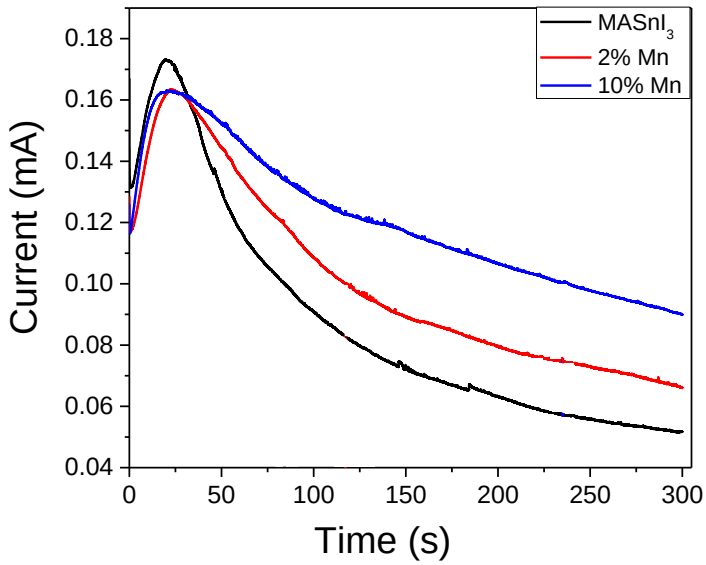

Figure 4.26 - Chronoamperometry curves of $MASnI_3$, 2% Mn and 10% Mn electrodes in 0.1 M aqueous Na_2SO_4 under positive applied potential (0.1 V).

The initial current of $MASnI_3$ (0.17 mA) was slighty higher than the 2% Mn (0.16 mA) and 10% Mn (0.16 mA) doped samples, which can be associated with higher reactivity at the electrode interface. All the samples present a current decay, where at 300 s, the current of $MASnI_3$ (0.05 mA) is the lowest followed by 2% Mn (0.07 mA) and 10% Mn (0.09 mA). The values demonstrate that the stability of $MASnI_3$ was improved with increase in Mn levels [250][251].

4.1.9.2 Non-aqueous measurements

Figure 4.27 shows the profile of the voltammograms obtained in non-aqueous medium (dichloromethane) with a concentration of 0.1 M of tetrabutylammonium hexafluorophosphate. It can be seen that $MASnI_3$ presents some properties observed in the aqueous analysis such as a crossover and clear oxidation and reduction peaks.

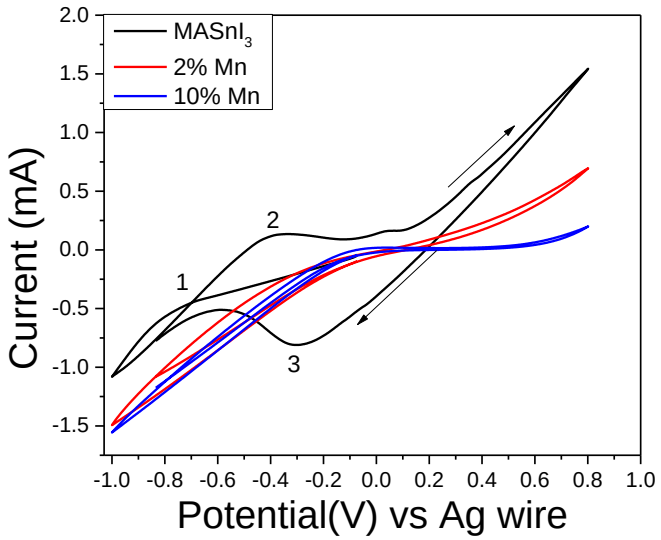

Figure 4.27 - Voltammograms of $MASnI_3$, 2% Mn and 10% Mn electrodes obtained in 0.1 M tetrabutylammonium hexafluorophosphate (dichloromethane).

The Mn doped samples have a higher resistance in accordance with the aqueous analysis, but possible oxidation and reduction peaks are not observed. $MASnI_3$ presents a crossover (point 1) at -0.69 V. A study reported a similar feature at -0.70 and -0.55 V [242]. As mentioned earlier, it can be associated with the formation of new phases.

When the potential is increased to more positive values, oxidation occurs at -0.39 V (position 2). It is difficult to assign a specific reaction since reactions

before the crossover determine which species can be oxidized. However, the oxidation of iodide species is highly speculated (Equation 4.10) [240].

$$3I^- \rightarrow I_3^- + 2e \quad (4.10)$$

With a reverse scan, a reduction peak can be found at position 3 (-0.30 V) and the reaction is presented in Equation 4.11 [241].

$$I_3^- + 2e \rightarrow 3I^- \quad (4.11)$$

The samples were further analyzed by electrochemical impedance. The impedance measurement shows that the samples present a far lower resistance (order of 10^2 compared to 10^3 (PLA)) to the flow of electrons due to the absence of the PLA layer impedance. The results are summarized in the Nyquist plot (Figure 4.28).

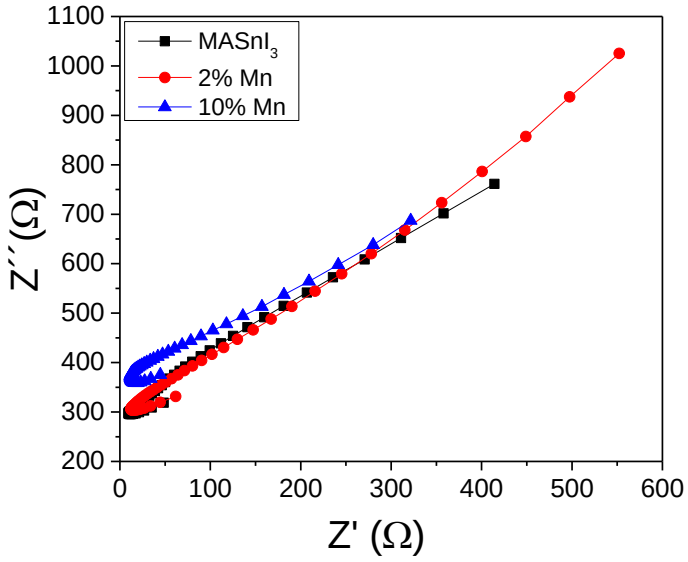

Figure 4.28 - Nyquist plots of $MASnI_3$ and the Mn doped $MASnI_3$ electrodes obtained in 0.1 M tetrabutylammonium hexafluorophosphate (dichloromethane).

The samples show what appears to be a loop at higher frequencies. Loops have been observed in perovskite/TiO_2 scaffolds but at intermediate and lower frequencies, and were linked to the number of interfaces in the scaffold [252]. Another possibility is the connection of the electrodes, which was not the case here. Based on these speculations, it is believed that the dissolution of the perovskite in the electrolyte solution and possible formation of other compounds could interfere with the impedance measurements. Thus, should be considered in the interpretation of this result. Figure 4.29 shows the dissolution of the perovskite film as the analysis proceeded.

Figure 4.29 - Photograph of degradation of $MASnI_3$ electrode in 0.1 M tetrabutylammonium hexafluorophosphate (dichloromethane).

The clear solution turned yellow as the experiments were conducted, thus further experiments were not considered.

4.1.10 Photovoltaic properties

Figure 4.30 shows the J−V curves of the best devices ($MASnI_3$ and Mn doped perovskites) and band alignment of the electron (TiO_2) and hole transport (P3HT) materials with the perovskites [253][30].

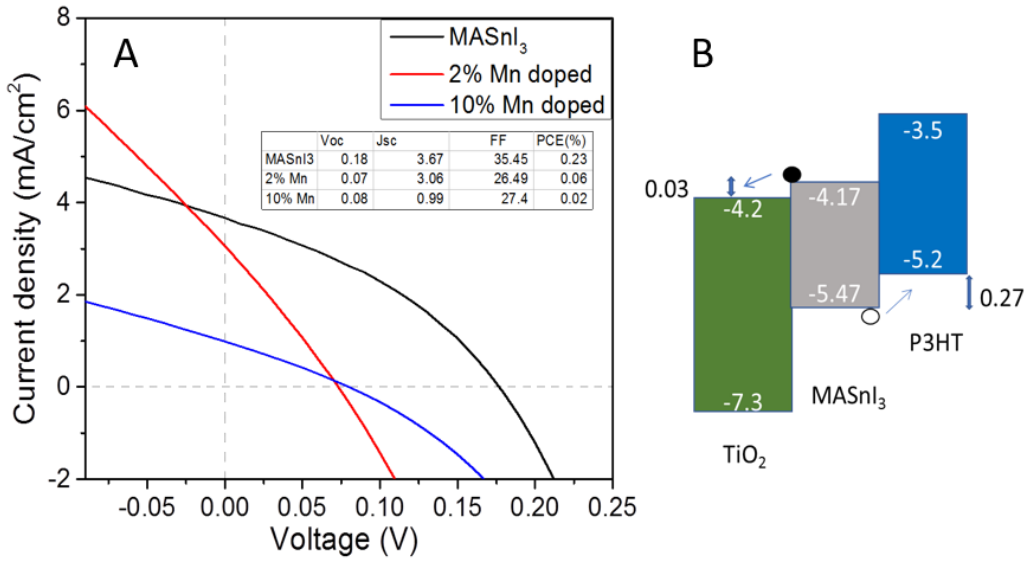

Figure 4.30 - J-V plots of $MASnI_3$ and Mn doped samples as well as band alignment. Insert: Summary of best cell results and PCE (power conversion efficiency).

The performance of the perovskite cells was not satisfactory because of low open-circuit voltage, current density and fill factor. However, they are not atypical of tin perovskites with P3HT [110]. For the $MASnI_3$ perovskite, the Voc,

Jsc, fill factor and PCE was 0.18 V, 3.67 mA/cm^2, 34.45% and 0.23%, respectively. In general, all the parameters associated with efficiency decreased upon Mn doping (2% and 10% Mn), which consequently decreased the efficiency of $MASnI_3$ from 0.23% to 0.06% (2% Mn) and 0.02% (10% Mn). A similar trend was seen in lead perovskites doped with Mn above 1%, suggesting that a small amount of Mn is adequate for the improvement of efficiency [219]. Table 4.2 presents a summary of the performance of the devices based on the best device and the mean of the batch containing the best device.

Table 4.2 - Performance of best devices and mean of best batch.

Sample	Voc (V)	Jsc (mA/cm^2)	FF(%)	PCE (%)
$MASnI_3$ (Best)	0.18	3.67	35.45	0.23
$MASnI_3$ (mean best batch)	0.17±0.01	2.88±0.33	34.36±0.53	0.16±0.03
2% Mn (Best)	0.07	3.06	26.49	0.06
2% Mn (mean best batch)	0.07±0.00	2.62±0.22	26.61±0.25	0.05±0.00
10% Mn (Best)	0.08	0.99	27.40	0.02
10% Mn (mean best batch)	0.08±0.00	0.86±0.10	26.37±0.37	0.02±0.00

The maximum short circuit current density (Jsc) that can be obtained from the device when voltage is null depends on the optical properties of the perovskite. The highest Jsc of $MASnI_3$ was associated with high light absorption presented by its low bandgap of 1.29 eV. This means that the generation of free electrons and holes is facilitated compared to the Mn doped samples. With doping, there was a slight increase in bandgap, which can reduce short circuit current density (Jsc). The trend of Jsc coincides with the electrochemical measurements where the doped samples presented lower photocurrents and higher resistance to the flow of electrons. Also, factors such as film quality and degree of recombination can interfere with the overall properties of the devices.

The effect of Mn on the open-circuit voltage (Voc) can be depicted from the decrease of the same. The maximum voltage shown by $MASnI_3$ decreased with Mn doping, from 0.18 V to 0.07 V (2% Mn) and 0.08 V (10% Mn). It was expected that doping should increase the Voc due to the slightly higher bandgap of the doped samples. As this did not occur, other factors that reduce the open-circuit can be considered.

Firstly, voltage losses through recombination is a plausible reason. Another factor could be the misalignment of the perovskite with the hole and

transport materials [254]. Theoretically, the selected electron transport material should be effective for charge transfer at the interfaces of the perovskite due to lower offsets with the hole and electron transport materials. However, during the operation of the solar cell, the real energy levels of the perovskite can change due to oxidation which can decrease the open-circuit voltage.

The fill factor of $MASnI_3$ decreased from 35.45 to 26.49 and 27.40% with Mn doping, which can be associated with high shunt resistance, poor quality of the perovskite cells and Mn. From the photovoltaic performance of the perovskites, it can be deduced that the photovoltaic properties of tin perovskite reduced with the incorporation of manganese. However, this finding is dependent on unoptimized devices. Thus, the potential of tin perovskites as well as Mn doping can be improved with optimization.

4.2 Tin perovskites synthesized with tin octoate and tin sulfate

4.2.1 Phase analysis

Figure 4.31 shows the diffraction patterns of the tin perovskites synthesized with tin(II) octoate at different temperature and time conditions.

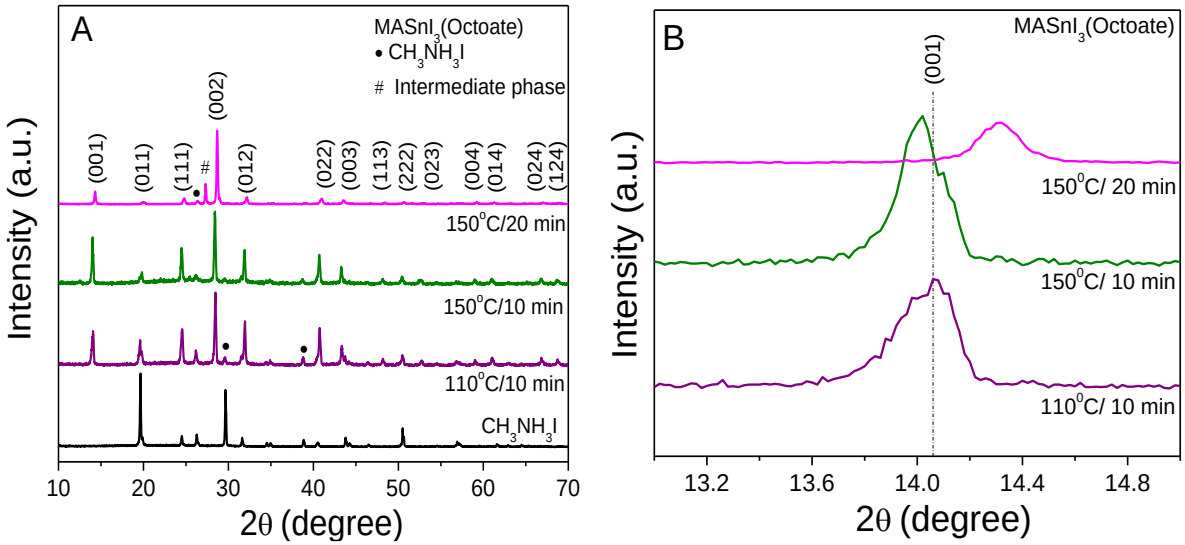

Figure 4.31 - A) Diffractograms of tin perovskite synthesized using tin octoate according to different temperature and time conditions and B) expanded view of (001) peak.

The patterns can be indexed to the pseudocubic phase, confirming the synthesis of tin perovskite using tin(II) octoate [3][16][97]. The (001) peak shifts

to a lower theta value with increase in temperature (110 ºC to 150 ºC). With increase in annealing time at 150 ºC, the (001) peaks shift to a higher theta value. Since a shift to higher theta values is related to lattice contraction, it is propably due to the loss of carbon residues from tin octoate with prolonged annealing (20 min) at high temperature (150 ºC).

Traces of methylammonium iodide can be seen in all samples.The sample annealed at 110 ºC presents a higher level of residual methylammonium iodide compared to the samples annealed at 150 ºC. However, increasing the annealing time (20 min) at 150 ºC was not beneficial to phase formation. The intensity of the perovskite peaks was reduced except for the (002) peak. Increasing the annealing time may not necessarily increase crystallinity since organic contents such as methylammonium might lose stability. Thus, the optimum condition is 150 ºC/10 min similar to the perovskite produced from tin iodide.

No secondary phase related to tin(II) octoate was identified, thus it is either incorporated into the perovskite structure or in the form of dangling bonds. All the peaks were more pronounced, suggesting non-preferential growth. This growth can be associated with the generation of dispersed nuclei due to steric hinderance caused by the octoate structure.

Figure 4.32 shows the diffraction patterns of the samples synthesized with $SnSO_4$ precursor.

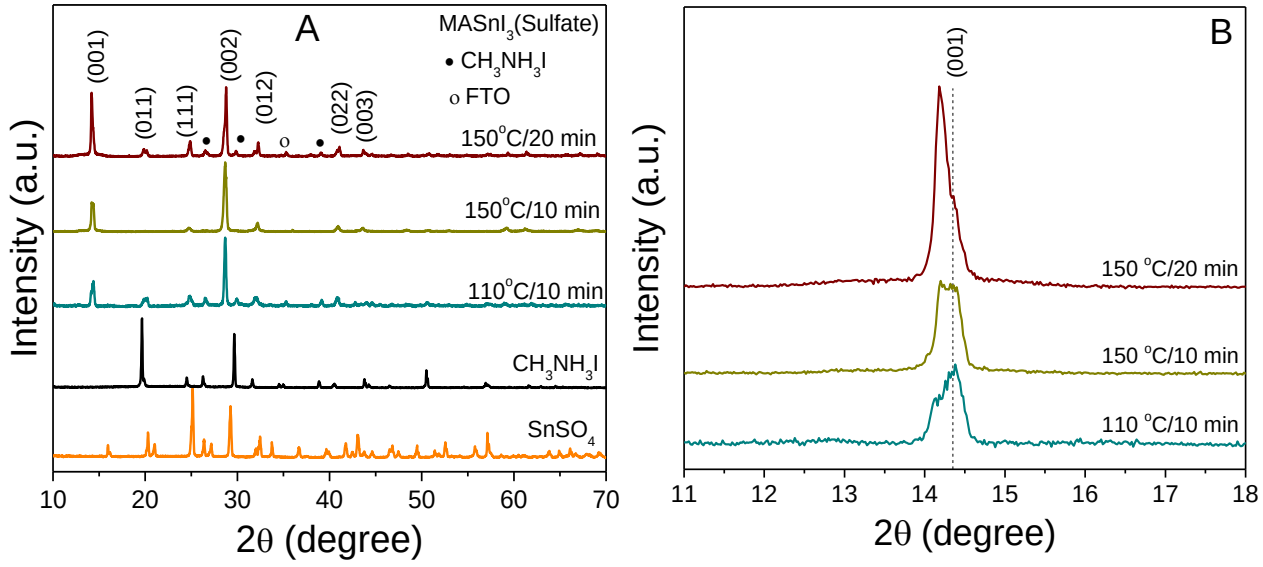

Figure 4.32 - Diffractograms of tin perovskite synthesized using tin sulfate and annealed at different temperature and time conditions and B) (001) peak.

Contrary to the tin octoate-derived perovskites, some form of preferential growth is apparent. It is believed that sulfur from the precursor can bind to iodide ions, affecting the crystallization energy of some planes. At 110 ºC, traces of methylammonium iodide can be seen in the sample. When the temperature was increased to 150 ºC, these traces decreased and the intensity of the (001) peak was not modified. With increase in annealing time, the traces of methylammonium iodide reappeared but the (001) peak was enhanced, which is contrary to the octoate-derived perovskites, where the intensity of the (001) peak as well as other perovskite peaks reduced with increase in temperature. This shows that tin perovskites derived from tin sulfate can withstand prolonged heat treatments, possibly due to sulfur.

4.2.2 Micro-Raman

Figure 4.33 presents the Raman spectra of tin perovskites synthesized using tin(II) octoate and tin(II) sulfate (150 ºC/10 min).

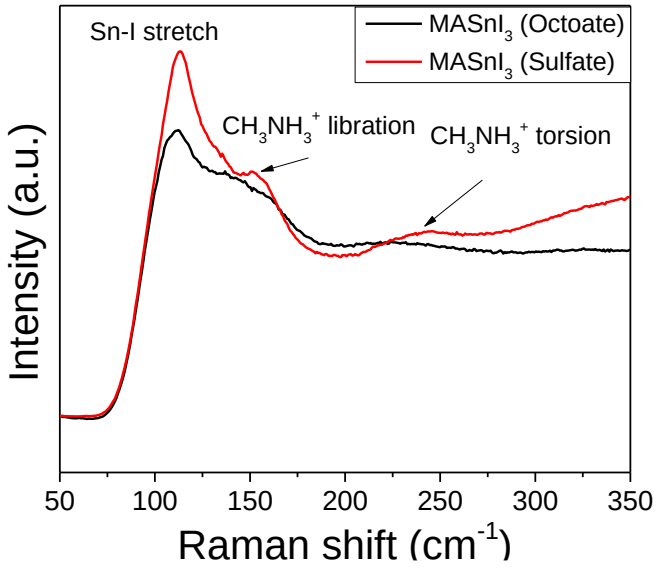

Figure 4.33 - Micro-Raman spectra of $MASnI_3$(Octoate) and $MASnI_3$(Sulfate) synthesized at 150 ºC for 10 min.

A vibrational mode at 112 cm^{-1} and 113 cm^{-1} can be observed for $MASnI_3$ (Octoate) and $MASnI_3$ (Sulfate), respectively, and was assigned to the Sn-I inorganic cage [255]. This mode is associated with perovskite formation and the successful reaction of iodide ions from methylammonium iodide with Sn from the

non-halide precursors. Thus, these perovskites have similar properties as those prepared from tin iodide.

In the 150 to 240 cm^{-1} regions, two bulges can be seen for all samples. They are assigned to the librational and torsion modes of methylammonium cation in ascending order [255][226], which confirm perovskite formation. The broader aspect of the bands, especially for $MASnI_3$ (Octoate) suggests a greater interferance of ethylhexanoate cations with the organic cage of the perovskite.

4.2.3 Fourier-transform infrared spectroscopy/Attenuated total reflection

Figure 4.34 shows the FTIR (ATR) spectra of methylammonium iodide and tin perovskites synthesized with tin octoate at different temperature and time conditions.

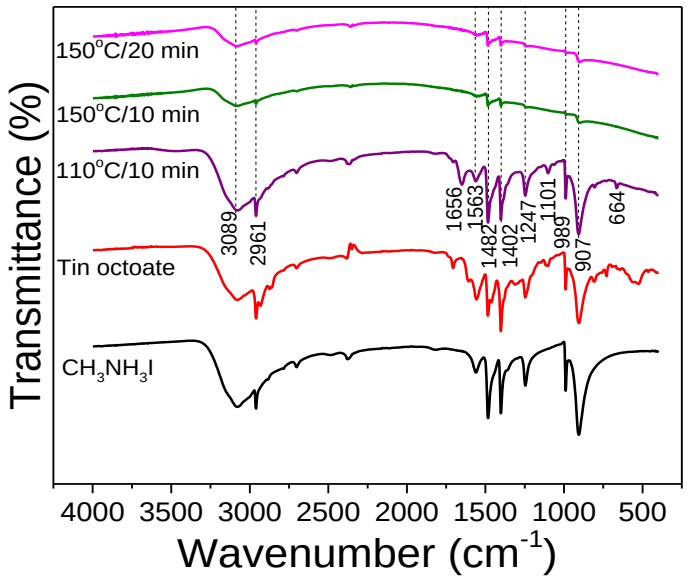

Figure 4.34 - FTIR (ATR) spectra of methylammonium iodide, tin octoate and tin octoate-derived tin perovskite synthesized at different temperature and time conditions.

The predominant vibrations in the samples were associated with organic species from the perovskite precursors.

In the functional group region, asymmetric N-H and symmetric C-H stretch bands at 3089 and 2961 cm^{-1} [224], respectively, are present in all samples as well as asymmetric N-H bending bands at 1563 cm^{-1} [224][256]. The NH_2 bending band at 1656 cm^{-1} is only present in the sample annealed at 110 °C/10 min [229].

The aforementioned bands are typical of organic species from the precursors (methylammonium iodide and tin octoate). They tend to have lower intensities with increase in annealing temperature (110 to 150 ºC). The sample calcined at 110 ºC presented N-H and C-H band intensities similar to methylammonium iodide and tin octoate. However, the intensity of the bands decreases with increase in temperature, pointing to intimate reaction between the reagents as temperature increases. With an increase in temperature and annealing time, the NH_2 bending band at 1656 cm^{-1} disappears, suggesting that these conditions may affect some bands [229].

In the fingerprint region, the bands at 1482, 1402 and 907 cm^{-1} assigned to C-H deformation [231], symmetric NH_3 bending [224] and CH_3NH_3 rocking [224], respectively, are present in all samples. However, the bands at 1247, 1101 and 989 cm^{-1} corresponding to CH_3NH_3 rocking [224], C-H wagging [232], and CH_2 rocking [257], respectively, are almost absent at high temperature (150 ºC). Thus, prolonged heating of the perovskite can be detrimental.

Figure 4.35 shows the FTIR spectra of the perovskites prepared with $SnSO_4$ and annealed at different temperature and time conditions. The precursors, $SnSO_4$ and methylammonium iodide, are also shown.

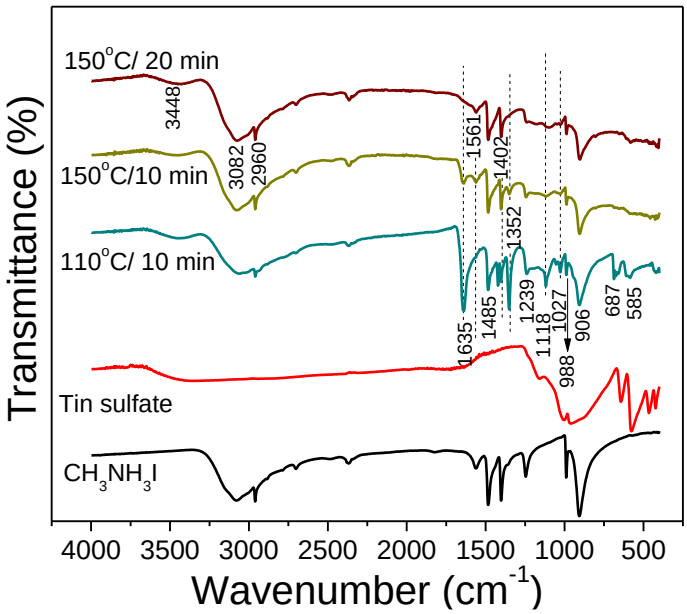

Figure 4.35 - FTIR (ATR) spectra of tin sulfate-derived tin perovskite synthesized at different temperature and time conditions.

As can be seen, tin sulfate contains no bands in the functional group region

(4000-1500 cm^{-1}) known for symmetric N-H stretching and/or O-H stretching (3448 cm^{-1}) [228][229], asymmetric N-H stretching (3082 cm^{-1}) [224], symmetric C-H stretching (2960 cm^{-1}) [224], NH_2 bending (1635 cm^{-1}) [229] and asymmetric N-H bending 1561 cm^{-1} [224]. However, the perovskite samples contain N-H and C-H bonds, which confirm the interaction of methylammonium iodide with tin sulfate. The vibrational mode at 1635 cm^{-1} assigned to NH_2 bending band is present in 110 ^oC/10 min and 150 ^oC/10 min but not in 150 ^oC/20 min [229].

The intensity of the same decreases with increase in temperature (110 to 150 ^oC) and completely disappears with prolonged heating (20 min). Thus, this band can be eliminated with prolonged heating. On the contrary, the asymmetric N-H bending band at 1561 cm^{-1} is enhanced with increase in temperature (110 to 150 ^oC). Vibrational modes at 1485, 1402, 1352, 1239, 1118, 988 and 906 cm^{-1} were present in all samples irrespective of annealing time and temperature and were assigned to C-H deformation, symmetric NH_3 bending, symmetric CH_3 bending, CH_3NH_3 rocking, C-H wagging, CH_2 rocking and CH_3NH_3 rocking, respectively [224][256][257]. The vibrational modes confirm the ability to form perovskites from tin sulfate.

Sulfur-related vibrations at 687 and 585 cm^{-1} were found in the samples and were attributed to CH_3-S and C-S stretching modes, respectively [258][259]. The intensity of the bands decreases with increase in temperature, pointing to a reduction in the level of dangling sulfur bonds.

4.2.4 Photoluminescence

Figure 4.36 presents the emission spectra of the tin octoate-derived perovskite treated at different calcination and time conditions. When the sample was treated at 150 ^oC for 20 min, the PL intensity decreased possibly due to the reduction of some planes evidenced by XRD analysis. Therefore, it can be assumed that the higher the crystallinity, the higher the PL intensity.

As regards sample 110 ^oC/10 min, its intensity was lower than the sample annealed at 150 ^oC/10 min. Since this particular sample supposingly had a greater level of dangling atoms (FTIR) associated with tin octoate, it is plausible that they passivate surface defects [260][261].

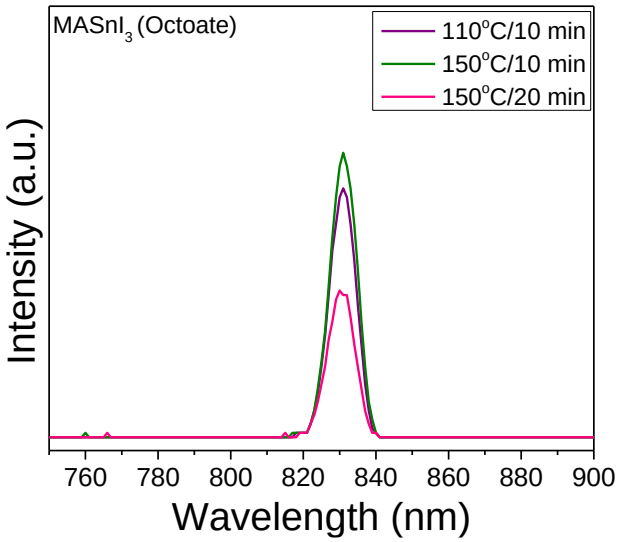

Figure 4.36 - A) Room temperature emission PL spectra of tin perovskites prepared from tin octoate. Excitation wavelength 550 nm.

Figure 4.37 shows the PL spectra of the tin perovskite produced with $SnSO_4$ precursor. The emission of the samples derived from tin sulfate occurred at 831 nm as the tin octoate samples. The PL intensity of the 150 °C/20 min was greater than its 110 °C and 150 °C/10 min counterparts.

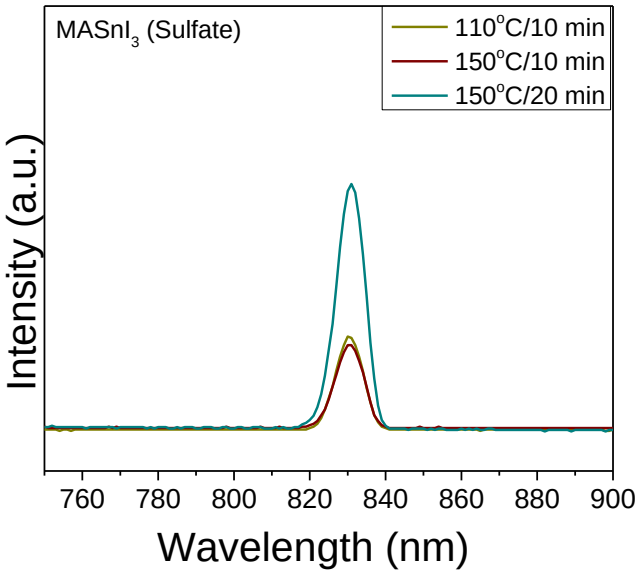

Figure 4.37 - A) Room temperature emission PL spectra of tin perovskites prepared from tin sulfate. Excitation wavelength 550 nm.

From the FTIR analysis, this sample appear to have minimal residual sulfur, thus dangling sulfur atoms may possibly contribute to recombination. Also, the diffraction patterns of the perovskite treated to the condition of 150 °C/20 min

were very pronounced, indicating that greater crystallinity is associated with greater luminescence.

4.2.5 UV-Vis Diffuse Reflectance Spectroscopy

Figure 4.38 presents the absorption spectra and the Kulbelka-Munk function of the samples prepared with tin octoate.

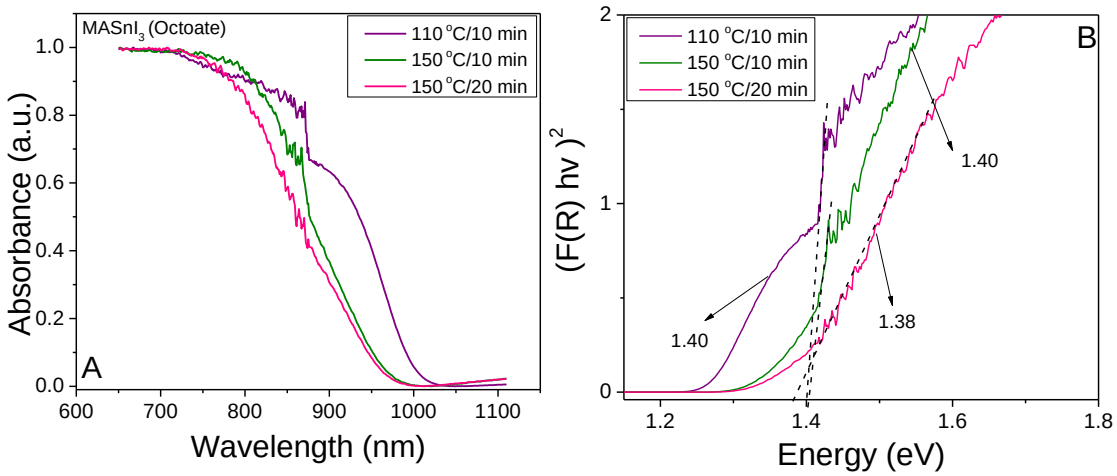

Figure 4.38 - A) Absorption of the perovskites in the visible region and B) Kubelka-Munk function for a direct bandgap with extrapolation of bandgap based on the intersection of the linear part of the absorption edge with the x-axis.

The samples show absorption in the visible region and near infra-red regions. The bandgaps observed (1.38 and 1.4 eV) were higher than the halide-derived perovskites (1.29 eV). From Figure 4.38 B, the bandgap of the tin octoate perovskites decreased from 1.4 eV to 1.38 eV with an increase in temperature from 110 ºC to 150 ºC. However, the decrease was only observed for the sample annealed at 150 ºC for 20 min.

Given the size of the organic cations in tin octoate compared to methylammonium, there can be distortion of the Sn-I octahedra leading to changes in bandgap according to annealing temperature and time [262]. Note that organic cations from tin octoate can cause bandgap increase by distorting the Sn-I octahedra and/or perovskite lattice [28][86]. Some authors have also linked lattice expansion to bandgap increase [263]. From the XRD analysis of the samples, annealing at 150 ºC for 20 min caused a significant shift in the (001) peak to higher theta values, pointing to lattice contraction associated with

bandgap reduction. Based on these assumptions, an increase in temperature from 110 ºC to 150 ºC will reduce organic residuals, which can cause bandgap reduction, especially when the annealing temperature is maintained for 20 min.

Figure 4.39 shows the absorption spectra of the tin perovskites derived from tin sulfate and the extrapolation of their bandgaps.

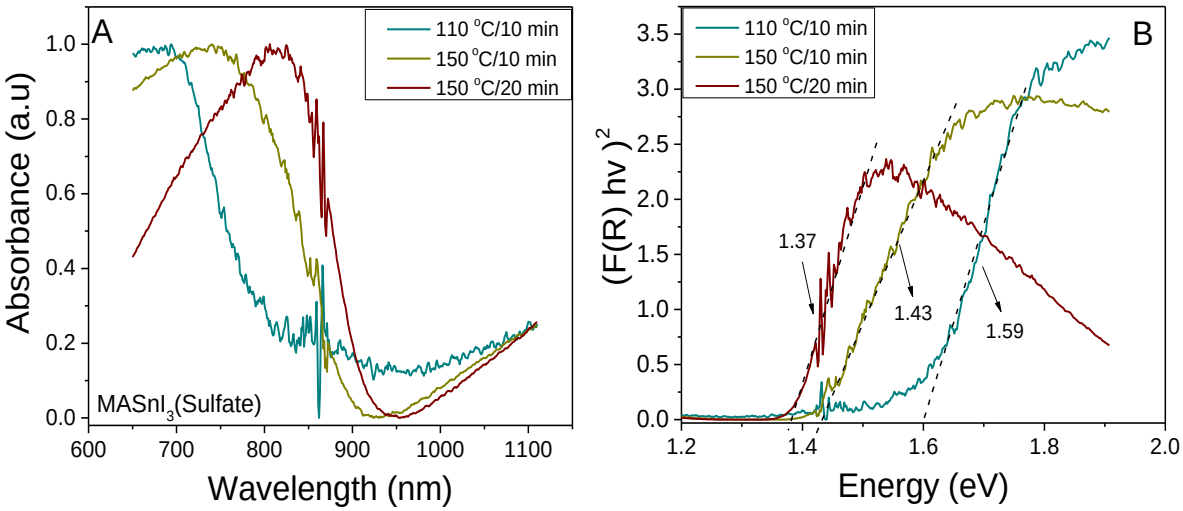

Figure 4.39 - A) Absorption of the perovskites in the visible region and B) Kubelka-Munk function for a direct bandgap material with bandgap extrapolation based on the intersection of the linear part of the absorption edge with the x-axis.

The samples present absorption in the visible region as expected, however, the bandgaps are higher than their iodide counterpart, $MASnI_3$ (1.29 eV). $MASnI_3$ (1.29 eV) annealed at 150 ºC/10 min has a lower bandgap than $MASnI_3$ derived from $SnSO_4$ (1.43 eV). The presence of sulfur may shift the valence band energy downwards (higher bandgap) if it increases antibonding between Sn 5s and I 5p orbitals [95][8].

The effect of temperature on the bandgaps of the samples was significant, being that increasing the annealing temperature (110 ºC to 150 ºC) caused the bandgap to decrease (1.59 to 1.43 eV). Also, prolonged heating (20 min) at 150 ºC had a decreasing effect on the bandgap (1.43 to 1.37 eV). It is believed that increasing the annealing temperature as well as prolonging annealing time can contribute to the reduction of sulfur in the samples, thus reducing the bandgap.

4.2.6 Scanning electron microscopy

The effect of tin octoate on the morphology of the perovskites was probed

by SEM (Figure 4.40).

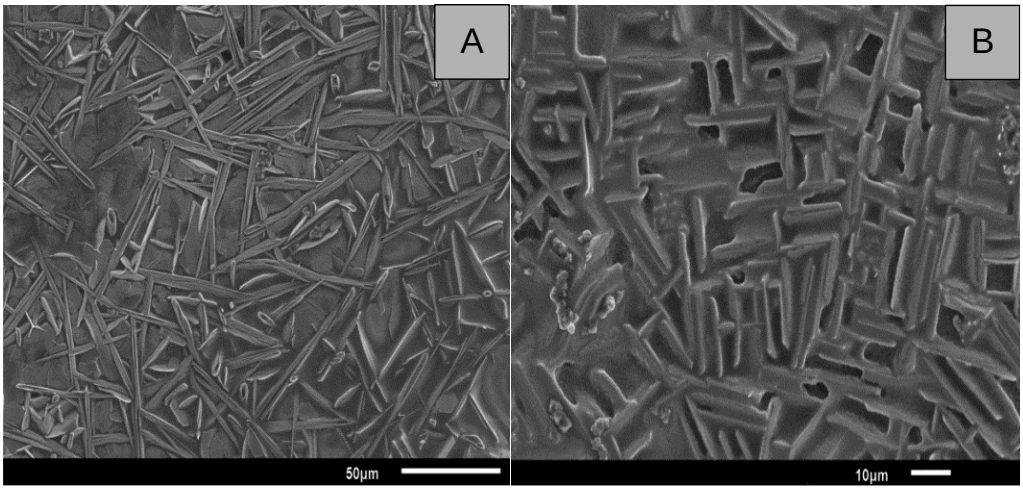

Figure 4.40 - A) SEM micrograph of $MASnI_3$ (Octoate) synthesized at 150 ^oC/10 min and B) Higher magnification of micrograph.

The morphology of $MASnI_3$ (octoate) consists of neddle-like structures, which form part of a continous film. This type of morphology can be associated with rapid nucleation at inhomogeneous sites due to high residual carbon and consequent poor growth [264]. Crystallization from DMF without solvent engineering can also be cited [264][149]. As the film was deposited by drop casting, its morphology can be improved by solvent engineering and other deposition methods such as spin coating.

The morphology of $MASnI_3$ (Sulfate) is shown in Figure 4.41. The migrograph shows that $MASnI_3$ (Sulfate) is formed of well-defined grains with some pinholes.

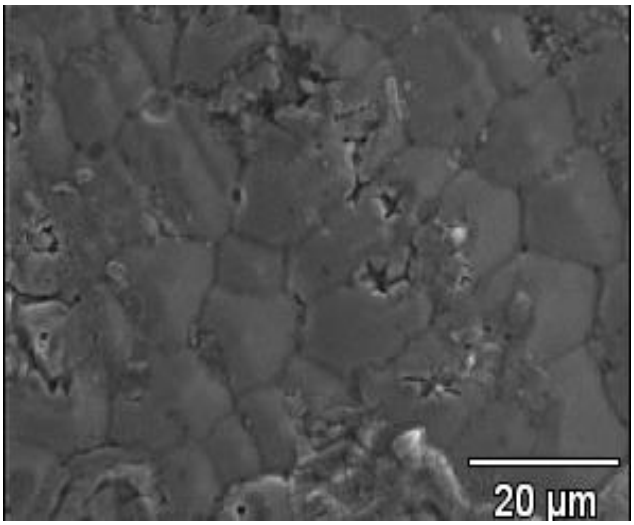

Figure 4.41 - SEM image of $MASnI_3$ (Sulfate) synthesized at 150 ^oC/10 min.

Grains are desirable for good carrier transport and low recombination. The formation of large grains can be associated with sulfate ions. Sulfur can bind strongly to tin atoms forming adducts which can slow down crystallization. It is expected that sulfur is not entirely removed from the perovskite, similar to chlorine as observed for the perovskite doped with $MnCl_2$. It is emphasized that the film quality can be improved by choice of solvents and deposition.

The distribution of Sn, C and I in $MASnI_3$ (Octoate) was verified by EDX and is presented in Figure 4.42.

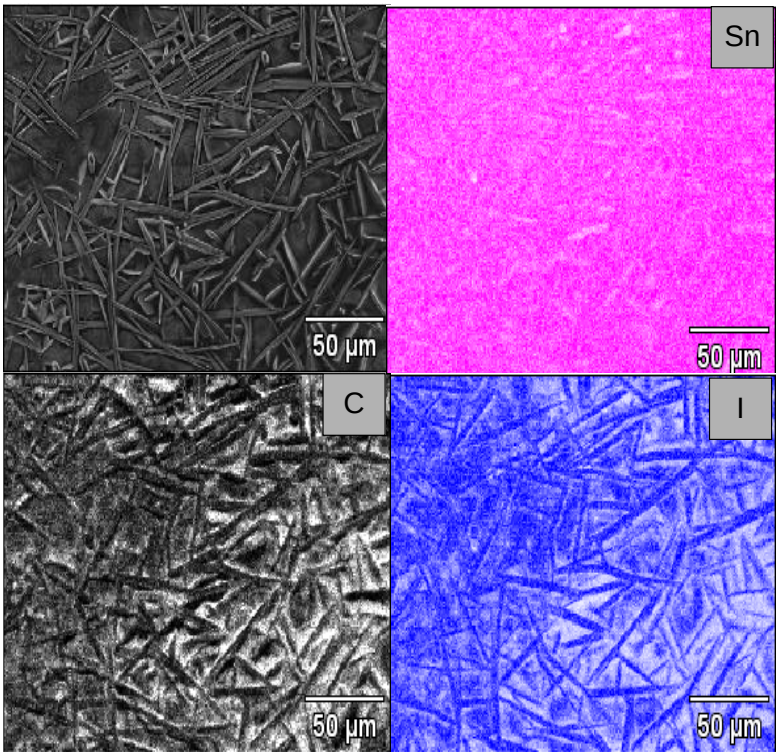

Figure 4.42 - EDX mapping of $MASnI_3$ (sulfate) synthesized at 150 ^oC/10 min.

It can be seen that the distribution of Sn is satisfactory. The neddle-like regions were mainly formed of iodine and carbon, suggesting that excess carbon from tin octaoate and excess iodine from methylammonium iodide may be responsible for the observed morphology. The challenge of using non-halide precursors involves the elimination of these byproducts.

The distribution of Sn, S and I was probed by EDX mapping and is shown in Figure 4.43. From EDX mapping, the distribution of Sn and I is satisfactory. Sulfur is not completely removed and its distribution is acceptable, depicting a lower tendency of segregation. Thus, ions such as sulfur or chlorine in the precursors become part of the perovskite chemical composition and can

contribute to the properties of the same.

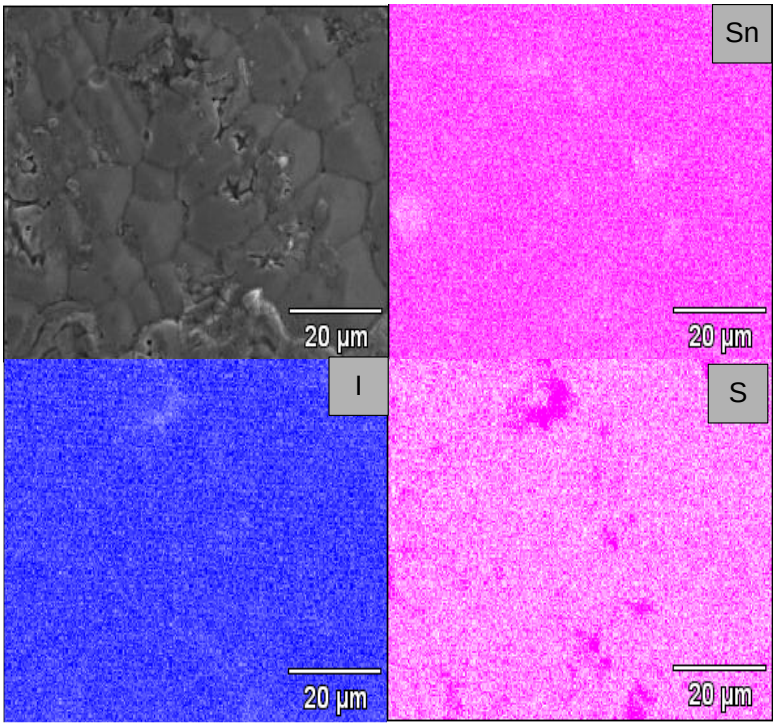

Figure 4.43 - EDX mapping of $MASnI_3$ (sulfate) synthesized at 150 ºC/10 min.

4.3 Oxygen-deficient TiO_2

In order to study the potential of oxygen-deficient TiO_2 as an electron transport material in perovskite cells, a general characterization of the same was conducted. Also, the effects of titanium isopropoxide concentration on the synthesis and characteristics of oxygen-deficient TiO_2 were analyzed.

4.3.1 Electron paramagnetic resonance

Electron paramagnetic resonance (EPR) is a useful technique for characterizing paramagnetic species associated with oxygen vacancies. The removal of an oxygen atom from the lattice disrupts the electroneutrality of the crystal. In this case, two electrons are bound to the vacant position to restore neutrality as expressed in Equation 4.13. This type of vacancy is known as neutral oxygen vacancy (F).

$$V_0 + e^- \rightarrow F^+ \quad (4.12)$$

$$V_0 + 2e^- \rightarrow F \quad (4.13)$$

$$V_0 \rightarrow F^{2+} \qquad (4.14)$$

The electrons bound to the neutral vacancy can be ionized, generating single positively (F^+ center) charged oxygen vacancy (Equation 4.12) or double positively charged oxygen vacancy (F^{2+} center) (Equation 4.14) [265]. Also, the electrons can reduce Ti(IV) species to Ti(III) [265]. Both F^+ and Ti(III) species are paramagnetic and detectable by EPR technique.

Figure 4.44 presents the EPR spectra and their double integration.

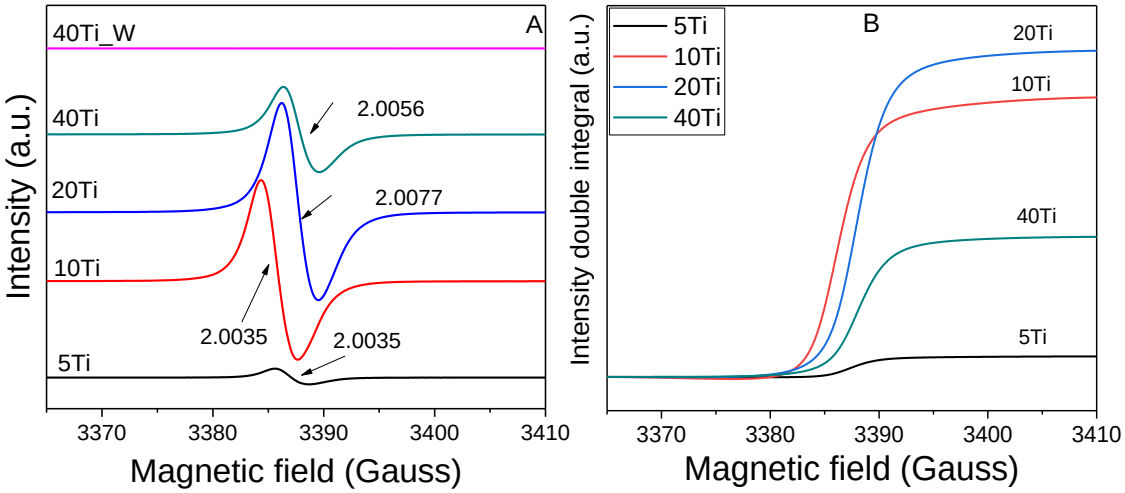

Figure 4.44 - A) Room temperature EPR spectra of samples (5Ti-40Ti) containing different volumes of Ti-isopropoxide (5 mL to 40 mL) and 40Ti powder (40Ti_W) calcined at 800 ºC and B) double integration of the EPR signal.

The estimated g-factors of the samples were 2.0035, 2.0035, 2.0077 and 2.0056 for 5Ti, 10Ti, 20Ti and 40Ti, respectively. They confirm the presence of oxygen vacancy with a trapped electron or single positively charged oxygen vacancy (F^+ center) [266][267], regardless of volume of titanium isopropoxide. Variations in g-factors indicate different local environment of the unpaired electrons related to strain and long/short range disorder [268].

Sample 40Ti_W did not present any paramagnetic species indicating the absence of oxygen vacancies (F^+). Given that 40Ti has oxygen vacancies, their absence in 40Ti_W suggests that calcination at 800 ºC may have annihilated them. It should be emphasized that other forms of diamagnetic defects related to oxygen vacancies are not accounted for by this technique.

Although the quantification of oxygen vacancies is beyond the scope of the study, a double integration of the signal provides a gross estimation based on

area. From Figure 4.44 B, sample 20Ti has the highest level of charged oxygen vacancies followed by 10Ti, 40Ti and 5Ti. Apparently, the level of charged oxygen vacancies increased from 5Ti to 20Ti with increase in the volume of Ti-isopropoxide, but decreased for 40Ti when the volume was increased beyond 20 mL. The absence of Ti(III) species in the samples can be attributed to the mild reducing conditions of the experiment.

4.3.2 X-ray diffraction

The diffraction patterns of the samples (5Ti, 10Ti, 20Ti, 40Ti and 40Ti_W) are shown in Figure 4.45.

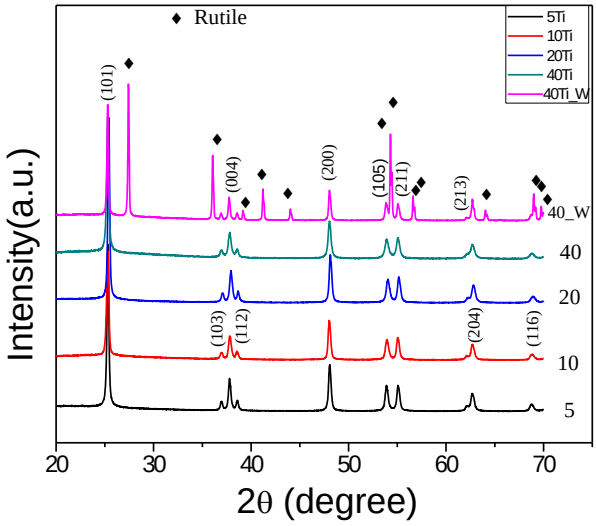

Figure 4.45 - X-ray diffraction patterns of samples containing different volumes of titanium isopropoxide (5-40Ti) and white 40Ti powder (40Ti_W) obtained by calcining 40Ti powder at 800 ºC.

They were indexed to anatase phase (PDF#04-0477) with the exception of Ti40_W which contains both rutile (60%) and anatase (40%) due to its high calcination temperature (800 ºC). The lattice parameters of the samples are presented in Table 4.3.

A subtle variation of the a=b lattice parameters is observed. The c lattice parameter and lattice volume underwent significant changes, where the lattice volume decreased in the order: 5Ti, 10Ti and 20Ti but increased for 40Ti. The order coincides with increase in singly charged oxygen vacancies and decrease in the same for sample 40Ti. This trend suggests that charged oxygen vacancies

can cause lattice contraction. Dang et al. (2019) reported the lattice contraction of rutile with greater loss of oxygen vacancies [269]. Naldino et al. (2012) also observed lattice contraction associated with oxygen vacancies [270].

Table 4.3 - Lattice parameters of 5Ti, 10Ti, 20Ti, 40Ti and 40Ti_W.

Sample	*a=b* (Å)	*c* (Å)	Volume (Å³)
5Ti	3.787	9.524	136.602
10Ti	3.787	9.508	136.383
20Ti	3.786	9.504	136.222
40Ti	3.788	9.516	136.528
40Ti_W (Anatase 39.6 wt%)	3.783	9.521	136.252
40Ti_W (Rutile 60.4 wt%)	4.593	2.960	62.442

4.3.3 Micro-Raman

Figure 4.46 shows the micro-Raman spectra of the samples. All the samples present modes corresponding to anatase whereas 40Ti_W presents additional modes related to rutile phase, in agreement with the XRD results.

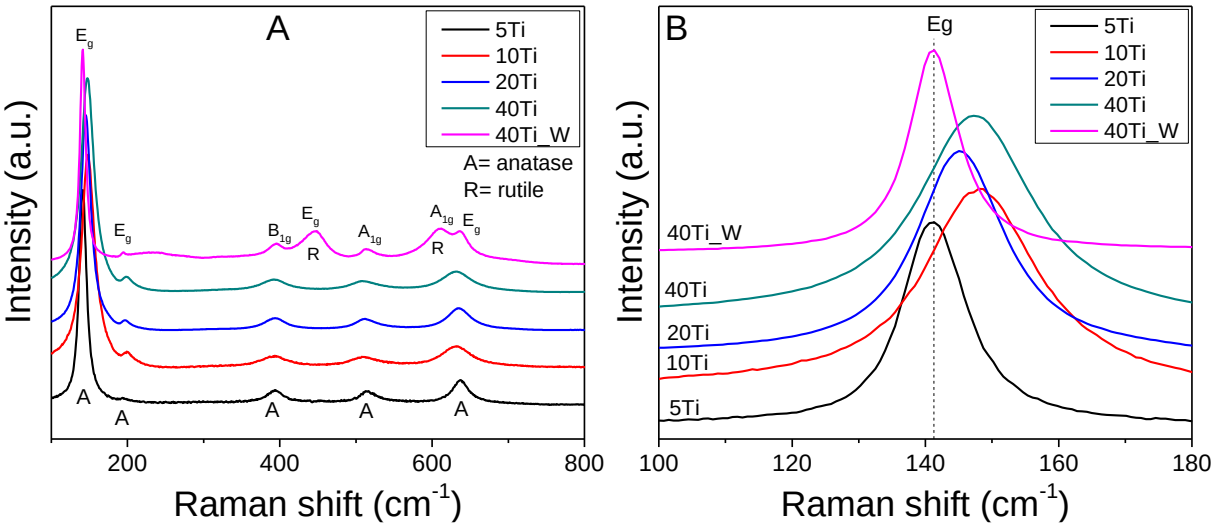

Figure 4.46 - A) Micro-Raman spectra of TiO_2 samples (5Ti, 10Ti, 20Ti, 40Ti and 40Ti_W) and B) Eg mode of all samples.

The Eg mode is characteristic of symmetric stretching of Ti-O-Ti bonds, thus it was analyzed for any apparent shift related to oxygen vacancies (Figure 4.46 B)[271][272]. In general, a shift to higher frequencies was observed (5Ti to 40Ti). A shift to higher frequencies can be associated with contraction of the lattice due to the presence of oxygen vacancies as indicated by XRD and EPR.

According to Hooke´s law, vibration frequency is directly proportional to bond strength (force constant) and inversely proportional to reduced mass (Equation 4.15):

$$v = \frac{1}{2\pi c}\sqrt{\frac{k}{\mu}} \tag{4.15}$$

where v is vibration frequency, k is force constant, c is the speed of light and μ is reduced mass.

The reduced mass (μ) is $\frac{m1.m2}{m1+m2}$ where m1 and m2 is the mass of elements 1 and 2, respectively. Thus, oxygen vacancies will act to decrease the reduced mass, resulting in shifts to higher frequencies. The shift to lower frequency shown by 40Ti_W compared to 40Ti highlights the effect of heat treatment on the reduction of oxygen vacancies. When 40Ti is heat-treated at 800 ^{o}C in air, the reducing environment provided by the initial synthesis may be limited, which can reduce the level of oxygen vacancies.

4.3.4 Transmission Electron Microscopy

The high resolution transmission micrographs of selected samples are presented in Figure 4.47: 5Ti, 20Ti, 40Ti and 40Ti_W. Oxygen-deficient TiO_2 has been shown to have a peculiar morphology consisting of a disordered outer layer and crystalline core [270]. Samples 5Ti, 20Ti and 40Ti have both crystalline and amorphous regions discriminated by the presence and absence of lattice fringes, respectively.

Note that 40Ti_W has no amorphous layer, thus it can inferred that the sample contains less oxygen vacancies and higher crystallinity at the surface associated with higher calcination temperature (800 ^{o}C). In general, the widths of the amorphous layers in the samples are not homogenous which could affect

surface properties. Sample 5Ti contains dislocations, suggestive of defects in the lattice as well as on the surface.

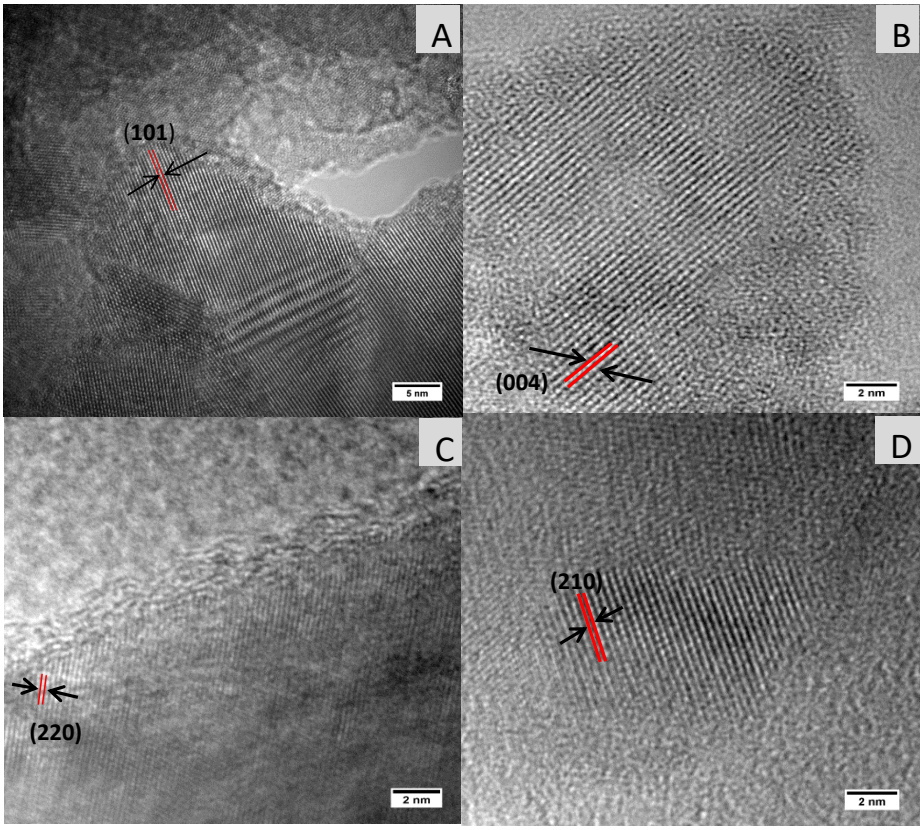

Figure 4.47 - High resolution transmission micrographs of A) 5Ti B) 20Ti C) 40Ti and D) 40Ti_W.

The d spacing marked for samples 5Ti, 20Ti, 40Ti are 0.350 nm, 0.235 nm, 0.130 nm corresponding to the (101), (004) and (220) planes of TiO_2 anatase phase, respectively [273]. For 40Ti_W, the d spacing was 0.209 nm equivalent to the (210) rutile plane [273]. The results highlight the phase composition of the samples and are in agreement with the XRD and micro-Raman analyses.

4.3.5 Field Emission Gun Scanning Electron Microscopy

The SEM-FEG micrographs of 5Ti, 10Ti, 20Ti, 40Ti and 40Ti_W are shown in Figure 4.48. They reveal that the samples are predominantly formed of micrometric agglomerates. The micrometric nature of the samples could be attributed to the fact that surfactants were not utilized. Sample 5Ti and 10Ti presented similar morphologies in the form of micrometric agglomerates composed of nanometric particles.

As regards the samples synthesized with 20 mL (Figure 4.48 C and D) and 40 mL (Figure 4.48 E) of titanium isopropoxide, the concentrations of Ti(IV) species are higher compared to 5Ti (Figure 4.48 A) and 10Ti (Figure 4.48 B).

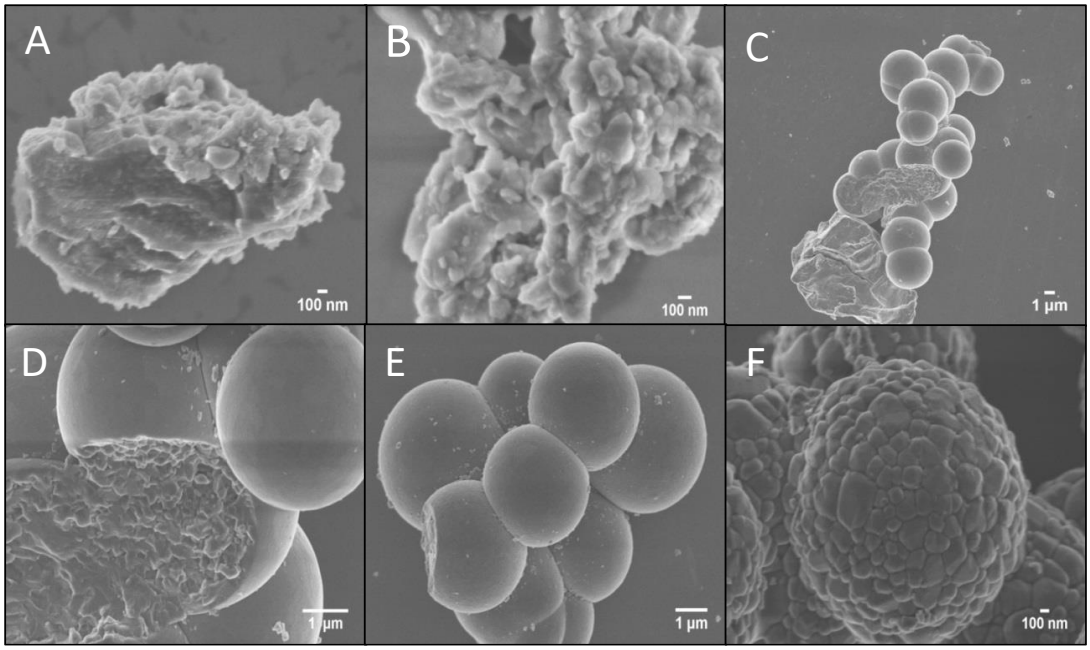

Figure 4.48 - Field emission gun (FEG)-SEM micrographs of A) 5Ti, B) 10Ti, C) 20Ti, D) 20Ti (Magnification), E) 40Ti and F) 40Ti_W.

Thus, upon the addition of HCl, the precipitation of titanium hydroxide species occurs due to higher reactivity. Given the higher quantity of precipitates, they assembly into microspheres and are maintained apart by electrostatic repulsion [274].

Figure 4.48 D shows the internal structure of the agglomerates in sample 20Ti. It shares some similarity with 5Ti and 10Ti, confirming them as building blocks of the microspheres. The size of the largest microsphere in 20Ti was 4.8 µm compared to 3.9 µm for 40Ti, the latter corresponding to a higher degree of ordering due to a higher number of small precipitates. The microspheres are maintained after heat treatment as shown by 40Ti_W, however, there is a clear formation of grain boundaries due to coalescence of particles during sintering.

4.3.6 X-ray photoelectron spectroscopy

The surface composition and states of selected samples (40Ti, 20Ti, 5Ti and 40Ti_W) were investigated by X-ray photoelectron spectroscopy (XPS).

Figure 4.49 presents the high resolution Ti2p spectra of the samples. The Ti $2p_{3/2}$ peak for the oxidation state of +4 is located at 458.61 eV, 458.47 eV, 458.44 eV and 458.39 eV for 5Ti, 20Ti, 40Ti and 40Ti_W, respectively [275][276].

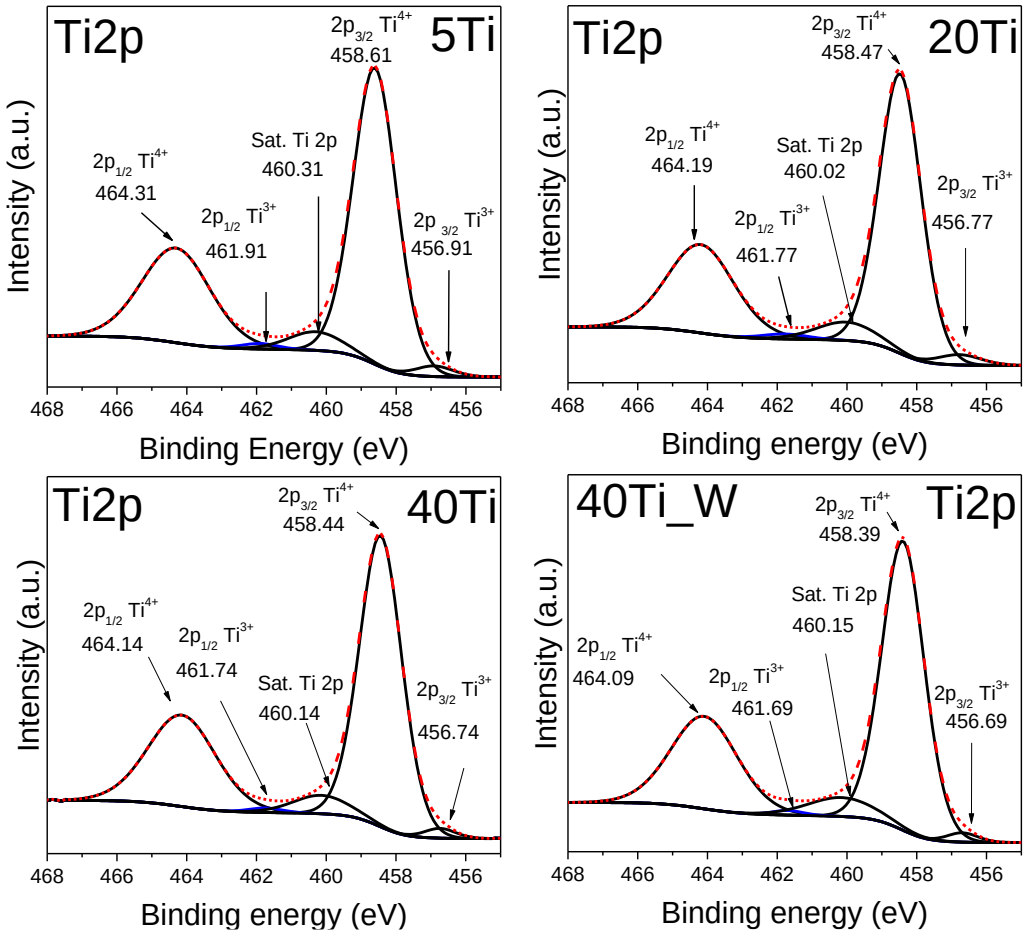

Figure 4.49 - Ti2p spectra of 5Ti, 20Ti, 40Ti and 40Ti_W.

The splitting energy between the Ti $2p_{3/2}$ and Ti $2p_{1/2}$ doublet was 5.7 eV in agreement with compiled data [277]. The binding energies of Ti(IV) ($2p_{1/2}$ and $2p_{3/2}$) shift slightly to lower values as the volume of titanium isopropoxide precursor increases, which point to reduction [278][279]. The quantification of Ti(IV) in the samples did not present a trend with volume of titanium isopropoxide precursor, 40Ti (92.6%) and 5Ti (92.3%) presented higher Ti(IV) quantities followed by 40Ti_W (91.6%) and 20Ti (90.9%). It is speculated that the degree of reduction of Ti(IV) species at the surface may determine the levels of Ti(IV), being higher for samples with lower degrees of reduction.

Although Ti(III) species were not identified by EPR, all the samples contain Ti(III) species as evidenced by the Ti(III) ($2p_{1/2}$ and $2p_{3/2}$) doublet (Figure 4.60).

This shows that EPR is more sensitive to the bulk region. The Ti ($2p_{3/2}$) peak for the oxidation state of +3 is present at 456.91 eV, 456.77 eV, 456.74 eV and 456.69 eV for samples 5Ti, 20Ti, 40Ti and 40Ti_W, respectively. The splitting energy between the Ti ($2p_{3/2}$) and Ti ($2p_{1/2}$) doublet was found to be 5 eV. Similar to the Ti(IV) analysis, a slight shift to lower binding energies was observed for the Ti(III) doublet ($2p_{1/2}$ and $2p_{3/2}$) indicating a reducing effect associated with an increase in titanium isopropoxide precursor. Apparently, the synthesis method has a potential of reducing Ti(IV) species.

The quantity of Ti(III) increases from 5Ti (2.9%) to 20Ti (3.5%) and then decreases from 40Ti (2.3%) to 40Ti_W (2.1%). Comparing this result to that of EPR, it is evident that the surface composition of the samples differs from the bulk. Thus, sample properties and performance will be defined by the synergism between surface and bulk oxygen vacancies.

Titanium satellites were present in the samples. They are formed when departing photoelectrons lose kinetic energy through the excitation of a valence electron to a higher bound state. According to Jonnard et al. (2005), satellites indicate double or multiply ionization of atoms [280]. The mechanisms behind satellite formation are summarized in Equations 4.16 and 4.17 [281]:

$$O(2p) \rightarrow Ti(4s) \tag{4.16}$$

$$O(2s) \rightarrow Ti(3d) \tag{4.17}$$

Sen et al. (1976) reported a separation energy of 5 eV between Ti $2p_{1/2}$ and Ti satellite peak [282]. In this thesis, the satellites of 5Ti, 20Ti, 40Ti and 40Ti_W are respectively centered at 460.31 eV, 460.02 eV, 460.14 eV and 460.15 eV corresponding to separation energies of 4 eV, 4.17 eV, 4 eV and 3.94 eV. Sample 40Ti_W has the highest level of Ti satellite (6.3%) followed by 20Ti (5.6%), 40Ti (5.4%) and 5Ti (4.8%). Since satellites are associated with multiple ionization, it is presumed that 40Ti_W is easily ionized compared to 5Ti.

Figure 4.50 presents the high resolution O 1s spectra of the samples. Three components are identified: O-Ti bonds (lattice oxygen), non-lattice oxygen bonds or Ti-OH and surface H_2O, in ascending order of energy [265][283]–[285]. Lattice oxygen bonds equivalent to O-Ti bonds occur at 529.86 eV, 529.69 eV, 529.74 eV and 529.62 eV for 5Ti, 20Ti, 40Ti and 40Ti_W, respectively. Samples

5Ti (54.48%) and 40Ti (55.85%) have the highest lattice oxygen whereas samples 20Ti (53.05%) and 40Ti_W (52.76%) have the lowest. The trend coincides with that of the Ti(IV) bonds, suggestive of lower surface reduction for samples with higher Ti(IV) and higher lattice oxygen levels.

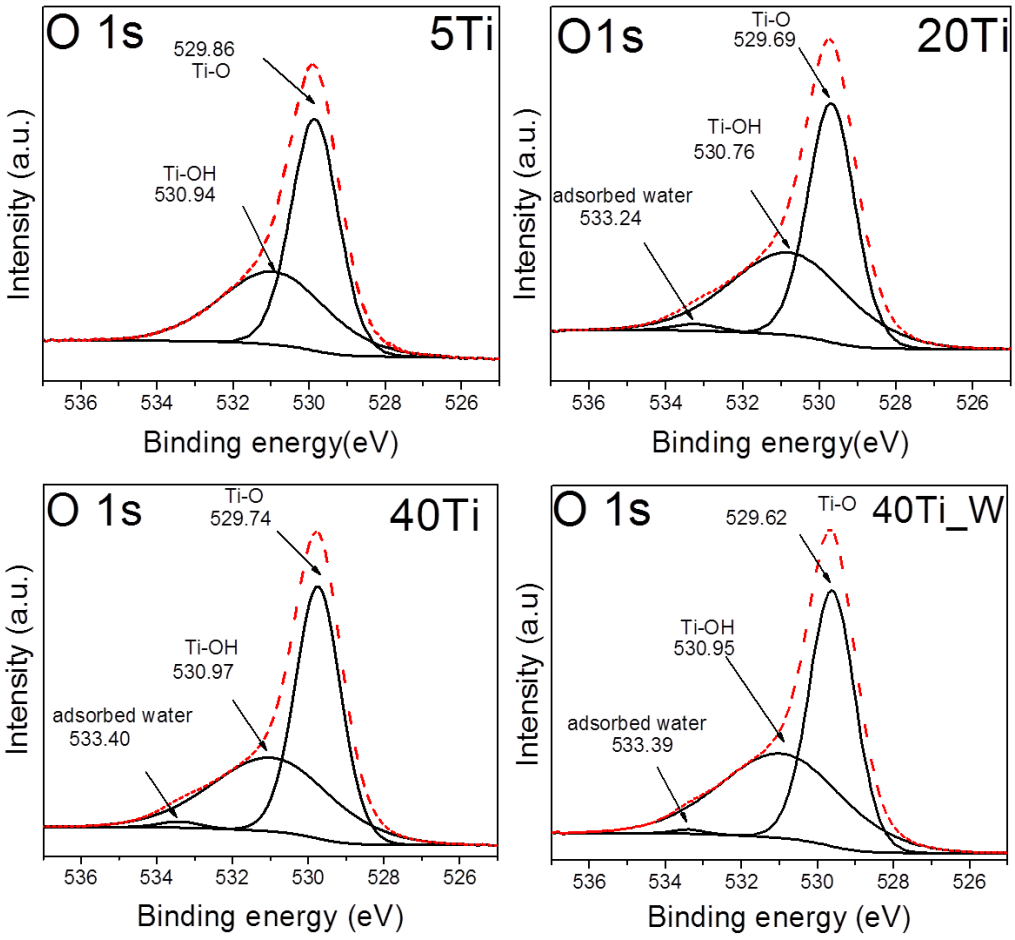

Figure 4.50 - O 1s spectra of 5Ti, 20Ti, 40Ti and 40Ti_W.

The peaks pertaining to non-lattice oxygen occur at 530.94 eV, 530.76 eV, 530.97 eV and 530.95 eV for 5Ti, 20Ti, 40Ti and 40Ti_W, respectively [286]. Non-lattice oxygen bonds can be described as oxygen atoms on hollow sites, thus their concentration can be linked to defects such as oxygen vacancies and/or dangling bonds [287].

Samples 40Ti_W (46.66%) and 20Ti (45.54%) presented higher levels of non-lattice oxygen while 40Ti (42.97%) and 5Ti (41.52%) presented lower levels, which is directly opposite to the trend found for lattice oxygen. This means that samples 40Ti_W and 20Ti have higher concentrations of oxygen vacancies and/or dangling bonds on the surface and consequently, lower surface Ti(IV).

Figure 4.51 presents the high resolution C1s spectra of the samples. For 5Ti, four components were identified. Adventitious carbon (284.60 eV), chemisorped CO_2 (286.02 eV), CO (288.64 eV) and TiC (282.81 eV) [288].

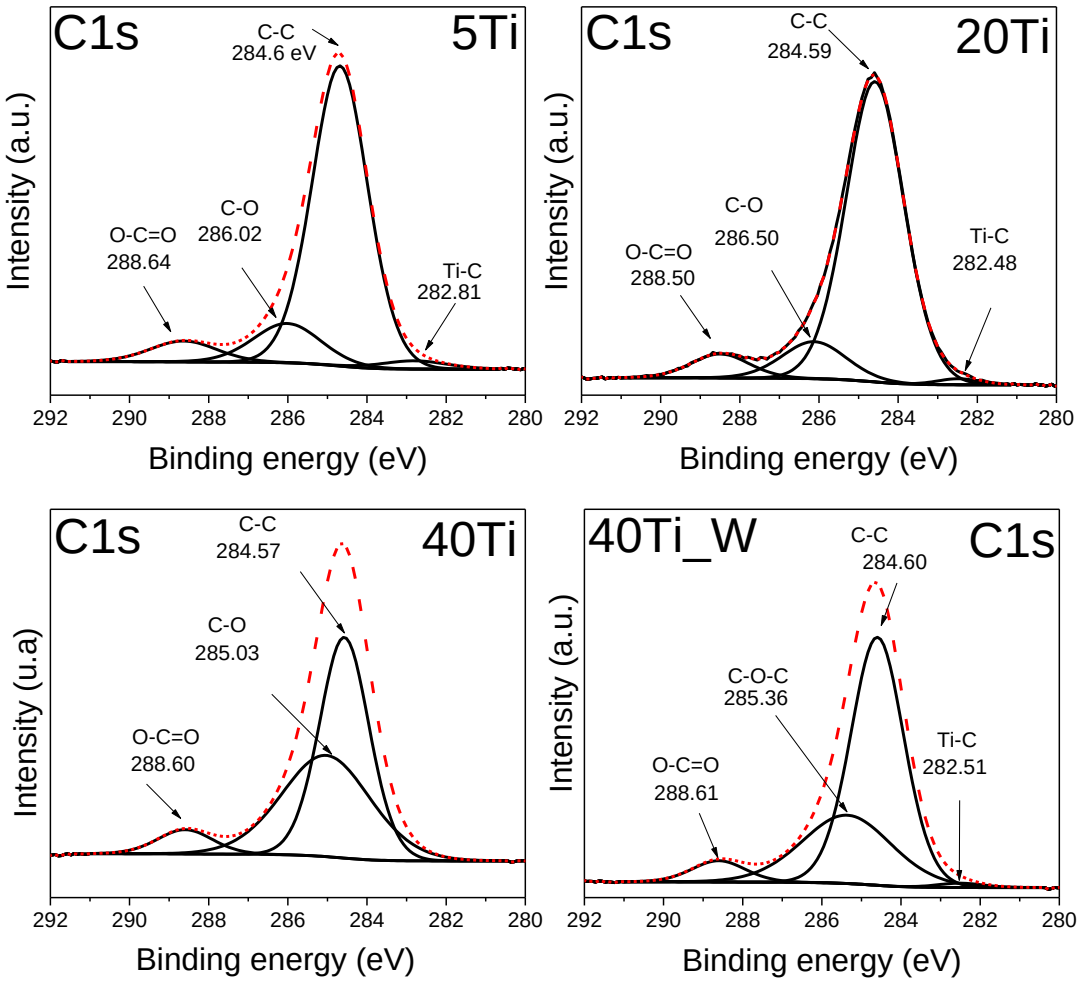

Figure 4.51 - C 1s spectra of 5Ti, 20Ti, 40Ti and 40Ti_W.

All the samples except 40Ti had titanium carbide. The contribution of carbon to the formation of surface oxygen vacancies is shown by the presence of titanium carbide. Accordingly, some oxygen atoms were substituted by carbon, causing the formation of oxygen vacancies. It also supports the hypothesis that carbon sources can provide a reducing environment during calcination.

Samples 5Ti (2.53%) presented the highest levels of TiC followed by 20Ti (1.18%) and 40Ti_W (0.94%). In general, the quantity of TiC decreased with increasing titanium precursor, which suggests that the level of carbon on the surface decreases with an increase in precipitation/hydrolysis. The precipitates can serve as nucleation sites, reducing the number of unreacted alkoxides.

It is rather strange that 40Ti did not have TiC on the surface although 40Ti_W was prepared from the same. A possible reason could be the further replacement of oxygen atoms with carbon trapped between particles during additional calcination. It is difficult to pinpoint the mechanism of carbide formation (500 ^{o}C) and its stability at high temperature (800 ^{o}C) given the synthesis conditions.

4.3.7 Photoluminescence

The effect of oxygen vacancies on the luminescence properties can be investigated by photoluminescence spectroscopy. The room temperature PL (355 nm excitation) spectra of the samples are presented in Figure 4.52. Due to the lack of emission around 378 nm characteristic of anatase bandgap, it is concluded that the emissions are not near band emissions [143]. Emissions centered at 512 nm (40Ti_W), 550 nm (40Ti), 580 nm (10Ti), 601 nm (5Ti) and 620 nm (20Ti) are present.

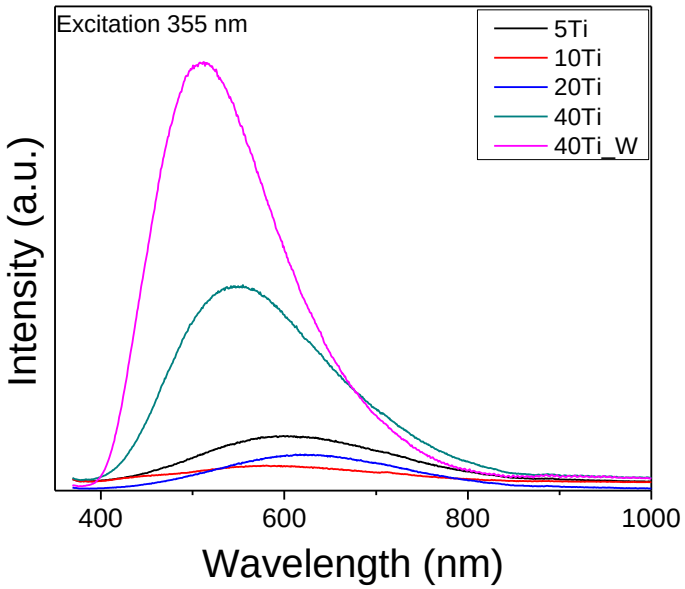

Figure 4.52 - Room temperature emission of 5Ti, 10Ti, 20Ti, 40Ti and 40Ti_W.

Emissions from 512 to 580 nm, also known as green emissions, are related to oxygen vacancies specifically F^{+} centers (singly charged oxygen vacancy) [289]–[292]. It can also be understood as the recombination of conduction band (cb) electrons with trapped (tr) holes, resulting in green emissions (Equation 4.18)

[291].

$$e_{cb}^{-} + h_{tr}^{+} \rightarrow hv_{green} \quad (4.18)$$

In general, the increase in non-radioactive contributions, that is, defects such as oxygen vacancies, quenches the PL intensity. This trend was shown by the decrease in green emissions (40Ti_W > 40Ti >10Ti) in line with the increase in oxygen vacancies as per EPR analysis. Because green emissions can be related to the recombination of conduction band electrons with trapped holes, a reduction in this emission can be associated with efficient charge separation with increase in oxygen vacancies.

Samples 5Ti (601 nm) and 20Ti (620 nm) presented red emissions. These emissions are suggestive of Ti(III) species and can be associated with the recombination of holes in the valence band (vb) with trapped (tr) electrons (Equation 4.19) [291].

$$h_{vb}^{+} + e_{tr}^{-} \rightarrow hv_{red} \quad (4.19)$$

Based on the PL intensity, 5Ti presents a greater recombination and lower levels of Ti(III) defects associated with oxygen vacancies when compared with 20Ti. This argument is backed by XPS analysis as well, where 20Ti presented higher levels of Ti(III) compared to 5Ti. Since all the samples contain Ti(III) species and oxygen vacancies, it is believed that the emissions observed are from the most dominant species.

In general, oxygen vacancies and Ti(III) species act as traps, reducing the recombination of charge carriers. Thus, an optimum level of both defects and synergism among them are important factors for efficient properties.

4.3.8 Fourier transform infrared (FTIR) spectroscopy

The FTIR spectra of the samples are shown in Figure 4.53. Subtle OH bands associated with water absorption can be observed. The formation of TiO_2 is confirmed through vibrations at 480 cm^{-1}, characteristic of Ti-O [293]. The band at 1384 cm^{-1} present in all samples is assigned to C-H bending related to the Ti-isopropoxide precursor [294]. Its intensity decreased with increasing volume of Ti-isopropoxide, suggesting a decrease in surface residual carbon.

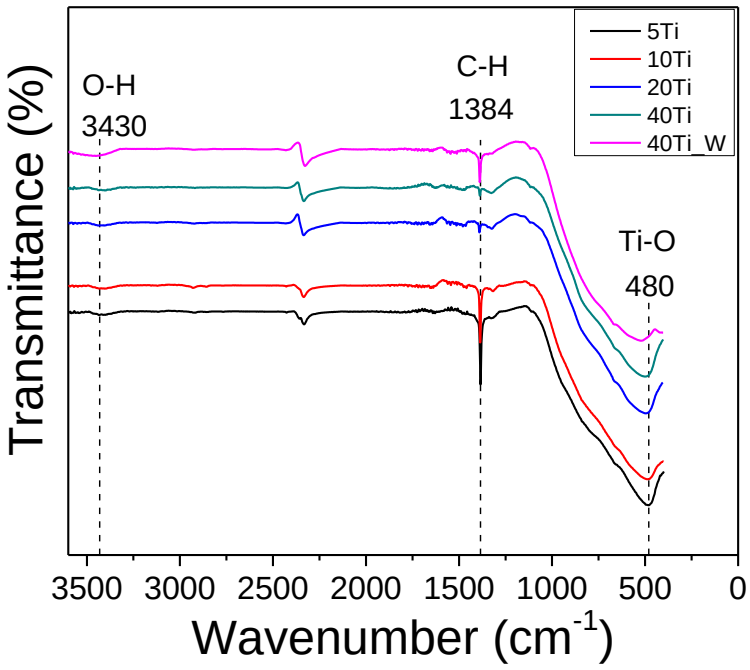

Figure 4.53 - FTIR spectra of 5Ti, 10Ti, 20Ti, 40Ti and 40Ti_W.

From the trend observed, the samples containing mostly microspheres such as 20Ti and 40Ti (FEG-SEM images) had lower surface C-H bonds while 5Ti and 10Ti with agglomerates presented higher surface C-H bonds. Increasing the volume of Ti precursor while maintaining the quantity of HCl and isopropanol reduces the stability of the sol through rapid precipitation/hydrolysis of titanium hydroxide particles. In this case, unreacted alkoxy groups can be greater in lower volumes of titanium isopropoxide, resulting in higher C-H bonds on the surface.

4.3.9 Bandgap

The presence of oxygen defects can create local states within the bandgap of the samples, which extend absorption into the visible region. Figure 4.54 A and B presents the absorption spectra and bandgap extrapolation of the samples based on the Kubelka-Munk function for an indirect bandgap material, respectively.

Figure 4.54 B shows the bandgaps of the samples extrapolated from the Kubelka-Munk function graphs for an indirect bandgap material. The samples with lower volumes of titanium isopropoxide had lower bandgaps, 10Ti (2.72 eV) and 5Ti (2.94 eV), and those with higher volumes presented higher bandgaps, 20Ti (3.01 eV) and 40Ti (3.08 eV). 40Ti_W calcined at a higher temperature

presents a lower bandgap (2.91 eV) compared to 40Ti (3.08 eV).

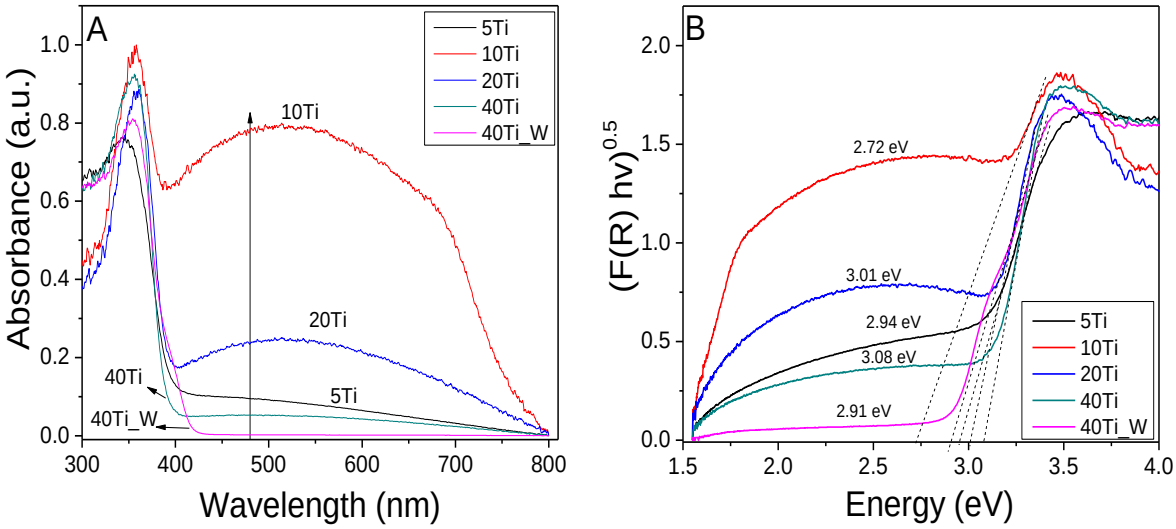

Figure 4.54 - A) Kubelka-Munk function derived from diffuse reflectance measurements and B) extrapolation of bandgap from Kubelka-Munk function for an indirect bandgap material.

The valence band maximum and conduction band minimum of TiO_2 are derived mainly from the O 2p and Ti 3d orbitals, respectively [295]. Thus, the increase or decrease in bandgap can be attributed to the combined contribution of Ti(III) species and oxygen vacancies in the samples.

The absorption at 450 nm increases in this trend, 40Ti_W, 40Ti, 5Ti, 20Ti and 10Ti, which is in agreement with decrease in PL intensity associated with defects. This means oxygen vacancies/Ti(III) enhance absorption in the visible region and lower PL intensity. Clearly, oxygen vacancies can aid the visible response of TiO_2 and their optimum level is important for effective reduction of recombination.

4.3.10 Photoactivity

The photocatalytic activity of the samples was tested under visible light for 4 hours using Amiloride solution (5 mg/L). Figure 4.55 shows the reduction of the concentration of Amiloride under visible light irradiation in the presence of the oxygen-deficient TiO_2 samples. The pure Amiloride solution with no sample showed insignificant activity, indicating negligible photolysis. The reduction of Amiloride concentration is then related to sample properties and irradiation.

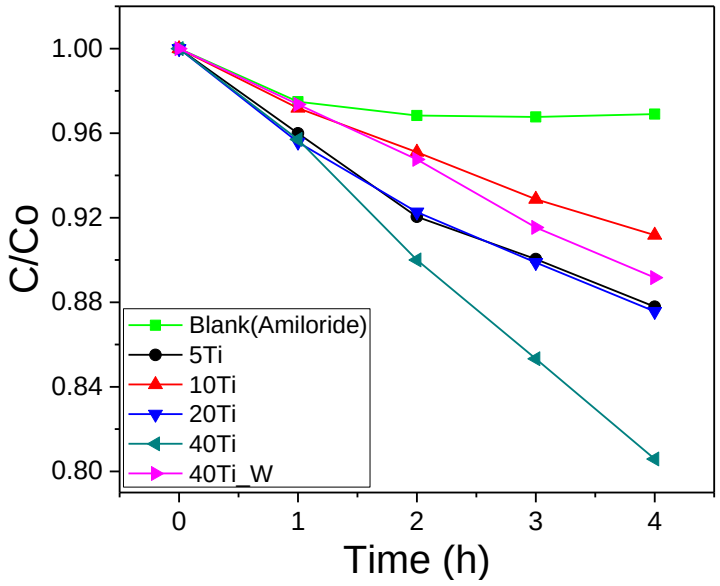

Figure 4.55 - Photodegradation of Amiloride in the presence of 5Ti, 10Ti, 20Ti, 40Ti and 40Ti_W.

In general, the samples exhibited low activity with a reduction of 12.2%, 10.8%, 12.4%, 19.4% and 8.8% for sample 5Ti, 10Ti, 20Ti, 40Ti and 40Ti_W, respectively. A possible reason could be the low stability of surface oxygen vacancies. The micrometric nature of the powders may have interfered with photoactivity since the reactivity of nanometric powders are superior.

When the activity of 40Ti and 40Ti_W is compared, it can be seen that the sample with greater oxygen vacancies (40Ti) as per EPR presents a higher photoactivity. Oxygen vacancies can influence visible light response, charge separation and/or recombination. From the PL analysis, 40Ti_W presents the highest intensity which is translated as lower density of defects that can participate in charge separation mechanisms. Despite the lower bandgap of 40Ti_W, its activity was not comparable to 40Ti. This suggests that the excess photons absorbed do not effectively contribute to photoactivity.

For the samples with different volumes of titanium isopropoxide, 40Ti presented the highest activity followed by 20Ti, 5Ti and 10Ti. The trend is consistent with high volume of titanium isopropoxide except for 5Ti and 10Ti, which indicates an important influence of titanium ions irrespective of defects. Considering the levels of oxygen defects, 10Ti and 20Ti were expected to have higher activities compared to 40Ti and 5Ti. However, since the samples contain

both surface and bulk oxygen vacancies, the synergy between them should be considered. According to Pan et al. (2013), surface oxygen vacancies are not stable and susceptible to oxidation through dissolved oxygen in water [188]. In contrast, bulk oxygen vacancies are more stable but can serve as recombination sites.

Among the samples, the higher the bandgap, the lower the photocatalytic activity. Although a lower bandgap is beneficial for visible activity, recombination can be promoted as the potential energy of charge carriers are lower. Thus, absorption in the visible region alone is not sufficient for the improvement of photoactivity. Other factors such as recombination and trapping dynamics are equally important.

4.3.11 Electrochemical analysis

To study the charge separation of the samples, impedance and transient photocurrent measurements under visible illumination were conducted. Figure 4.56 presents the Nyquist plots and Randles circuit (Insert) of the samples.

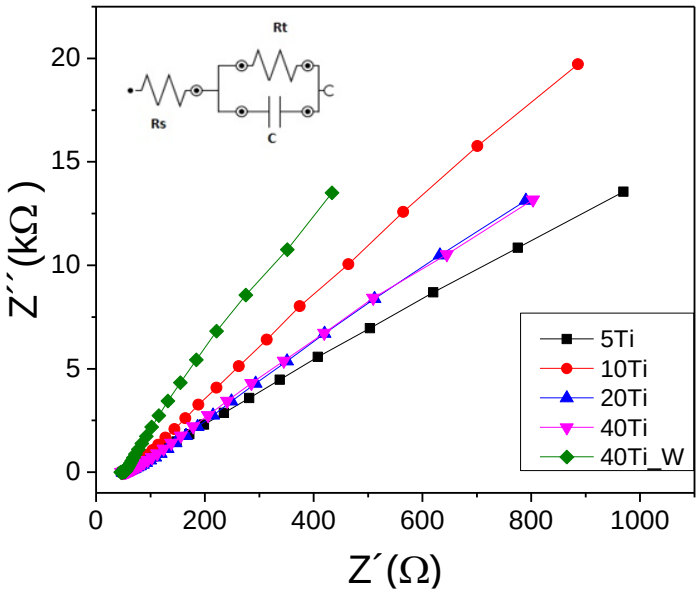

Figure 4.56 - Nyquist plot of 5Ti, 10Ti, 20Ti, 40Ti and 40Ti_W. Insert: Randles circuit.

The circuit includes a solution resistance (Rs), a double layer capacitor (C) and a charge transfer resistance (Rt). The values of the circuit elements are shown in Table 4.4.

Table 4.4 - Lattice parameters of 5Ti, 10Ti, 20Ti, 40Ti and 40Ti_W.

Sample	Rs(Ω)	Rt(kΩ)	C(μF)
5Ti	52.3	117	10.6
10Ti	52.6	266	7.5
20Ti	49.9	130	10.9
40Ti	48.3	281	11.4
40Ti_W	52.5	129	11.0

Since the electrolyte utilized was equivalent for all samples, the solution resistance was expected to be within the same range. For charge transfer resistance, the trend was as follows: 40Ti > 10Ti > 20Ti > 40Ti_W > 5Ti. From the EPR, XPS and PL analyses, the samples present a mixture of defects (Ti(III) and oxygen vacancies) and they vary in the bulk and surface. Thus, an optimum combination is beneficial for electron transfer.

Double layer capacitance describes the system's ability to store charges at the electrode/electrolyte interface. This storage can be related to oxygen vacancies on the surface which can participate in current generation when appropriate voltage is applied [296]. The sample with the highest capacitance was 40Ti followed by 40Ti_W, 20Ti, 5Ti and 10Ti. With the exception of 40Ti_W, the trend is in agreement with photocatalytic activity. It emphasizes the role of surface charges on adsorption and consequently, photocatalytic activity.

Photocurrent under light and dark cycles for all samples is presented in Figure 4.57.

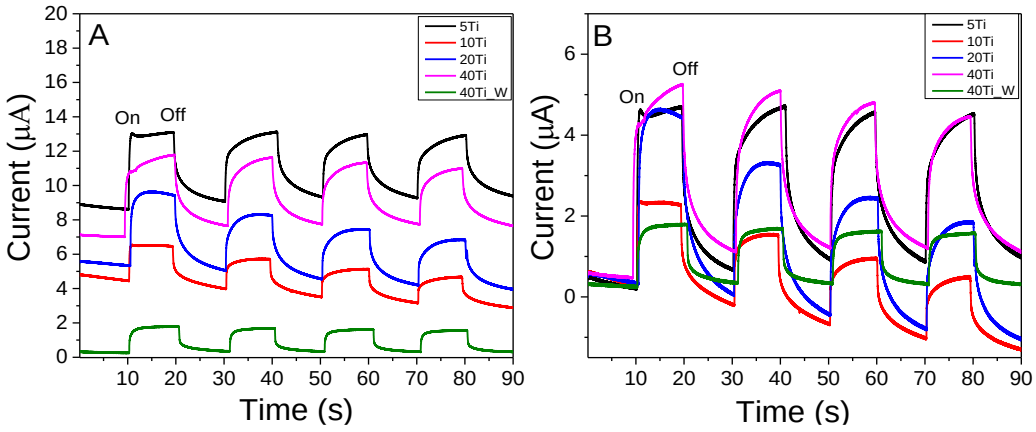

Figure 4.57 - A) Photocurrent response of 5Ti, 10Ti, 20Ti, 40Ti and 40Ti_W and B) photocurrent response translated to facilitate the analysis of current variation.

The photocurrent responses of the samples were probed under light and dark cycles with a bias potential of 1.2 V. To facilitate the analysis of the samples, they were all translated to the value of sample 40Ti_W. Thus, the variation of photocurrent was considered. The responses of samples 5Ti, 40Ti and 40Ti_W were consistent with time compared to 20Ti and 10Ti, which can be associated with better chemical and photo-stability. A slow decay of the dark current is observed for all samples, indicating the effect of trapped charge carriers on carrier lifetime [297].

With regard to 40Ti and 40Ti_W, the photocurrent of the latter is lower despite having a lower charge transfer resistance, suggesting that the presence of oxygen vacancies improves charge separation and lifetime of photogenerated carriers. In this case, there is a variation in charge transfer resistance under illumination associated with limited number of defects for charge separation. The finding is also consistent with the photocatalytic trend.

For the samples with different volumes of Ti isopropoxide, 40Ti presented the highest photocurrent followed by 5Ti, 20Ti and 10Ti. The samples with the highest levels of defects as per EPR analysis (20Ti and 10Ti) had lower photocurrents. The sequence of photocurrent reduction follows a decrease in PL intensity. The PL analysis showed a predominance of Ti(III) (20Ti and 5Ti) and oxygen vacancy (40Ti and 10Ti) in emission quenching. The decrease in PL indicates efficient separation of charges through defects. Therefore, it is expected that the samples with the lowest PL intensity would have the highest photocurrent. As this did not occur, we assume that in addition to charge separation, the number of free electrons (not trapped) and the half-life of charges before recombination can be influential factors. With these considerations, an increase in the density of the traps can decrease the number of free electrons which in turn reduces photocurrent. Therefore, there is an optimum level of defects for efficient separation for photocurrent production as well as optimum free electrons. Among the samples, 40Ti and 5Ti appear to have a good combination of these properties.

5 CONCLUSION

5.1 Tin perovskites

Based upon the experimental conditions adopted in this thesis, it is possible to conclude that tin perovskites can be doped with Mn in a proportion of up to 10% mol without disrupting the perovskite structure. The bandgap of tin perovskite can be modified with Mn doping either through formation of discrete levels or changes in valence band energy. Doping tin perovskites with chlorine containing precursors can result in unintentional residual chlorine. Doping tin perovskite with 10% Mn can partially improve stability according to X-ray diffraction patterns collected after 24 h. Although Mn improves stability, the photovoltaic parameters of tin perovskite reduced with Mn doping. It is important to note that the solar cells were not optimized, thus Mn doping alone cannot be blamed for the poor performance.

The electrochemical properties of tin perovskites can be investigated in aqueous media with the help of a PLA layer, however the method must be complemented with other techniques. From the electrochemical analysis, Mn increases the resistance of tin perovskite, which is detrimental to photovoltaic properties. According to chronoamperometry measurements, 10% Mn and 2% Mn improve the stability of tin perovskite.

Tin (II) octoate and $SnSO_4$ can be used as alternative tin precursors for the synthesis of tin perovskites, provided the mole ratio of methylammonium iodide to non-halide precursor is at least 3:1, respectively. A temperature of 110 ^oC/10 min is sufficient for the formation of tin perovskites derived from non-halide precursors, but a higher temperature (150 ^oC) aids in crystallization and reduction of residues associated with the precursors.

$SnSO_4$ appears to slow the crystallization of tin perovskite as evidenced by large grains. Sulfur can unintentionally dope the perovskite, which can affect the properties of the perovskite. The use of tin octoate containing carbon atoms can cause segregation.

Residues are always present when non-halide tin precursors are utilized, thus their effects should be taken into consideration.

5.2 Oxygen-deficient TiO_2

The synthesis of oxygen-deficient TiO_2 based on calcination in air requires a localized reducing atmosphere. A combination of Isopropanol, Ti-isopropoxide and HCl can provide an in-situ reducing atmosphere for the formation of oxygen vacancies through unreacted alkoxides and/or CH_3 species.

The concentration of titanium isopropoxide controls precipitation/ hydrolysis as well as particle assembly, factors which directly affect the level of unreacted alkoxides and/or CH_3 species.

Carbon atoms can replace oxygen atoms on the surface during calcination to form TiC, contributing to the formation of oxygen vacancies. The contribution of TiC increases with increase in titanium isopropoxide concentration.

There exists an optimum level of oxygen vacancies, above which recombination becomes dominant, reducing photocatalytic activity and photocurrent. Poor photocatalytic activity of oxygen-deficient TiO_2 can be associated with size factors and stability of the oxygen vacancies.

6 SUGGESTIONS FOR FUTURE STUDIES

The thesis presented the synthesis and characterization of tin perovskites and Mn doped tin perovskites. Futhermore, it presented the potential of tin octoate and tin sulfate as precursors for the synthesis of tin perovskites.

A future research project is the development of tin perovskite solar cells based on halide and non-halide tin precursors. For instance, improving efficiency through the control and optimization of morphology and testing of alternative hole transport materials.

Manganese as a dopant of tin perovskites was shown to reduce the efficiency of tin perovskite solar cells. However, emphasis was not laid on the development of Mn doped tin perovskite solar cell, thus necessary optimization of the solar cell components was not conducted. In this case, one can investigate the optimum concentration of Mn for both efficiency and stability.

A new method for the electrochemical measurement of perovskites using a polymer layer was introduced. It should be possible to realize electrochemical measurements using different polymers.

As regards the synthesis of oxygen-deficient TiO_2 materials, the effect of varying HCl concentration as well as the use of other titanium dioxide precursors can be investigated.

Finally, future efforts can be directed towards integrating oxygen-deficient TiO_2 and selected Sn perovskites, aiming to increase performance.

7 REFERENCES

[1] M. Grätzel, “Dye-sensitized solar cells,” *J. Photochem. Photobiol. C Photochem. Rev.*, vol. 4, no. 2, pp. 145–153, 2003, doi: 10.1016/S1389-5567(03)00026-1.

[2] S. A. Bretschneider, J. Weickert, J. A. Dorman, and L. Schmidt-Mende, “Research Update: Physical and electrical characteristics of lead halide perovskites for solar cell applications,” *APL Mater.*, vol. 2, no. 4, p. 40701, Apr. 2014, doi: 10.1063/1.4871795.

[3] C. C. Stoumpos, C. D. Malliakas, and M. G. Kanatzidis, “Semiconducting Tin and Lead Iodide Perovskites with Organic Cations: Phase Transitions, High Mobilities, and Near-Infrared Photoluminescent Properties,” *Inorg. Chem.*, vol. 52, no. 15, pp. 9019–9038, Aug. 2013, doi: 10.1021/ic401215x.

[4] G. Bye and B. Ceccaroli, “Solar grade silicon: Technology status and industrial trends,” *Sol. Energy Mater. Sol. Cells*, vol. 130, pp. 634–646, 2014, doi: 10.1016/j.solmat.2014.06.019.

[5] Z. Dong and Y. Lin, “Ultra-thin wafer technology and applications: A review,” *Mater. Sci. Semicond. Process.*, vol. 105, p. 104681, 2020, doi: 10.1016/j.mssp.2019.104681.

[6] M. A. Mingsukang, M. H. Buraidah, and A. K. Arof, “Third-Generation-Sensitized Solar Cells,” in *Nanostructured Solar Cells*, N. Das, Ed. Rijeka: IntechOpen, 2017, p. Ch. 2.

[7] L. M. Herz, “Charge-Carrier Mobilities in Metal Halide Perovskites: Fundamental Mechanisms and Limits,” *ACS Energy Lett.*, vol. 2, no. 7, pp. 1539–1548, Jul. 2017, doi: 10.1021/acsenergylett.7b00276.

[8] P. Umari, E. Mosconi, and F. De Angelis, “Relativistic GW calculations on $CH_3NH_3PbI_3$ and $CH_3NH_3SnI_3$ Perovskites for Solar Cell Applications,” *Sci. Rep.*, vol. 4, no. 1, p. 4467, 2014, doi: 10.1038/srep04467.

[9] NREL, “Best Research-Cell Efficiency Chart (National Renewable

Energy Laboratory, 2021)," 2021. https://www.nrel.gov/pv/assets/pdfs/cell-pv-eff-emergingpv-rev210726.pdf (accessed Jun. 10, 2021).

[10] W. E. I. Sha, X. Ren, L. Chen, and W. C. H. Choy, "The efficiency limit of $CH_3NH_3PbI_3$ perovskite solar cells," *Appl. Phys. Lett.*, vol. 106, no. 22, p. 221104, 2015, doi: 10.1063/1.4922150.

[11] L. M. Pazos-Outón, T. P. Xiao, and E. Yablonovitch, "Fundamental Efficiency Limit of Lead Iodide Perovskite Solar Cells," *J. Phys. Chem. Lett.*, vol. 9, no. 7, pp. 1703–1711, Apr. 2018, doi: 10.1021/acs.jpclett.7b03054.

[12] A. Kojima, K. Teshima, Y. Shirai, and T. Miyasaka, "Organometal Halide Perovskites as Visible-Light Sensitizers for Photovoltaic Cells," *J. Am. Chem. Soc.*, vol. 131, no. 17, pp. 6050–6051, May 2009, doi: 10.1021/ja809598r.

[13] J.-H. Im, C.-R. Lee, J.-W. Lee, S.-W. Park, and N.-G. Park, "6.5% efficient perovskite quantum-dot-sensitized solar cell," *Nanoscale*, vol. 3, no. 10, pp. 4088–4093, 2011, doi: 10.1039/C1NR10867K.

[14] H.-S. Kim *et al.*, "Lead Iodide Perovskite Sensitized All-Solid-State Submicron Thin Film Mesoscopic Solar Cell with Efficiency Exceeding 9%," *Sci. Rep.*, vol. 2, p. 591, Aug. 2012, doi: 10.1038/srep00591.

[15] O. Benedict, "A responsible compromise?," 2019. https://www.pv-magazine.com/2019/11/16/the-weekend-read-a-responsible-compromise/ (accessed Nov. 20, 2019).

[16] H.-Y. Hsu, L. Ji, M. Du, J. Zhao, E. T. Yu, and A. J. Bard, "Optimization of Lead-free Organic–inorganic Tin(II) Halide Perovskite Semiconductors by Scanning Electrochemical Microscopy," *Electrochim. Acta*, vol. 220, pp. 205–210, Dec. 2016, doi: 10.1016/j.electacta.2016.10.049.

[17] P.-P. Sun, Q.-S. Li, L.-N. Yang, and Z.-S. Li, "Theoretical insights into a potential lead-free hybrid perovskite: substituting Pb^{2+} with Ge^{2+}," *Nanoscale*, vol. 8, no. 3, pp. 1503–1512, 2016, doi:

10.1039/C5NR05337D.

[18] I. Benabdallah, M. Boujnah, A. El Kenz, A. Benyoussef, M. Abatal, and A. Bassam, “Lead-free perovskite based bismuth for solar cells absorbers,” *J. Alloys Compd.*, vol. 773, pp. 796–801, 2019, doi: 10.1016/j.jallcom.2018.09.332.

[19] T.-W. Lin, C. Su, and C. C. Lin, “Phase transition and energy transfer of lead-free Cs_2SnCl_6 perovskite nanocrystals by controlling the precursors and doping manganese ions,” *J. Inf. Disp.*, vol. 20, no. 4, pp. 209–216, 2019, doi: 10.1080/15980316.2019.1655493.

[20] D. Agustin and M. Ehses, “ChemInform Abstract: 119Sn NMR Spectroscopic and Structural Properties of Transition Metal Complexes with Terminal Stannylene Ligands,” *Comptes Rendus Chim.*, vol. 10, pp. 1189–1227, Oct. 2009, doi: 10.1016/j.crci.2009.04.004.

[21] R. D. Shannon, “Revised effective ionic radii and systematic studies of interatomic distances in halides and chalcogenides,” *Acta Crystallogr. Sect. A*, vol. 32, no. 5, pp. 751–767, Sep. 1976, doi: 10.1107/S0567739476001551.

[22] S. Rühle, “Tabulated values of the Shockley–Queisser limit for single junction solar cells,” *Sol. Energy*, vol. 130, pp. 139–147, 2016, doi: 10.1016/j.solener.2016.02.015.

[23] E. Jokar, C.-H. Chien, C.-M. Tsai, A. Fathi, and E. W.-G. Diau, “Robust Tin-Based Perovskite Solar Cells with Hybrid Organic Cations to Attain Efficiency Approaching 10%,” *Adv. Mater.*, vol. 31, no. 2, p. 1804835, Jan. 2019, doi: 10.1002/adma.201804835.

[24] N. K. Noel *et al.*, “Lead-free organic-inorganic tin halide perovskites for photovoltaic applications,” *Energy Environ. Sci.*, vol. 7, no. 9, pp. 3061–3068, 2014, doi: 10.1039/C4EE01076K.

[25] T. Leijtens, R. Prasanna, A. Gold-Parker, M. F. Toney, and M. D. McGehee, “Mechanism of Tin Oxidation and Stabilization by Lead Substitution in Tin Halide Perovskites,” *ACS Energy Lett.*, vol. 2,

no. 9, pp. 2159–2165, Sep. 2017, doi: 10.1021/acsenergylett.7b00636.

[26] M. Konstantakou and T. Stergiopoulos, “A critical review on tin halide perovskite solar cells,” *J. Mater. Chem. A*, vol. 5, pp. 11518–11549, 2017, doi: 10.1039/C7TA00929A.

[27] S. Gupta, D. Cahen, and G. Hodes, “How SnF_2 Impacts the Material Properties of Lead-Free Tin Perovskites,” *J. Phys. Chem. C*, vol. 122, no. 25, pp. 13926–13936, Jun. 2018, doi: 10.1021/acs.jpcc.8b01045.

[28] Y. Takahashi *et al.*, “Charge-transport in tin-iodide perovskite $CH_3NH_3SnI_3$: origin of high conductivity,” *Dalt. Trans.*, vol. 40, no. 20, pp. 5563–5568, 2011, doi: 10.1039/C0DT01601B.

[29] M. Ozaki *et al.*, “Solvent-Coordinated Tin Halide Complexes as Purified Precursors for Tin-Based Perovskites,” *ACS Omega*, vol. 2, no. 10, pp. 7016–7021, Oct. 2017, doi: 10.1021/acsomega.7b01292.

[30] F. Hao, C. C. Stoumpos, D. H. Cao, R. P. H. Chang, and M. G. Kanatzidis, “Lead-free solid-state organic-inorganic halide perovskite solar cells,” *Nat Phot.*, vol. 8, no. 6, pp. 489–494, Jun. 2014, doi: 10.1038/nphoton.2014.82.

[31] Sigma-Aldrich, “Product Comparison Guide,” 2019. https://www.sigmaaldrich.com/catalog/substance/tiniiiodide372521029470911?lang=en&region=US (accessed Dec. 27, 2019).

[32] Sigma-Aldrich, “Price of Tin(II) sulfate,” 2019. https://www.sigmaaldrich.com/catalog/search?term=snso4&interface=All&N=0&mode=match partialmax&lang=en&region=US&focus=product (accessed Dec. 27, 2019).

[33] Sigma-Aldrich, “Price of Tin(II) octoate,” 2019. https://www.sigmaaldrich.com/catalog/product/aldrich/s3252?lang=en&region=US (accessed Dec. 27, 2019).

[34] E. S. Parrott, R. L. Milot, T. Stergiopoulos, H. J. Snaith, M. B.

Johnston, and L. M. Herz, “Effect of Structural Phase Transition on Charge-Carrier Lifetimes and Defects in $CH_3NH_3SnI_3$ Perovskite,” *J. Phys. Chem. Lett.*, vol. 7, no. 7, pp. 1321–1326, Apr. 2016, doi: 10.1021/acs.jpclett.6b00322.

[35] F. Wang *et al.*, “Organic Cation-Dependent Degradation Mechanism of Organotin Halide Perovskites,” *Adv. Funct. Mater.*, vol. 26, no. 20, pp. 3417–3423, May 2016, doi: 10.1002/adfm.201505127.

[36] C. Liu, J. Fan, H. Li, C. Zhang, and Y. Mai, “Highly Efficient Perovskite Solar Cells with Substantial Reduction of Lead Content,” *Sci. Rep.*, vol. 6, p. 35705, Oct. 2016, doi: 10.1038/srep35705.

[37] S. J. Lee *et al.*, “Fabrication of Efficient Formamidinium Tin Iodide Perovskite Solar Cells through SnF_2–Pyrazine Complex,” *J. Am. Chem. Soc.*, vol. 138, no. 12, pp. 3974–3977, Mar. 2016, doi: 10.1021/jacs.6b00142.

[38] W. Liao *et al.*, “Lead-Free Inverted Planar Formamidinium Tin Triiodide Perovskite Solar Cells Achieving Power Conversion Efficiencies up to 6.22%,” *Adv. Mater.*, vol. 28, no. 42, pp. 9333–9340, Nov. 2016, doi: 10.1002/adma.201602992.

[39] Y. Li *et al.*, “50% Sn-Based Planar Perovskite Solar Cell with Power Conversion Efficiency up to 13.6%,” *Adv. Energy Mater.*, vol. 6, no. 24, pp. 1601353-n/a, Dec. 2016, doi: 10.1002/aenm.201601353.

[40] D. Zhao *et al.*, “Low-bandgap mixed tin–lead iodide perovskite absorbers with long carrier lifetimes for all-perovskite tandem solar cells,” *Nat. Energy*, vol. 2, p. 17018, Mar. 2017, doi: 10.1038/nenergy.2017.18.

[41] B. Zhao *et al.*, “High Open-Circuit Voltages in Tin-Rich Low-Bandgap Perovskite-Based Planar Heterojunction Photovoltaics,” *Adv. Mater.*, vol. 29, no. 2, pp. 1604744-n/a, Jan. 2017, doi: 10.1002/adma.201604744.

[42] K. Kobayashi, H. Hasegawa, Y. Takahashi, J. Harada, and T. Inabe, “Electronic properties of tin iodide hybrid perovskites: effect of indium doping,” *Mater. Chem. Front.*, vol. 2, no. 7, pp. 1291–1295, 2018, doi: 10.1039/C7QM00587C.

[43] J. Yuan, B. Li, and C. Hao, “Study on cobalt doped tin based perovskite material with enhanced air stability,” *Mater. Sci. Semicond. Process.*, vol. 57, pp. 95–98, 2017, doi: 10.1016/j.mssp.2016.09.029.

[44] H. Hasegawa, K. Kobayashi, Y. Takahashi, J. Harada, and T. Inabe, “Effective band gap tuning by foreign metal doping in hybrid tin iodide perovskites,” *J. Mater. Chem. C*, vol. 5, no. 16, pp. 4048–4052, 2017, doi: 10.1039/C7TC00446J.

[45] L. Dimesso, “Influence of the anion nature on the properties of Sr-containing formamidinium tin halide perovskites,” *J. Mater. Res.*, vol. 33, no. 24, pp. 4144–4155, 2018, doi: 10.1557/jmr.2018.412.

[46] L. A.-D. Dimesso Lucangelo A4 - Das, Chittaranjan A4 - Mayer, Thomas A4 - Jaegermann, Wolfram, “Investigation of earth-alkaline (EA = Mg, Ca, Sr) containing methylammonium tin iodide perovskite systems,” *J. Mater. Sci.*, vol. v. 53, no. 1, pp. 356-368–2018 v.53 no.1, 2018, doi: 10.1007/s10853-017-1545-0.

[47] M.-G. Ju, J. Dai, L. Ma, and X. C. Zeng, “Lead-Free Mixed Tin and Germanium Perovskites for Photovoltaic Application,” *J. Am. Chem. Soc.*, vol. 139, no. 23, pp. 8038–8043, Jun. 2017, doi: 10.1021/jacs.7b04219.

[48] S. Nagane *et al.*, “Lead-Free Perovskite Semiconductors Based on Germanium–Tin Solid Solutions: Structural and Optoelectronic Properties,” *J. Phys. Chem. C*, vol. 122, no. 11, pp. 5940–5947, Mar. 2018, doi: 10.1021/acs.jpcc.8b00480.

[49] N. Ito *et al.*, “Mixed Sn–Ge Perovskite for Enhanced Perovskite Solar Cell Performance in Air,” *J. Phys. Chem. Lett.*, vol. 9, no. 7, pp. 1682–1688, Apr. 2018, doi: 10.1021/acs.jpclett.8b00275.

[50] K. Oshima, *Science of Synthesis: Houben-Weyl Methods of*

Molecular Transformation , Vol. 2 : Compounds of Group 3-7 (Mn.., Cr..,V.., Ti.., Sc.., La.., Ac..), vol. 2. Stuttgart: Georg Thieme Verlag, 2003.

[51] J. Liang *et al.*, “Enhancing Optical, Electronic, Crystalline, and Morphological Properties of Cesium Lead Halide by Mn Substitution for High-Stability All-Inorganic Perovskite Solar Cells with Carbon Electrodes,” *Adv. Energy Mater.*, vol. 8, no. 20, p. 1800504, 2018, doi: 10.1002/aenm.201800504.

[52] W. J. Mir, A. Swarnkar, and A. Nag, “Postsynthesis Mn-doping in $CsPbI_3$ nanocrystals to stabilize the black perovskite phase,” *Nanoscale*, vol. 11, no. 10, pp. 4278–4286, 2019, doi: 10.1039/C9NR00248K.

[53] S. Zou *et al.*, “Stabilizing Cesium Lead Halide Perovskite Lattice through Mn(II) Substitution for Air-Stable Light-Emitting Diodes,” *J. Am. Chem. Soc.*, vol. 139, no. 33, pp. 11443–11450, Aug. 2017, doi: 10.1021/jacs.7b04000.

[54] L. Ren *et al.*, “Doped Manipulation of Photoluminescence and Carrier Lifetime from $CH_3NH_3PbI_3$ Perovskite Thin Films,” *ACS Appl. Mater. Interfaces*, vol. 11, no. 17, pp. 16174–16180, May 2019, doi: 10.1021/acsami.9b01506.

[55] A. Fujishima and K. Honda, “Electrochemical Photolysis of Water at a Semiconductor Electrode,” *Nature*, vol. 238, no. 5358, pp. 37–38, 1972, doi: 10.1038/238037a0.

[56] J. Moan, “7 Visible Light and UV Radiation,” *Radiat. Home, Outdoors Work.*, Jan. 2001.

[57] A. Zaleska, “Doped-TiO_2: A Review,” *Recent Patents on Engineering*, vol. 2, no. 3. pp. 157–164, 2008, doi: 10.2174/187221208786306289.

[58] S. B. Rawal, S. Bera, D. Lee, D.-J. Jang, and W. I. Lee, “Design of visible-light photocatalysts by coupling of narrow bandgap semiconductors and TiO_2: effect of their relative energy band positions on the photocatalytic efficiency,” *Catal. Sci. Technol.*,

vol. 3, no. 7, pp. 1822–1830, 2013, doi: 10.1039/C3CY00004D.

[59] J. Nowotny *et al.*, “Defect chemistry and defect engineering of TiO_2-based semiconductors for solar energy conversion,” *Chem. Soc. Rev.*, vol. 44, no. 23, pp. 8424–8442, 2015, doi: 10.1039/c4cs00469h.

[60] L. R. Grabstanowicz *et al.*, “Facile Oxidative Conversion of TiH_2 to High-Concentration Ti3+-Self-Doped Rutile TiO2 with Visible-Light Photoactivity,” *Inorg. Chem.*, vol. 52, no. 7, pp. 3884–3890, Apr. 2013, doi: 10.1021/ic3026182.

[61] X. Chen, L. Liu, P. Y. Yu, and S. S. Mao, “Increasing Solar Absorption for Photocatalysis with Black Hydrogenated Titanium Dioxide Nanocrystals,” *Science (80-.).*, vol. 331, no. 6018, pp. 746 LP – 750, Feb. 2011, doi: 10.1126/science.1200448.

[62] A. Sinhamahapatra, J.-P. Jeon, and J.-S. Yu, “A new approach to prepare highly active and stable black titania for visible light-assisted hydrogen production,” *Energy Environ. Sci.*, vol. 8, no. 12, pp. 3539–3544, 2015, doi: 10.1039/C5EE02443A.

[63] H. He, K. Yang, N. Wang, F. Luo, and H. Chen, “Hydrogenated TiO_2 film for enhancing photovoltaic properties of solar cells and self-sensitized effect,” *J. Appl. Phys.*, vol. 114, no. 21, p. 213505, Dec. 2013, doi: 10.1063/1.4832783.

[64] Z. Wang *et al.*, “H-Doped Black Titania with Very High Solar Absorption and Excellent Photocatalysis Enhanced by Localized Surface Plasmon Resonance,” *Adv. Funct. Mater.*, vol. 23, no. 43, pp. 5444–5450, 2013, doi: 10.1002/adfm.201300486.

[65] T. Nakajima, T. Nakamura, K. Shinoda, and T. Tsuchiya, “Rapid formation of black titania photoanodes: pulsed laser-induced oxygen release and enhanced solar water splitting efficiency,” *J. Mater. Chem. A*, vol. 2, no. 19, pp. 6762–6771, 2014, doi: 10.1039/C4TA00557K.

[66] Q. Kang, J. Cao, Y. Zhang, L. Liu, H. Xu, and J. Ye, “Reduced TiO_2 nanotube arrays for photoelectrochemical water splitting,” *J.*

Mater. Chem. A, vol. 1, no. 18, pp. 5766–5774, 2013, doi: 10.1039/C3TA10689F.

[67] Z. Wang *et al.*, “Visible-light photocatalytic, solar thermal and photoelectrochemical properties of aluminium-reduced black titania,” *Energy Environ. Sci.*, vol. 6, no. 10, pp. 3007–3014, 2013, doi: 10.1039/C3EE41817K.

[68] Z. Zhao *et al.*, “Reduced TiO_2 rutile nanorods with well-defined facets and their visible-light photocatalytic activity,” *Chem. Commun.*, vol. 50, no. 21, pp. 2755–2757, 2014, doi: 10.1039/C3CC49182J.

[69] V. R. Akshay, B. Arun, G. Mandal, A. Chanda, and M. Vasundhara, “Significant reduction in the optical band-gap and defect assisted magnetic response in Fe-doped anatase TiO_2 nanocrystals as dilute magnetic semiconductors,” *New J. Chem.*, vol. 43, no. 15, pp. 6048–6062, 2019, doi: 10.1039/C9NJ00275H.

[70] S. Mathew *et al.*, “Cu-Doped TiO_2: Visible Light Assisted Photocatalytic Antimicrobial Activity,” *Appl. Sci.*, vol. 8, p. 2067, Oct. 2018, doi: 10.3390/app8112067.

[71] L. M. Santos *et al.*, “Structural characterization of Ag-doped TiO_2 with enhanced photocatalytic activity,” *RSC Adv.*, vol. 5, no. 125, pp. 103752–103759, 2015, doi: 10.1039/C5RA22647C.

[72] M. Pelaez *et al.*, “A review on the visible light active titanium dioxide photocatalysts for environmental applications,” *Appl. Catal. B Environ.*, vol. 125, pp. 331–349, 2012, doi: 10.1016/j.apcatb.2012.05.036.

[73] A. K. Rumaiz, J. C. Woicik, E. Cockayne, H. Y. Lin, G. H. Jaffari, and S. I. Shah, “Oxygen vacancies in N doped anatase TiO_2: Experiment and first-principles calculations,” *Appl. Phys. Lett.*, vol. 95, no. 26, p. 262111, 2009, doi: 10.1063/1.3272272.

[74] Y. Yang, D. Ni, Y. Yao, Y. Zhong, Y. Ma, and J. Yao, “High photocatalytic activity of carbon doped TiO_2 prepared by fast combustion of organic capping ligands,” *RSC Adv.*, vol. 5, no. 113,

pp. 93635–93643, 2015, doi: 10.1039/C5RA19058D.

[75] C. Di Valentin, G. Pacchioni, A. Selloni, S. Livraghi, and E. Giamello, “Characterization of Paramagnetic Species in N-Doped TiO_2 Powders by EPR Spectroscopy and DFT Calculations,” *J. Phys. Chem. B*, vol. 109, no. 23, pp. 11414–11419, Jun. 2005, doi: 10.1021/jp051756t.

[76] K. Palanivelu, J.-S. Im, and Y.-S. Lee, “Carbon Doping of TiO_2 for Visible Light Photo Catalysis - A review,” *Carbon Lett.*, vol. 8, pp. 214–224, 2007, doi: 10.5714/CL.2007.8.3.214.

[77] L. Kong *et al.*, “Simple Ethanol Impregnation Treatment Can Enhance Photocatalytic Activity of TiO_2 Nanoparticles under Visible-Light Irradiation,” *ACS Appl. Mater. Interfaces*, vol. 7, no. 14, pp. 7752–7758, Apr. 2015, doi: 10.1021/acsami.5b00888.

[78] X. Zou, J. Liu, J. Su, F. Zuo, J. Chen, and P. Feng, “Facile Synthesis of Thermal and Photostable Titania with Paramagnetic Oxygen Vacancies for Visible-Light Photocatalysis,” *Chem. – A Eur. J.*, vol. 19, no. 8, pp. 2866–2873, Feb. 2013, doi: 10.1002/chem.201202833.

[79] F. Zuo, L. Wang, T. Wu, Z. Zhang, D. Borchardt, and P. Feng, “Self-Doped Ti^{3+} Enhanced Photocatalyst for Hydrogen Production under Visible Light,” *J. Am. Chem. Soc.*, vol. 132, no. 34, pp. 11856–11857, Sep. 2010, doi: 10.1021/ja103843d.

[80] S. G. Ullattil and P. Periyat, “A ‘one pot’ gel combustion strategy towards Ti^{3+} self-doped ‘black’ anatase TiO_{2-x} solar photocatalyst,” *J. Mater. Chem. A*, vol. 4, no. 16, pp. 5854–5858, 2016, doi: 10.1039/C6TA01993E.

[81] Q. Maqbool and A. Srivastava, “Benign Synthesis of Black Microspheres of Anatase TiO_2 with Paramagnetic Oxygen Vacancies through NH_3 Treatment,” *Chem. – A Eur. J.*, vol. 23, no. 56, pp. 13864–13868, 2017, doi: 10.1002/chem.201702343.

[82] P. Karthik, V. Vinesh, A. R. Mahammed Shaheer, and B. Neppolian, “Self-doping of Ti^{3+} in TiO_2 through incomplete

hydrolysis of titanium (IV) isopropoxide: An efficient visible light sonophotocatalyst for organic pollutants degradation," *Appl. Catal. A Gen.*, vol. 585, p. 117208, 2019, doi: 10.1016/j.apcata.2019.117208.

[83] G. Kieslich, S. Sun, and A. K. Cheetham, "An extended Tolerance Factor approach for organic-inorganic perovskites," *Chem. Sci.*, vol. 6, no. 6, pp. 3430–3433, 2015, doi: 10.1039/C5SC00961H.

[84] K. L. Svane *et al.*, "How Strong Is the Hydrogen Bond in Hybrid Perovskites?," *J. Phys. Chem. Lett.*, vol. 8, no. 24, pp. 6154–6159, Dec. 2017, doi: 10.1021/acs.jpclett.7b03106.

[85] P. R. Varadwaj, A. Varadwaj, H. M. Marques, and K. Yamashita, "Significance of hydrogen bonding and other noncovalent interactions in determining octahedral tilting in the $CH_3NH_3PbI_3$ hybrid organic-inorganic halide perovskite solar cell semiconductor," *Sci. Rep.*, vol. 9, no. 1, p. 50, 2019, doi: 10.1038/s41598-018-36218-1.

[86] A. Walsh, "Principles of Chemical Bonding and Band Gap Engineering in Hybrid Organic–Inorganic Halide Perovskites," *J. Phys. Chem. C*, vol. 119, no. 11, pp. 5755–5760, Mar. 2015, doi: 10.1021/jp512420b.

[87] V. M. Goldschmidt, "Die Gesetze der Krystallochemie," *Naturwissenschaften*, vol. 14, no. 21, pp. 477–485, 1926, doi: 10.1007/BF01507527.

[88] C. Li, X. Lu, W. Ding, L. Feng, Y. Gao, and Z. Guo, "Formability of ABX_3 (X = F, Cl, Br, I) halide perovskites," *Acta Crystallogr. Sect. B*, vol. 64, no. 6, pp. 702–707, Dec. 2008, doi: 10.1107/S0108768108032734.

[89] L. De Trizio *et al.*, "Sn Cation Valency Dependence in Cation Exchange Reactions Involving $Cu_{2-x}Se$ Nanocrystals," *J. Am. Chem. Soc.*, vol. 136, no. 46, pp. 16277–16284, Nov. 2014, doi: 10.1021/ja508161c.

[90] W. Travis, E. N. K. Glover, H. Bronstein, D. O. Scanlon, and R. G.

Palgrave, “On the application of the tolerance factor to inorganic and hybrid halide perovskites: a revised system,” *Chem. Sci.*, vol. 7, no. 7, pp. 4548–4556, 2016, doi: 10.1039/C5SC04845A.

[91] P. S. Whitfield *et al.*, “Structures, Phase Transitions and Tricritical Behavior of the Hybrid Perovskite Methyl Ammonium Lead Iodide,” *Sci. Rep.*, vol. 6, no. 1, p. 35685, 2016, doi: 10.1038/srep35685.

[92] Y. Takahashi, H. Hasegawa, Y. Takahashi, and T. Inabe, “Hall mobility in tin iodide perovskite $CH_3NH_3SnI_3$: Evidence for a doped semiconductor,” *J. Solid State Chem.*, vol. 205, pp. 39–43, 2013, doi: 10.1016/j.jssc.2013.07.008.

[93] X. Lü *et al.*, “Enhanced Structural Stability and Photo Responsiveness of $CH_3NH_3SnI_3$ Perovskite via Pressure-Induced Amorphization and Recrystallization,” *Adv. Mater.*, vol. 28, no. 39, pp. 8663–8668, Oct. 2016, doi: 10.1002/adma.201600771.

[94] T. Yokoyama *et al.*, “Overcoming Short-Circuit in Lead-Free $CH_3NH_3SnI_3$ Perovskite Solar Cells via Kinetically Controlled Gas–Solid Reaction Film Fabrication Process,” *J. Phys. Chem. Lett.*, vol. 7, no. 5, pp. 776–782, Mar. 2016, doi: 10.1021/acs.jpclett.6b00118.

[95] R. Prasanna *et al.*, “Band Gap Tuning via Lattice Contraction and Octahedral Tilting in Perovskite Materials for Photovoltaics,” *J. Am. Chem. Soc.*, vol. 139, no. 32, pp. 11117–11124, Aug. 2017, doi: 10.1021/jacs.7b04981.

[96] J.-H. Lee *et al.*, “Resolving the Physical Origin of Octahedral Tilting in Halide Perovskites,” *Chem. Mater.*, vol. 28, no. 12, pp. 4259–4266, Jun. 2016, doi: 10.1021/acs.chemmater.6b00968.

[97] Y. Dang *et al.*, “Formation of Hybrid Perovskite Tin Iodide Single Crystals by Top-Seeded Solution Growth,” *Angew. Chemie Int. Ed.*, vol. 55, no. 10, pp. 3447–3450, Mar. 2016, doi: 10.1002/anie.201511792.

[98] T. M. Koh *et al.*, “Formamidinium tin-based perovskite with low Eg

for photovoltaic applications," *J. Mater. Chem. A*, vol. 3, no. 29, pp. 14996–15000, 2015, doi: 10.1039/C5TA00190K.

[99] L. Lanzetta, J. M. Marin-Beloqui, I. Sanchez-Molina, D. Ding, and S. A. Haque, "Two-Dimensional Organic Tin Halide Perovskites with Tunable Visible Emission and Their Use in Light-Emitting Devices," *ACS Energy Lett.*, vol. 2, no. 7, pp. 1662–1668, Jul. 2017, doi: 10.1021/acsenergylett.7b00414.

[100] D. H. Cao *et al.*, "Thin Films and Solar Cells Based on Semiconducting Two-Dimensional Ruddlesden–Popper $(CH_3(CH_2)_3NH_3)_2(CH_3NH_3)_{n-1}Sn_nI_{3n+1}$ Perovskites," *ACS Energy Lett.*, vol. 2, no. 5, pp. 982–990, May 2017, doi: 10.1021/acsenergylett.7b00202.

[101] A. Pisanu, A. Speltini, P. Quadrelli, G. Drera, L. Sangaletti, and L. Malavasi, "Enhanced air-stability of Sn-based hybrid perovskites induced by dimethylammonium (DMA): synthesis, characterization, aging and hydrogen photogeneration of the $MA_{1-x}DMA_xSnBr_3$ system," *J. Mater. Chem. C*, vol. 7, no. 23, pp. 7020–7026, 2019, doi: 10.1039/C9TC01743G.

[102] W. Ke *et al.*, "Efficient Lead-Free Solar Cells Based on Hollow {en}$MASnI_3$ Perovskites," *J. Am. Chem. Soc.*, vol. 139, no. 41, pp. 14800–14806, Oct. 2017, doi: 10.1021/jacs.7b09018.

[103] W. Ke *et al.*, "Enhanced photovoltaic performance and stability with a new type of hollow 3D perovskite {en}$FASnI_3$," *Sci. Adv.*, vol. 3, no. 8, p. e1701293, Aug. 2017, doi: 10.1126/sciadv.1701293.

[104] L. Dimesso, C. Das, T. Mayer, and W. Jaegermann, "Investigation of earth-alkaline (EA = Mg, Ca, Sr) containing methylammonium tin iodide perovskite systems," *J. Mater. Sci.*, vol. 53, Jan. 2018, doi: 10.1007/s10853-017-1545-0.

[105] I. E. Castelli, J. M. García-Lastra, K. S. Thygesen, and K. W. Jacobsen, "Bandgap calculations and trends of organometal halide perovskites," *APL Mater.*, vol. 2, no. 8, p. 81514, Aug. 2014,

doi: 10.1063/1.4893495.

[106] S. Kumar, M. Z. Ansari, and N. Khare, “Transparent $CH_3NH_3SnCl_3$/Al-ZnO p-n heterojunction diode,” *AIP Conf. Proc.*, vol. 1731, no. 1, p. 120025, May 2016, doi: 10.1063/1.4948097.

[107] N. Gopinathan, S. S. Basha, I. B. S. Banu, M. H. Mamat, and M. M. S. Sirajudeen, “Solvents driven structural, morphological, optical and dielectric properties of lead free perovskite $CH_3NH_3SnCl_3$ for optoelectronic applications: experimental and DFT study,” *Mater. Res. Express*, vol. 6, no. 12, p. 125921, 2020, doi: 10.1088/2053-1591/ab6a47.

[108] Z. Shi and A. H. Jayatissa, “Perovskites-Based Solar Cells: A Review of Recent Progress, Materials and Processing Methods,” *Materials* , vol. 11, no. 5. 2018, doi: 10.3390/ma11050729.

[109] Z. Song, S. C. Watthage, A. B. Phillips, and M. J. Heben, “Pathways toward high-performance perovskite solar cells: review of recent advances in organo-metal halide perovskites for photovoltaic applications,” *J. Photonics Energy*, vol. 6, no. 2, pp. 1–23, 2016, doi: 10.1117/1.JPE.6.022001.

[110] M.-C. Jung, S. R. Raga, and Y. Qi, “Properties and solar cell applications of Pb-free perovskite films formed by vapor deposition,” *RSC Adv.*, vol. 6, no. 4, pp. 2819–2825, 2016, doi: 10.1039/C5RA21291J.

[111] W. Ke *et al.*, “Dopant-Free Tetrakis-Triphenylamine Hole Transporting Material for Efficient Tin-Based Perovskite Solar Cells,” *J. Am. Chem. Soc.*, vol. 140, no. 1, pp. 388–393, Jan. 2018, doi: 10.1021/jacs.7b10898.

[112] L. Dongxue and Y. Liu, “Recent progress of dopant-free organic hole-transporting materials in perovskite solar cells,” *J. Semicond.*, vol. 38, no. 1, p. 11005, Jan. 2017, doi: 10.1088/1674-4926/38/1/011005.

[113] X. Yin, Y. Guo, H. Xie, W. Que, and L. B. Kong, “Nickel Oxide as Efficient Hole Transport Materials for Perovskite Solar Cells,” *Sol.*

RRL, vol. 3, no. 5, p. 1900001, 2019, doi: 10.1002/solr.201900001.

[114] L. Ma, F. Hao, C. C. Stoumpos, B. T. Phelan, M. R. Wasielewski, and M. G. Kanatzidis, “Carrier Diffusion Lengths of over 500 nm in Lead-Free Perovskite $CH_3NH_3SnI_3$ Films,” *J. Am. Chem. Soc.*, vol. 138, no. 44, pp. 14750–14755, Nov. 2016, doi: 10.1021/jacs.6b09257.

[115] Z. Yang *et al.*, “SnO_2-C60 Pyrrolidine Tris-Acid (CPTA) as the Electron Transport Layer for Highly Efficient and Stable Planar Sn-Based Perovskite Solar Cells,” *Adv. Funct. Mater.*, vol. 29, no. 42, p. 1903621, Oct. 2019, doi: 10.1002/adfm.201903621.

[116] D. Huang *et al.*, “Perovskite solar cells with a DMSO-treated PEDOT:PSS hole transport layer exhibit higher photovoltaic performance and enhanced durability,” *Nanoscale*, vol. 9, no. 12, pp. 4236–4243, 2017, doi: 10.1039/C6NR08375G.

[117] A. Al Mamun, T. T. Ava, K. Zhang, H. Baumgart, and G. Namkoong, “New PCBM/carbon based electron transport layer for perovskite solar cells,” *Phys. Chem. Chem. Phys.*, vol. 19, no. 27, pp. 17960–17966, 2017, doi: 10.1039/C7CP02523H.

[118] M. Baranowski and P. Plochocka, “Excitons in Metal-Halide Perovskites,” *Adv. Energy Mater.*, vol. 10, no. 6, p. 1903659, 2020, doi: 10.1002/aenm.201903659.

[119] A. Miyata *et al.*, “Direct measurement of the exciton binding energy and effective masses for charge carriers in organic-inorganic tri-halide perovskites,” *Nat Phys*, vol. 11, no. 7, pp. 582–587, Jul. 2015, doi: 10.1038/nphys3357.

[120] Z. Yang *et al.*, “Unraveling the Exciton Binding Energy and the Dielectric Constant in Single-Crystal Methylammonium Lead Triiodide Perovskite,” *J. Phys. Chem. Lett.*, vol. 8, no. 8, pp. 1851–1855, Apr. 2017, doi: 10.1021/acs.jpclett.7b00524.

[121] K. Galkowski *et al.*, “Excitonic Properties of Low-Band-Gap Lead–Tin Halide Perovskites,” *ACS Energy Lett.*, vol. 4, no. 3, pp. 615–

621, Mar. 2019, doi: 10.1021/acsenergylett.8b02243.

[122] ZSW, “Perovskite Solar cells.” https://www.zsw-bw.de/forschung/photovoltaik/themen/perowskitsolarzellen.html (accessed Nov. 17, 2019).

[123] Z. H. Bakr, Q. Wali, A. Fakharuddin, L. Schmidt-Mende, T. M. Brown, and R. Jose, “Advances in hole transport materials engineering for stable and efficient perovskite solar cells,” *Nano Energy*, vol. 34, pp. 271–305, 2017, doi: 10.1016/j.nanoen.2017.02.025.

[124] V. Manjunath, R. Krishna, S. Maniarasu, E. Ramasamy, S. Shanmugasundaram, and G. Veerappan, “Chapter 4 - Perovskite Solar Cell Architectures,” S. Thomas and A. B. T.-P. P. Thankappan, Eds. Academic Press, 2018, pp. 89–121.

[125] J. S. Manser, J. A. Christians, and P. V Kamat, “Intriguing Optoelectronic Properties of Metal Halide Perovskites,” *Chem. Rev.*, vol. 116, no. 21, pp. 12956–13008, Nov. 2016, doi: 10.1021/acs.chemrev.6b00136.

[126] W. Shockley, “The Theory of p-n Junctions in Semiconductors and p-n Junction Transistors,” *Bell Syst. Tech. J.*, vol. 28, no. 3, pp. 435–489, Jul. 1949, doi: 10.1002/j.1538-7305.1949.tb03645.x.

[127] O. Breitenstein, “Understanding the current-voltage characteristics of industrial crystalline silicon solar cells by considering inhomogeneous current distributions,” *Opto-Electronics Rev.*, vol. 21, no. 3, pp. 259–282, 2013, doi: 10.2478/s11772-013-0095-5.

[128] P. S. Priambodo, N. R. Poespawati, and D. Hartanto, “Solar Cells,” in *Silicon Wafer-Based Technologies*, A. Kosyachenko, Leonid, Ed. Rijeka: IntechOpen, 2011, pp. 1–28.

[129] N. Shintaku, M. Hiramoto, and S. Izawa, “Effect of trap-assisted recombination on open-circuit voltage loss in phthalocyanine/fullerene solar cells,” *Org. Electron.*, vol. 55, pp. 69–74, 2018, doi: 10.1016/j.orgel.2018.01.016.

[130] C. Uhrich *et al.*, “Origin of open circuit voltage in planar and bulk heterojunction organic thin-film photovoltaics depending on doped transport layers,” *J. Appl. Phys.*, vol. 104, no. 4, p. 43107, Aug. 2008, doi: 10.1063/1.2973199.

[131] J. H. Heo and S. H. Im, “Highly reproducible, efficient hysteresis-less $CH_3NH_3PbI_{3-x}Cl_x$ planar hybrid solar cells without requiring heat-treatment,” *Nanoscale*, vol. 8, 2015, doi: 10.1039/C5NR08458J.

[132] F. Hao *et al.*, “Solvent-Mediated Crystallization of $CH_3NH_3SnI_3$ Films for Heterojunction Depleted Perovskite Solar Cells,” *J. Am. Chem. Soc.*, vol. 137, no. 35, pp. 11445–11452, Sep. 2015, doi: 10.1021/jacs.5b06658.

[133] X. Liu, K. Yan, D. Tan, X. Liang, H. Zhang, and W. Huang, “Solvent Engineering Improves Efficiency of Lead-Free Tin-Based Hybrid Perovskite Solar Cells beyond 9%,” *ACS Energy Lett.*, vol. 3, no. 11, pp. 2701–2707, Nov. 2018, doi: 10.1021/acsenergylett.8b01588.

[134] C. C. Vidyasagar, B. M. Muñoz Flores, and V. M. Jiménez Pérez, “Recent Advances in Synthesis and Properties of Hybrid Halide Perovskites for Photovoltaics,” *Nano-Micro Lett.*, vol. 10, no. 4, p. 68, 2018, doi: 10.1007/s40820-018-0221-5.

[135] M. Xiao *et al.*, “A Fast Deposition-Crystallization Procedure for Highly Efficient Lead Iodide Perovskite Thin-Film Solar Cells,” *Angew. Chemie*, vol. 126, no. 37, pp. 10056–10061, 2014, doi: 10.1002/ange.201405334.

[136] M. Xiao *et al.*, “Selection of an anti-solvent for efficient and stable cesium-containing triple cation planar perovskite solar cells,” *Nanoscale*, vol. 10, no. 25, pp. 12141–12148, 2018, doi: 10.1039/C8NR03580F.

[137] T. Fujihara, S. Terakawa, T. Matsushima, C. Qin, M. Yahiro, and C. Adachi, “Fabrication of high coverage $MASnI_3$ perovskite films for stable, planar heterojunction solar cells,” *J. Mater. Chem. C*,

vol. 5, no. 5, pp. 1121–1127, 2017, doi: 10.1039/C6TC05069G.

[138] J. Liu *et al.*, “Lead-Free Solar Cells based on Tin Halide Perovskite Films with High Coverage and Improved Aggregation,” *Angew. Chemie Int. Ed.*, vol. 57, no. 40, pp. 13221–13225, Oct. 2018, doi: 10.1002/anie.201808385.

[139] X.-L. Li, L.-L. Gao, Q.-Q. Chu, Y. Li, B. Ding, and G.-J. Yang, “Green Solution-Processed Tin-Based Perovskite Films for Lead-Free Planar Photovoltaic Devices,” *ACS Appl. Mater. Interfaces*, vol. 11, no. 3, pp. 3053–3060, Jan. 2019, doi: 10.1021/acsami.8b19143.

[140] J. Burschka *et al.*, “Sequential deposition as a route to high-performance perovskite-sensitized solar cells,” *Nature*, vol. 499, no. 7458, pp. 316–319, Jul. 2013, doi: 10.1038/nature12340.

[141] T. H. Chowdhury, M. E. Kayesh, J.-J. Lee, Y. Matsushita, S. Kazaoui, and A. Islam, “Post-Deposition Vapor Annealing Enables Fabrication of 1 cm^2 Lead-Free Perovskite Solar Cells,” *Sol. RRL*, vol. 3, no. 12, p. 1900245, 2019, doi: 10.1002/solr.201900245.

[142] F. Gao *et al.*, “Enhanced performance of tin halide perovskite solar cell by addition of lead thiocyanate,” *RSC Adv.*, vol. 8, no. 25, pp. 14025–14030, 2018, doi: 10.1039/C8RA00809D.

[143] C. Mortan, T. Hellmann, O. Clemens, T. Mayer, and W. Jaegermann, “Preparation of Methylammonium Tin Iodide ($CH_3NH_3SnI_3$) Perovskite Thin Films via Flash Evaporation,” *Phys. status solidi*, vol. 216, no. 18, p. 1900209, Sep. 2019, doi: 10.1002/pssa.201900209.

[144] T. Arend, M. Tönnies, P. Reisbeck, C. Rieckmann, and R. Kersting, “Physical vapor deposition of methylammonium tin iodide thin films,” *Phys. status solidi*, vol. 214, Mar. 2017, doi: 10.1002/pssa.201600796.

[145] D. Weber, “$CH_3NH_3SnBr_xI_{3-x}$ (x = 0-3), ein Sn(II)-System mit kubischer Perowskitstruktur / $CH_3NH_3SnBr_xI_{3-x}$(x = 0-3), a Sn(II)-System with Cubic Perovskite Structure,” *Zeitschrift für*

Naturforschung B, vol. 33. p. 862, 1978, doi: 10.1515/znb-1978-0809.

[146] K. Yamada, T. Matsui, T. Tsuritani, T. Okuda, and S. Ichiba, “127I-NQR, 119 Sn Mössbauer Effect, and Electrical Conductivity of $MSnI_3$ (M = K, NH_4, Rb, Cs, and CH_3NH_3),” *Zeitschrift für Naturforsch. A*, vol. 45, Apr. 1990, doi: 10.1515/zna-1990-3-416.

[147] D. B. Mitzi, C. A. Feild, W. T. A. Harrison, and A. M. Guloy, “Conducting tin halides with a layered organic-based perovskite structure,” *Nature*, vol. 369, no. 6480, pp. 467–469, Jun. 1994, doi: 10.1038/369467a0.

[148] D. B. Mitzi, C. A. Feild, Z. Schlesinger, and R. B. Laibowitz, “Transport, Optical, and Magnetic Properties of the Conducting Halide Perovskite $CH_3NH_3SnI_3$,” *J. Solid State Chem.*, vol. 114, no. 1, pp. 159–163, 1995, doi: 10.1006/jssc.1995.1023.

[149] Y. Ogomi *et al.*, “$CH_3NH_3Sn_xPb_{1-x}I_3$ Perovskite Solar Cells Covering up to 1060 nm,” *J. Phys. Chem. Lett.*, vol. 5, no. 6, pp. 1004–1011, Mar. 2014, doi: 10.1021/jz5002117.

[150] T.-B. Song, T. Yokoyama, S. Aramaki, and M. G. Kanatzidis, “Performance Enhancement of Lead-Free Tin-Based Perovskite Solar Cells with Reducing Atmosphere-Assisted Dispersible Additive,” *ACS Energy Lett.*, vol. 2, no. 4, pp. 897–903, Apr. 2017, doi: 10.1021/acsenergylett.7b00171.

[151] K. P. Marshall, M. Walker, R. I. Walton, and R. A. Hatton, “Enhanced stability and efficiency in hole-transport-layer-free $CsSnI_3$ perovskite photovoltaics,” *Nat. Energy*, vol. 1, no. 12, p. 16178, 2016, doi: 10.1038/nenergy.2016.178.

[152] M. H. Kumar *et al.*, “Lead-free halide perovskite solar cells with high photocurrents realized through vacancy modulation.,” *Adv. Mater.*, vol. 26, no. 41, pp. 7122–7, Nov. 2014, doi: 10.1002/adma.201401991.

[153] T. Nakamura *et al.*, “Sn(IV)-free tin perovskite films realized by in situ Sn(0) nanoparticle treatment of the precursor solution,” *Nat.*

Commun., vol. 11, no. 1, p. 3008, 2020, doi: 10.1038/s41467-020-16726-3.

[154] M. Xiao *et al.*, “Tin-Based Perovskite with Improved Coverage and Crystallinity through Tin-Fluoride-Assisted Heterogeneous Nucleation,” *Adv. Opt. Mater.*, vol. 6, no. 1, p. 1700615, Jan. 2018, doi: 10.1002/adom.201700615.

[155] H. Hoshi, N. Shigeeda, and T. Dai, “Improved oxidation stability of tin iodide cubic perovskite treated by 5-ammonium valeric acid iodide,” *Mater. Lett.*, vol. 183, pp. 391–393, Nov. 2016, doi: 10.1016/j.matlet.2016.07.048.

[156] F. Gu *et al.*, “Improving Performance of Lead-Free Formamidinium Tin Triiodide Perovskite Solar Cells by Tin Source Purification,” *Sol. RRL*, vol. 2, no. 10, p. 1800136, 2018, doi: 10.1002/solr.201800136.

[157] X. Xu *et al.*, “Ascorbic acid as an effective antioxidant additive to enhance the efficiency and stability of Pb/Sn-based binary perovskite solar cells,” *Nano Energy*, vol. 34, pp. 392–398, 2017, doi: 10.1016/j.nanoen.2017.02.040.

[158] T.-B. Song *et al.*, “Importance of Reducing Vapor Atmosphere in the Fabrication of Tin-Based Perovskite Solar Cells,” *J. Am. Chem. Soc.*, vol. 139, no. 2, pp. 836–842, Jan. 2017, doi: 10.1021/jacs.6b10734.

[159] S. Tsarev *et al.*, “Hydrazinium-assisted stabilisation of methylammonium tin iodide for lead-free perovskite solar cells,” *J. Mater. Chem. A*, vol. 6, no. 43, pp. 21389–21395, 2018, doi: 10.1039/C8TA07699E.

[160] F. Li *et al.*, “A Cation-Exchange Approach for the Fabrication of Efficient Methylammonium Tin Iodide Perovskite Solar Cells,” *Angew. Chemie Int. Ed.*, vol. 58, no. 20, pp. 6688–6692, May 2019, doi: 10.1002/anie.201902418.

[161] M. E. Kayesh *et al.*, “Enhanced Photovoltaic Performance of $FASnI_3$-Based Perovskite Solar Cells with Hydrazinium Chloride

Coadditive," *ACS Energy Lett.*, vol. 3, no. 7, pp. 1584–1589, Jul. 2018, doi: 10.1021/acsenergylett.8b00645.

[162] F. Li *et al.*, "Trihydrazine Dihydriodide-Assisted Fabrication of Efficient Formamidinium Tin Iodide Perovskite Solar Cells," *Sol. RRL*, vol. 3, no. 9, p. 1900285, Sep. 2019, doi: 10.1002/solr.201900285.

[163] Y. Yu *et al.*, "Thermally evaporated methylammonium tin triiodide thin films for lead-free perovskite solar cell fabrication," *RSC Adv.*, vol. 6, no. 93, pp. 90248–90254, 2016, doi: 10.1039/C6RA19476A.

[164] Z. Zhu, C.-C. Chueh, N. Li, C. Mao, and A. K.-Y. Jen, "Realizing Efficient Lead-Free Formamidinium Tin Triiodide Perovskite Solar Cells via a Sequential Deposition Route," *Adv. Mater.*, vol. 30, no. 6, p. 1703800, 2018, doi: 10.1002/adma.201703800.

[165] M. Weiss, J. Horn, C. Richter, and D. Schlettwein, "Preparation and characterization of methylammonium tin iodide layers as photovoltaic absorbers," *Phys. status solidi*, vol. 213, no. 4, pp. 975–981, 2016, doi: 10.1002/pssa.201532594.

[166] F. Zuo, S. T. Williams, P.-W. Liang, C.-C. Chueh, C.-Y. Liao, and A. K.-Y. Jen, "Binary-Metal Perovskites Toward High-Performance Planar-Heterojunction Hybrid Solar Cells," *Adv. Mater.*, vol. 26, no. 37, pp. 6454–6460, 2014, doi: 10.1002/adma.201401641.

[167] G. E. Eperon *et al.*, "Perovskite-perovskite tandem photovoltaics with optimized band gaps," *Science (80-.).*, vol. 354, no. 6314, pp. 861–865, 2016, doi: 10.1126/science.aaf9717.

[168] X. Qiu *et al.*, "From unstable $CsSnI_3$ to air-stable Cs_2SnI_6: A lead-free perovskite solar cell light absorber with bandgap of 1.48eV and high absorption coefficient," *Sol. Energy Mater. Sol. Cells*, vol. 159, pp. 227–234, 2017, doi: 10.1016/j.solmat.2016.09.022.

[169] F. Funabiki, Y. Toda, and H. Hosono, "Optical and Electrical Properties of Perovskite Variant $(CH_3NH_3)_2SnI_6$," *J. Phys. Chem. C*, vol. 122, no. 20, pp. 10749–10754, May 2018, doi:

10.1021/acs.jpcc.8b01820.

[170] Z. Huanping *et al.*, “Interface engineering of highly efficient perovskite solar cells,” *Science (80-.).*, vol. 345, no. 6196, pp. 542–546, Aug. 2014, doi: 10.1126/science.1254050.

[171] K. K. Bass, R. E. McAnally, S. Zhou, P. I. Djurovich, M. E. Thompson, and B. C. Melot, “Influence of moisture on the preparation, crystal structure, and photophysical properties of organohalide perovskites,” *Chem. Commun.*, vol. 50, no. 99, pp. 15819–15822, 2014, doi: 10.1039/C4CC05231E.

[172] A. Dubey *et al.*, “Room temperature, air crystallized perovskite film for high performance solar cells,” *J. Mater. Chem. A*, vol. 4, no. 26, pp. 10231–10240, 2016, doi: 10.1039/C6TA02918C.

[173] J. Zhao *et al.*, “Investigation of the Hydrolysis of Perovskite Organometallic Halide $CH_3NH_3PbI_3$ in Humidity Environment,” *Sci. Rep.*, vol. 6, p. 21976, Feb. 2016, doi: 10.1038/srep21976.

[174] G. H. Imler *et al.*, “Solid state transformation of the crystalline monohydrate $(CH_3NH_3)PbI_3(H_2O)$ to the $(CH_3NH_3)PbI_3$ perovskite,” *Chem. Commun.*, vol. 51, no. 56, pp. 11290–11292, 2015, doi: 10.1039/C5CC03741G.

[175] X. Dong *et al.*, “Improvement of the humidity stability of organic-inorganic perovskite solar cells using ultrathin Al_2O_3 layers prepared by atomic layer deposition,” *J. Mater. Chem. A*, vol. 3, no. 10, pp. 5360–5367, 2015, doi: 10.1039/C4TA06128D.

[176] D. Li *et al.*, “Humidity-Induced Grain Boundaries in $MAPbI_3$ Perovskite Films,” *J. Phys. Chem. C*, vol. 120, no. 12, pp. 6363–6368, Mar. 2016, doi: 10.1021/acs.jpcc.6b00335.

[177] J. Yang, B. D. Siempelkamp, D. Liu, and T. L. Kelly, “Investigation of $CH_3NH_3PbI_3$ Degradation Rates and Mechanisms in Controlled Humidity Environments Using in Situ Techniques,” *ACS Nano*, vol. 9, no. 2, pp. 1955–1963, Feb. 2015, doi: 10.1021/nn506864k.

[178] A. M. A. Leguy *et al.*, “Reversible Hydration of $CH_3NH_3PbI_3$in Films, Single Crystals, and Solar Cells,” *Chem. Mater.*, vol. 27, no.

9, pp. 3397–3407, May 2015, doi: 10.1021/acs.chemmater.5b00660.

[179] J. M. Frost, K. T. Butler, F. Brivio, C. H. Hendon, M. van Schilfgaarde, and A. Walsh, “Atomistic Origins of High-Performance in Hybrid Halide Perovskite Solar Cells,” *Nano Lett.*, vol. 14, no. 5, pp. 2584–2590, May 2014, doi: 10.1021/nl500390f.

[180] S. Ito, S. Tanaka, K. Manabe, and H. Nishino, “Effects of Surface Blocking Layer of Sb_2S_3 on Nanocrystalline TiO_2 for $CH_3NH_3PbI_3$ Perovskite Solar Cells,” *J. Phys. Chem. C*, vol. 118, no. 30, pp. 16995–17000, Jul. 2014, doi: 10.1021/jp500449z.

[181] D. Kim, J. Hong, Y. Park, and K. Kim, “The origin of oxygen vacancy induced ferromagnetism in undoped TiO_2,” *J. Phys. Condens. Matter*, vol. 21, p. 195405, 2009, doi: 10.1088/0953-8984/21/19/195405.

[182] S. Park, B. Magyari-Kope, and Y. Nishi, “First-principles study of resistance switching in rutile TiO_2 with oxygen vacancy,” in *2008 9th Annual Non-Volatile Memory Technology Symposium (NVMTS)*, 2008, pp. 1–5, doi: 10.1109/NVMT.2008.4731193.

[183] B. Yang, G. Chen, H. Tian, and L. Wen, “Improvement of the Photoelectrochemical Performance of TiO_2 Nanorod Array by PEDOT and Oxygen Vacancy Co-Modification,” *Catalysts*, vol. 9, no. 5, 2019, doi: 10.3390/catal9050407.

[184] A. Sarkar and G. G. Khan, “The formation and detection techniques of oxygen vacancies in titanium oxide-based nanostructures,” *Nanoscale*, vol. 11, no. 8, pp. 3414–3444, 2019, doi: 10.1039/C8NR09666J.

[185] J. Yu, “Preparation of Blue TiO_2 for Visible-Light-Driven Photocatalysis,” C. T. K. Nguyen, Ed. Rijeka: IntechOpen, 2018, p. Ch. 12.

[186] M. Wajid Shah *et al.*, “Facile Synthesis of Defective TiO_{2-x} Nanocrystals with High Surface Area and Tailoring Bandgap for Visible-light Photocatalysis,” *Sci. Rep.*, vol. 5, no. 1, p. 15804,

2015, doi: 10.1038/srep15804.

[187] S. Hoang, S. P. Berglund, N. T. Hahn, A. J. Bard, and C. B. Mullins, “Enhancing Visible Light Photo-oxidation of Water with TiO_2 Nanowire Arrays via Cotreatment with H_2 and NH_3: Synergistic Effects between Ti^{3+} and N,” *J. Am. Chem. Soc.*, vol. 134, no. 8, pp. 3659–3662, Feb. 2012, doi: 10.1021/ja211369s.

[188] X. Pan, M.-Q. Yang, X. Fu, N. Zhang, and Y.-J. Xu, “Defective TiO_2 with oxygen vacancies: synthesis, properties and photocatalytic applications,” *Nanoscale*, vol. 5, no. 9, pp. 3601–3614, 2013, doi: 10.1039/C3NR00476G.

[189] S. G. Ullattil, S. B. Narendranath, S. C. Pillai, and P. Periyat, “Black TiO_2 Nanomaterials: A Review of Recent Advances,” *Chem. Eng. J.*, vol. 343, pp. 708–736, Jul. 2018, doi: 10.1016/J.CEJ.2018.01.069.

[190] M. Qiu *et al.*, “Synthesis of Ti^{3+} self-doped TiO_2 nanocrystals based on Le Chatelier’s principle and their application in solar light photocatalysis,” *RSC Adv.*, vol. 6, no. 78, pp. 74376–74383, 2016, doi: 10.1039/C6RA12674J.

[191] R. Nawaz, C. F. Kait, H. Y. Chia, M. H. Isa, and L. W. Huei, “Glycerol-Mediated Facile Synthesis of Colored Titania Nanoparticles for Visible Light Photodegradation of Phenolic Compounds,” *Nanomaterials*, vol. 9, no. 11, 2019, doi: 10.3390/nano9111586.

[192] J. Wang *et al.*, “Origin of Photocatalytic Activity of Nitrogen-Doped TiO_2 Nanobelts,” *J. Am. Chem. Soc.*, vol. 131, no. 34, pp. 12290–12297, Sep. 2009, doi: 10.1021/ja903781h.

[193] I. Nakamura, N. Negishi, S. Kutsuna, T. Ihara, S. Sugihara, and K. Takeuchi, “Role of Oxygen Vacancy in the Plasma-Treated TiO_2 Photocatalyst With Visible Light Activity for NO Removal,” *J. Mol. Catal. A Chem.*, vol. 161, pp. 205–212, Nov. 2000, doi: 10.1016/S1381-1169(00)00362-9.

[194] X. Pan, N. Zhang, X. Fu, and Y.-J. Xu, “Selective oxidation of

benzyl alcohol over TiO_2 nanosheets with exposed {001} facets: Catalyst deactivation and regeneration," *Appl. Catal. A Gen.*, vol. 453, pp. 181–187, 2013, doi: 10.1016/j.apcata.2012.12.023.

[195] Z.-T. Wang, N. A. Deskins, M. A. Henderson, and I. Lyubinetsky, "Inhibitive Influence of Oxygen Vacancies for Photoactivity on TiO_2 (110)," *Phys. Rev. Lett.*, vol. 109, no. 26, p. 266103, Dec. 2012, doi: 10.1103/PhysRevLett.109.266103.

[196] T. Xia, Y. Zhang, J. Murowchick, and X. Chen, "Vacuum-treated titanium dioxide nanocrystals: Optical properties, surface disorder, oxygen vacancy, and photocatalytic activities," *Catal. Today*, vol. 225, pp. 2–9, 2014, doi: 10.1016/j.cattod.2013.08.026.

[197] W. Yu, F. Chen, Y. Wang, and L. Zhao, "Rapid evaluation of oxygen vacancies-enhanced photogeneration of the superoxide radical in nano-TiO_2 suspensions," *RSC Adv.*, vol. 10, no. 49, pp. 29082–29089, 2020, doi: 10.1039/D0RA06299E.

[198] G. Wang *et al.*, "Hydrogen-Treated TiO_2 Nanowire Arrays for Photoelectrochemical Water Splitting," *Nano Lett.*, vol. 11, no. 7, pp. 3026–3033, Jul. 2011, doi: 10.1021/nl201766h.

[199] M. Liu, X. Qiu, M. Miyauchi, and K. Hashimoto, "Cu(II) Oxide Amorphous Nanoclusters Grafted Ti^{3+} Self-Doped TiO_2: An Efficient Visible Light Photocatalyst," *Chem. Mater.*, vol. 23, no. 23, pp. 5282–5286, Dec. 2011, doi: 10.1021/cm203025b.

[200] National Center for Biotechnology Information, "PubChem Compound Summary for CID 16231, Amiloride," 2019. https://pubchem.ncbi.nlm.nih.gov/compound/Amiloride (accessed Aug. 10, 2019).

[201] P. Calza, C. Massolino, G. Monaco, C. Medana, and C. Baiocchi, "Study of the photolytic and photocatalytic transformation of amiloride in water," *J. Pharm. Biomed. Anal.*, vol. 48, no. 2, pp. 315–320, Sep. 2008, doi: 10.1016/J.JPBA.2008.01.014.

[202] D. J. Benos, "Amiloride: a molecular probe of sodium transport in tissues and cells," *Am. J. Physiol. Physiol.*, vol. 242, no. 3, pp.

C131–C145, 1982, doi: 10.1152/ajpcell.1982.242.3.C131.

[203] S. Kaihara, S. Matsumura, A. G. Mikos, and J. P. Fisher, “Synthesis of poly(L-lactide) and polyglycolide by ring-opening polymerization,” *Nat. Protoc.*, vol. 2, no. 11, pp. 2767–2771, 2007, doi: 10.1038/nprot.2007.391.

[204] M. Szycher, *Szycher’s Handbook of Polyurethanes, First Edition*. Taylor & Francis, 1999.

[205] National Center for Biotechnology Information, “PubChem Compound Summary for CID 9318, Stannous octoate,” *PubChem*. https://pubchem.ncbi.nlm.nih.gov/compound/Stannous-octoate#section=2D-Structure (accessed Feb. 06, 2019).

[206] M. J. García-Campo, T. Boronat, L. Quiles-Carrillo, R. Balart, and N. Montanes, “Manufacturing and Characterization of Toughened Poly(lactic acid) (PLA) Formulations by Ternary Blends with Biopolyesters,” *Polymers* , vol. 10, no. 1. 2018, doi: 10.3390/polym10010003.

[207] M. EL-Henawey, R. Gebhardt, M. El-Tonsy, and S. Chaudhary, “Organic solvent vapor treatment of the lead iodide layer in the two-step sequential deposition of $CH_3NH_3PbI_3$-based perovskite solar cells,” *J. Mater. Chem. A*, vol. 4, Dec. 2015, doi: 10.1039/C5TA08656F.

[208] P. Da, M. Cha, L. Sun, Y. Wu, Z.-S. Wang, and G. Zheng, “High-Performance Perovskite Photoanode Enabled by Ni Passivation and Catalysis,” *Nano Lett.*, vol. 15, Apr. 2015, doi: 10.1021/acs.nanolett.5b00788.

[209] M. I. Ahmed, Z. Hussain, A. Khalid, H. M. N. Amin, and A. Habib, “Absorption enhancement in $CH_3NH_3PbI_3$ solar cell using a TiO_2/MoS_2 nanocomposite electron selective contact,” *Mater. Res. Express*, vol. 3, no. 4, p. 45022, 2016, doi: 10.1088/2053-1591/3/4/045022.

[210] E. H. Anaraki *et al.*, “Highly efficient and stable planar perovskite solar cells by solution-processed tin oxide,” *Energy Environ. Sci.*,

vol. 9, no. 10, pp. 3128–3134, 2016, doi: 10.1039/C6EE02390H.

[211] M. Saliba *et al.*, “How to Make over 20% Efficient Perovskite Solar Cells in Regular (n–i–p) and Inverted (p–i–n) Architectures,” *Chem. Mater.*, vol. 30, no. 13, pp. 4193–4201, Jul. 2018, doi: 10.1021/acs.chemmater.8b00136.

[212] A. C. Larson and R. B. Von Dreele, “General Structure Analysis System (GSAS),” 2004.

[213] Toby B. H., “EXPGUI, a graphical user interface for GSAS,” *J. Appl. Crystallogr.*, vol. 34, pp. 210–213, 2001.

[214] L. Dimesso, C. Fasel, K. Lakus-Wollny, T. Mayer, and W. Jaegermann, “Thermal stability of lead-free $CH_3NH_3Sn_xI_3$ systems ($0.9 \leq x \leq 1.1$) for photovoltaics,” *Mater. Sci. Semicond. Process.*, vol. 68, pp. 152–158, Sep. 2017, doi: 10.1016/j.mssp.2017.06.012.

[215] S.-Y. Kim, H.-J. Jo, S.-J. Sung, K.-P. Kim, Y.-W. Heo, and D.-H. Kim, “Preferential (100)-oriented $CH_3NH_3PbI_3$ perovskite film formation by flash drying and elucidation of formation mechanism,” *RSC Adv.*, vol. 6, no. 97, pp. 94502–94509, 2016, doi: 10.1039/C6RA21423A.

[216] D. Bartesaghi, A. Ray, J. Jiang, R. K. M. Bouwer, S. Tao, and T. J. Savenije, “Partially replacing Pb^{2+} by Mn^{2+} in hybrid metal halide perovskites: Structural and electronic properties,” *APL Mater.*, vol. 6, no. 12, p. 121106, Dec. 2018, doi: 10.1063/1.5060953.

[217] M. I. Saidaminov, A. L. Abdelhady, G. Maculan, and O. M. Bakr, “Retrograde solubility of formamidinium and methylammonium lead halide perovskites enabling rapid single crystal growth,” *Chem. Commun.*, vol. 51, no. 100, pp. 17658–17661, 2015, doi: 10.1039/C5CC06916E.

[218] D. Bai *et al.*, “Interstitial Mn^{2+}-Driven High-Aspect-Ratio Grain Growth for Low-Trap-Density Microcrystalline Films for Record Efficiency $CsPbI_2Br$ Solar Cells,” *ACS Energy Lett.*, vol. 3, no. 4, pp. 970–978, Apr. 2018, doi: 10.1021/acsenergylett.8b00270.

[219] W. Liu *et al.*, “Efficient perovskite solar cells fabricated by manganese cations incorporated in hybrid perovskites,” *J. Mater. Chem. C*, vol. 7, no. 38, pp. 11943–11952, 2019, doi: 10.1039/C9TC03375K.

[220] M. Du, L. Cui, and F. Liu, “A New Reversible Phase Transformation of Intermetallic Ti_3Sn,” *Materials (Basel).*, vol. 12(15), p. 2484, Aug. 2019, doi: 10.3390/ma12152484.

[221] T. M. Brenner *et al.*, “Conversion of Single Crystalline PbI_2 to $CH_3NH_3PbI_3$: Structural Relations and Transformation Dynamics,” *Chem. Mater.*, vol. 28, no. 18, pp. 6501–6510, Sep. 2016, doi: 10.1021/acs.chemmater.6b01747.

[222] S. Kavadiya, J. Strzalka, D. M. Niedzwiedzki, and P. Biswas, “Crystal reorientation in methylammonium lead iodide perovskite thin film with thermal annealing,” *J. Mater. Chem. A*, vol. 7, no. 20, pp. 12790–12799, 2019, doi: 10.1039/C9TA02358E.

[223] S. A. Fateev *et al.*, “Solution Processing of Methylammonium Lead Iodide Perovskite from γ-Butyrolactone: Crystallization Mediated by Solvation Equilibrium,” *Chem. Mater.*, vol. 30, no. 15, pp. 5237–5244, Aug. 2018, doi: 10.1021/acs.chemmater.8b01906.

[224] M. A. Pérez-Osorio *et al.*, “Vibrational Properties of the Organic–Inorganic Halide Perovskite $CH_3NH_3PbI_3$ from Theory and Experiment: Factor Group Analysis, First-Principles Calculations, and Low-Temperature Infrared Spectra,” *J. Phys. Chem. C*, vol. 119, no. 46, pp. 25703–25718, Nov. 2015, doi: 10.1021/acs.jpcc.5b07432.

[225] M. A. Pérez-Osorio *et al.*, “Raman Spectrum of the Organic–Inorganic Halide Perovskite $CH_3NH_3PbI_3$ from First Principles and High-Resolution Low-Temperature Raman Measurements,” *J. Phys. Chem. C*, vol. 122, no. 38, pp. 21703–21717, Sep. 2018, doi: 10.1021/acs.jpcc.8b04669.

[226] C. Quarti *et al.*, “The Raman Spectrum of the $CH_3NH_3PbI_3$ Hybrid Perovskite: Interplay of Theory and Experiment,” *J. Phys. Chem.*

Lett., vol. 5, no. 2, pp. 279–284, Jan. 2014, doi: 10.1021/jz402589q.

[227] L.-Q. Xie *et al.*, “Organic–inorganic interactions of single crystalline organolead halide perovskites studied by Raman spectroscopy,” *Phys. Chem. Chem. Phys.*, vol. 18, no. 27, pp. 18112–18118, 2016, doi: 10.1039/C6CP01723A.

[228] R. Biswas, W. Carpenter, G. A. Voth, and A. Tokmakoff, “Molecular modeling and assignment of IR spectra of the hydrated excess proton in isotopically dilute water,” *J. Chem. Phys.*, vol. 145, no. 15, p. 154504, Oct. 2016, doi: 10.1063/1.4964723.

[229] R. B. Penland, S. Mizushima, C. Curran, and J. V Quagliano, “Infrared Absorption Spectra of Inorganic Coordination Complexes. X. Studies of Some Metal-Urea Complexes[1a,b],” *J. Am. Chem. Soc.*, vol. 79, no. 7, pp. 1575–1578, Apr. 1957, doi: 10.1021/ja01564a014.

[230] T. Glaser *et al.*, “Infrared Spectroscopic Study of Vibrational Modes in Methylammonium Lead Halide Perovskites,” *J. Phys. Chem. Lett.*, vol. 6, no. 15, pp. 2913–2918, Aug. 2015, doi: 10.1021/acs.jpclett.5b01309.

[231] M. Acik *et al.*, “Substitutional Growth of Methylammonium Lead Iodide Perovskites in Alcohols,” *Adv. Energy Mater.*, vol. 8, no. 5, p. 1701726, Feb. 2018, doi: 10.1002/aenm.201701726.

[232] A. P. Gray and R. C. Lord, “Rotation-Vibration Spectra of Methyl Amine and Its Deuterium Derivatives,” *J. Chem. Phys.*, vol. 26, no. 3, pp. 690–705, 1957, doi: 10.1063/1.1743369.

[233] Y. Wen, Y.-G. Tang, and G.-Q. Yan, “Large grain size $CH_3NH_3PbI_3$ film for perovskite solar cells with hydroic acid additive,” *AIP Adv.*, vol. 8, no. 9, p. 95226, Sep. 2018, doi: 10.1063/1.5048424.

[234] Z. Dang *et al.*, “In Situ Transmission Electron Microscopy Study of Electron Beam-Induced Transformations in Colloidal Cesium Lead Halide Perovskite Nanocrystals,” *ACS Nano*, vol. 11, no. 2, pp. 2124–2132, Feb. 2017, doi: 10.1021/acsnano.6b08324.

[235] W. Zhu *et al.*, “A facile,solvent vapor–fumigation-induced,self-repair recrystallization of $CH_3NH_3PbI_3$ films for high-performance perovskite solar cells,” *Nanoscale*, vol. 7, no. 12, pp. 5427–5434, 2015, doi: 10.1039/C5NR00225G.

[236] Y. Li *et al.*, “Realizing full coverage of perovskite film on substrate surface during solution processing: Characterization and elimination of uncovered surface,” *J. Power Sources*, vol. 320, pp. 204–211, 2016, doi: 10.1016/j.jpowsour.2016.04.098.

[237] P. C. Harikesh *et al.*, “Doping and Switchable Photovoltaic Effect in Lead-Free Perovskites Enabled by Metal Cation Transmutation,” *Adv. Mater.*, vol. 30, no. 34, p. 1802080, 2018, doi: 10.1002/adma.201802080.

[238] S. Weber, T. Rath, B. Kunert, R. Resel, T. Dimopoulos, and G. Trimmel, “Dependence of material properties and photovoltaic performance of triple cation tin perovskites on the iodide to bromide ratio,” *Monatshefte für Chemie - Chem. Mon.*, vol. 150, no. 11, pp. 1921–1927, 2019, doi: 10.1007/s00706-019-02503-6.

[239] H. Jin *et al.*, “It’s a trap! On the nature of localised states and charge trapping in lead halide perovskites,” *Mater. Horiz.*, vol. 7, pp. 397–410, 2020, doi: 10.1039/C9MH00500E.

[240] Y. A. Yaraliyev, “Oxidation of iodide ions by means of cyclic voltammetry,” *Electrochim. Acta*, vol. 29, no. 9, pp. 1213–1214, 1984, doi: 10.1016/0013-4686(84)87181-9.

[241] W.-W. Liu *et al.*, “Interface Engineered Binary Platinum Free Alloy-based Counter Electrodes with Improved Performance in Dye-Sensitized Solar Cells,” *Sci. Rep.*, vol. 10, no. 1, p. 9157, 2020, doi: 10.1038/s41598-020-64965-7.

[242] C. Yang, A. Tang, F. Teng, and K. Jiang, “Electrochemistry of Perovskite $CH_3NH_3PbI_3$ crystals,” *Acta Physico-Chimica Sinica*, vol. 34, no. 11. pp. 1197–1201, 2018, doi: 10.3866/PKU.WHXB201804097.

[243] S. Karastogianni and S. Girousi, “Electrochemical Behavior and

Voltammetric Determination of a Manganese(II) Complex at a Carbon Paste Electrode," *Anal. Chem. Insights*, vol. 11, pp. 1–11, Jan. 2016, doi: 10.4137/ACI.S32150.

[244] H. Tang and B. Pesic, "Electrochemistry of $ErCl_3$ and morphology of erbium electrodeposits produced on Mo substrate in early stages of electrocrystallization from LiCl–KCl molten salts," *Electrochim. Acta*, vol. 133, pp. 224–232, 2014, doi: 10.1016/j.electacta.2014.04.014.

[245] M. Shi, Z. Chen, and J. Sun, "Determination of chloride diffusivity in concrete by AC impedance spectroscopy," *Cem. Concr. Res.*, vol. 29, no. 7, pp. 1111–1115, 1999, doi: 10.1016/S0008-8846(99)00079-4.

[246] G. Richardson *et al.*, "Can slow-moving ions explain hysteresis in the current–voltage curves of perovskite solar cells?," *Energy Environ. Sci.*, vol. 9, no. 4, pp. 1476–1485, 2016, doi: 10.1039/C5EE02740C.

[247] X. Li *et al.*, "High Performance of Manganese Porphyrin Sensitized p-Type $CuFe_2O_4$ Photocathode for Solar Water Splitting to Produce Hydrogen in a Tandem Photoelectrochemical Cell," *Catalysts*, vol. 8, p. 108, Mar. 2018, doi: 10.3390/catal8030108.

[248] Y. Wu, Z. Yue, A. Liu, P. Yang, and M. Zhu, "P-Type Cu-Doped $Zn_{0.3}Cd_{0.7}S$/Graphene Photocathode for Efficient Water Splitting in a Photoelectrochemical Tandem Cell," *ACS Sustain. Chem. Eng.*, vol. 4, no. 5, pp. 2569–2577, May 2016, doi: 10.1021/acssuschemeng.5b01795.

[249] I. Hossain *et al.*, "Photo-degradation of perovskite solar cells: Modeling and Simulation," in *2018 IEEE 7th World Conference on Photovoltaic Energy Conversion (WCPEC) (A Joint Conference of 45th IEEE PVSC, 28th PVSEC & 34th EU PVSEC)*, 2018, pp. 1122–1124, doi: 10.1109/PVSC.2018.8548193.

[250] J. Tong, Y. Liu, Q. Peng, W. Hu, and Q. Wu, "An efficient Sb-SnO_2-supported IrO_2 electrocatalyst for the oxygen evolution reaction in

acidic medium," *J. Mater. Sci.*, vol. 52, pp. 13427–13443, 2017, doi: 10.1007 / s10853-017-1447-1.

[251] P. K. Gupta, A. Bhandari, S. Saha, J. Bhattacharya, and R. G. S. Pala, "Modulating Oxygen Evolution Reactivity in MnO_2 through Polymorphic Engineering," *J. Phys. Chem. C*, vol. 123, no. 36, pp. 22345–22357, Sep. 2019, doi: 10.1021/acs.jpcc.9b05823.

[252] M. Anaya *et al.*, "Electron injection and scaffold effects in perovskite solar cells," *J. Mater. Chem. C*, vol. 5, no. 3, pp. 634–644, 2017, doi: 10.1039/C6TC04639H.

[253] M. Alidaei, M. Izadifard, M. Ghazi, and V. Ahmadi, "Efficiency enhancement of perovskite solar cells using structural and morphological improvement of $CH_3NH_3PbI_3$ absorber layers," *Mater. Res. Express*, vol. 5, 2018, doi: 10.1088/2053-1591/aaa616.

[254] I. Gelmetti *et al.*, "Energy alignment and recombination in perovskite solar cells: weighted influence on the open circuit voltage," *Energy Environ. Sci.*, vol. 12, no. 4, pp. 1309–1316, 2019, doi: 10.1039/C9EE00528E.

[255] M. Ledinský *et al.*, "Raman Spectroscopy of Organic–Inorganic Halide Perovskites," *J. Phys. Chem. Lett.*, vol. 6, pp. 401–406, Feb. 2015, doi: 10.1021/jz5026323.

[256] O. Flender, J. R. Klein, T. Lenzer, and K. Oum, "Ultrafast photoinduced dynamics of the organolead trihalide perovskite $CH_3NH_3PbI_3$ on mesoporous TiO_2 scaffolds in the 320–920 nm range," *Phys. Chem. Chem. Phys.*, vol. 17, no. 29, pp. 19238–19246, 2015, doi: 10.1039/C5CP01973G.

[257] H. Abid, A. Trigui, A. Mlayah, E. K. Hlil, and Y. Abid, "Phase transition in organic–inorganic perovskite $(C_9H_{19}NH_3)_2PbI_2Br_2$ of long-chain alkylammonium," *Results Phys.*, vol. 2, pp. 71–76, 2012, doi: 10.1016/j.rinp.2012.04.003.

[258] D. Lin-Vien, N. B. Colthup, W. G. Fateley, and J. G. Grasselli, "CHAPTER 14 - Organic Sulfur Compounds," in *The Handbook of*

Infrared and Raman Characteristic Frequencies of Organic Molecules, D. Lin-Vien, N. B. Colthup, W. G. Fateley, and J. G. Grasselli, Eds. San Diego: Academic Press, 1991, pp. 225–250.

[259] J. Workman, “21 - Infrared Spectral Correlation Charts,” in *The Handbook of Organic Compounds*, J. Workman, Ed. Burlington: Academic Press, 2001, pp. 237–242.

[260] E. Jokar, C.-H. Chien, A. Fathi, M. Rameez, Y.-H. Chang, and E. W.-G. Diau, “Slow surface passivation and crystal relaxation with additives to improve device performance and durability for tin-based perovskite solar cells,” *Energy Environ. Sci.*, vol. 11, no. 9, pp. 2353–2362, 2018, doi: 10.1039/C8EE00956B.

[261] Q. Jiang *et al.*, “Surface passivation of perovskite film for efficient solar cells,” *Nat. Photonics*, vol. 13, no. 7, pp. 460–466, 2019, doi: 10.1038/s41566-019-0398-2.

[262] C. Tablero Crespo, “Absorption coefficients data of lead iodine perovskites using 14 different organic cations,” *Data Br.*, vol. 27, p. 104636, 2019, doi: 10.1016/j.dib.2019.104636.

[263] D. Ghosh *et al.*, “Lattice Expansion in Hybrid Perovskites: Effect on Optoelectronic Properties and Charge Carrier Dynamics,” *J. Phys. Chem. Lett.*, vol. 10, no. 17, pp. 5000–5007, Sep. 2019, doi: 10.1021/acs.jpclett.9b02020.

[264] B. P. Nguyen *et al.*, “Phase formation and local charge transport of lead-free $CH_3NH_3Sn(I_{1-x}Br_x)_3 (0 \leq x \leq 1)$ perovskite solar cells fabricated by solvent optimization,” *Sol. Energy*, vol. 186, pp. 136–144, 2019, doi: 10.1016/j.solener.2019.05.007.

[265] S. Chen *et al.*, “A Facile Approach to Prepare Black TiO_2 with Oxygen Vacancy for Enhancing Photocatalytic Activity,” *Nanomaterials*, vol. 8, no. 4, p. 245, Apr. 2018, doi: 10.3390/nano8040245.

[266] F. Amano, M. Nakata, A. Yamamoto, and T. Tanaka, “Effect of Ti^{3+} Ions and Conduction Band Electrons on Photocatalytic and Photoelectrochemical Activity of Rutile Titania for Water

Oxidation," *J. Phys. Chem. C*, vol. 120, no. 12, pp. 6467–6474, Mar. 2016, doi: 10.1021/acs.jpcc.6b01481.

[267] J. Cai *et al.*, "Synergetic Enhancement of Light Harvesting and Charge Separation over Surface-Disorder-Engineered TiO_2 Photonic Crystals," *Chem*, vol. 2, no. 6, pp. 877–892, 2017, doi: 10.1016/j.chempr.2017.05.006.

[268] T. P. M. Alegre, F. G. G. Hernández, A. L. C. Pereira, and G. Medeiros-Ribeiro, "Landé g Tensor in Semiconductor Nanostructures," *Phys. Rev. Lett.*, vol. 97, no. 23, p. 236402, Dec. 2006, doi: 10.1103/PhysRevLett.97.236402.

[269] Y. Dang and A. R. West, "Oxygen stoichiometry, chemical expansion or contraction, and electrical properties of rutile, $TiO_{2\pm\delta}$ ceramics," *J. Am. Ceram. Soc.*, vol. 102, no. 1, pp. 251–259, 2019, doi: 10.1111/jace.15889.

[270] A. Naldoni *et al.*, "Effect of Nature and Location of Defects on Bandgap Narrowing in Black TiO_2 Nanoparticles," *J. Am. Chem. Soc.*, vol. 134, no. 18, pp. 7600–7603, May 2012, doi: 10.1021/ja3012676.

[271] A. Moya *et al.*, "Oxygen vacancies and interfaces enhancing photocatalytic hydrogen production in mesoporous CNT/TiO_2 hybrids," *Appl. Catal. B Environ.*, vol. 179, pp. 574–582, 2015, doi: 10.1016/j.apcatb.2015.05.052.

[272] M. M. Araújo *et al.*, "Anatase TiO_2 nanocrystals anchored at inside of SBA-15 mesopores and their optical behavior," *Appl. Surf. Sci.*, vol. 389, pp. 1137–1147, 2016, doi: 10.1016/j.apsusc.2016.08.018.

[273] M. Rehan, X. Lai, and G. M. Kale, "Hydrothermal synthesis of titanium dioxide nanoparticles studied employing in situ energy dispersive X-ray diffraction," *CrystEngComm*, vol. 13, no. 11, pp. 3725–3732, 2011, doi: 10.1039/C0CE00781A.

[274] N. Syuhada, B. Yuliarto, and Nugraha, "Synthesis and Characterization Hierarchical Three-Dimensional TiO_2 Structure

via Hydrothermal Method," *IOP Conf. Ser. Mater. Sci. Eng.*, vol. 367, p. 12052, 2018, doi: 10.1088/1757-899x/367/1/012052.

[275] U. Diebold and T. E. Madey, "TiO_2 by XPS," *Surf. Sci. Spectra*, vol. 4, no. 3, pp. 227–231, Jul. 1996, doi: 10.1116/1.1247794.

[276] J. T. Mayer, U. Diebold, T. E. Madey, and E. Garfunkel, "Titanium and reduced titania overlayers on titanium dioxide(110)," *J. Electron Spectros. Relat. Phenomena*, vol. 73, no. 1, pp. 1–11, 1995, doi: 10.1016/0368-2048(94)02258-5.

[277] M. C. Biesinger, L. W. M. Lau, A. R. Gerson, and R. S. C. Smart, "Resolving surface chemical states in XPS analysis of first row transition metals, oxides and hydroxides: Sc, Ti, V, Cu and Zn," *Appl. Surf. Sci.*, vol. 257, no. 3, pp. 887–898, 2010, doi: 10.1016/j.apsusc.2010.07.086.

[278] W. Göpel *et al.*, "Surface defects of TiO_2(110): A combined XPS, XAES AND ELS study," *Surf. Sci.*, vol. 139, no. 2, pp. 333–346, 1984, doi: 10.1016/0039-6028(84)90054-2.

[279] Y.-C. Lu *et al.*, "In Situ Ambient Pressure X-ray Photoelectron Spectroscopy Studies of Lithium-Oxygen Redox Reactions," *Sci. Rep.*, vol. 2, no. 1, p. 715, 2012, doi: 10.1038/srep00715.

[280] P. Jonnard, I. Jarrige, and C. Bonnelle, "Satellite lines induced by electrons of near-threshold energy in the x-ray emission band spectra of 3d, 4d, and 5d transition metals," *Phys. Rev. B*, vol. 71, p. 155107, Apr. 2005, doi: 10.1103/PhysRevB.71.155107.

[281] I. Ikemoto, K. Ishii, H. Kuroda, and J. M. Thomas, "Satellite phenomena in the X-ray photoelectron spectra of some titanium compounds," *Chem. Phys. Lett.*, vol. 28, no. 1, pp. 55–59, 1974, doi: 10.1016/0009-2614(74)80015-1.

[282] S. K. Sen, J. Riga, and J. Verbist, "2s and 2p X-ray photoelectron spectra of Ti^{4+} ion in TiO_2," *Chem. Phys. Lett.*, vol. 39, no. 3, pp. 560–564, 1976, doi: 10.1016/0009-2614(76)80329-6.

[283] B. Bharti, S. Kumar, H.-N. Lee, and R. Kumar, "Formation of oxygen vacancies and Ti^{3+} state in TiO_2 thin film and enhanced

optical properties by air plasma treatment," *Sci. Rep.*, vol. 6, p. 32355, Aug. 2016, doi: 10.1038/srep32355.

[284] Z. Jiang, D. Ding, L. Wang, Y. Zhang, and L. Zan, "Interfacial effects of MnO_x-loaded TiO_2 with exposed {001} facets and its catalytic activity for the photoreduction of CO_2," *Catal. Sci. Technol.*, vol. 7, no. 14, pp. 3065–3072, 2017, doi: 10.1039/C7CY00729A.

[285] H. Perron *et al.*, "Combined investigation of water sorption on TiO_2 rutile (110) single crystal face: XPS vs. periodic DFT," *Surf. Sci.*, vol. 601, no. 2, pp. 518–527, 2007, doi: 10.1016/j.susc.2006.10.015.

[286] J. Zou, J. Gao, and F. Xie, "An amorphous TiO_2 sol sensitized with H_2O_2 with the enhancement of photocatalytic activity," *J. Alloy. Compd. - J Alloy. Compd.*, vol. 497, pp. 420–427, May 2010, doi: 10.1016/j.jallcom.2010.03.093.

[287] L. K. Preethi, R. P. Antony, T. Mathews, L. Walczak, and C. S. Gopinath, "A Study on Doped Heterojunctions in TiO_2 Nanotubes: An Efficient Photocatalyst for Solar Water Splitting," *Sci. Rep.*, vol. 7, no. 1, p. 14314, 2017, doi: 10.1038/s41598-017-14463-0.

[288] A.-A. Mel, E. Gautron, C.-H. Choi, B. Angleraud, A. Granier, and P.-Y. Tessier, "Titanium carbide/carbon composite nanofibers prepared by a plasma process," *Nanotechnology*, vol. 21, p. 435603, Oct. 2010, doi: 10.1088/0957-4484/21/43/435603.

[289] S. A. Abdullah *et al.*, "Photoluminescence study of trap-state defect on TiO_2 thin films at different substrate temperature via RF magnetron sputtering," *J. Phys. Conf. Ser.*, vol. 995, p. 12067, 2018, doi: 10.1088/1742-6596/995/1/012067.

[290] C. Mercado, Z. Seeley, A. Bandyopadhyay, S. Bose, and J. L. McHale, "Photoluminescence of Dense Nanocrystalline Titanium Dioxide Thin Films: Effect of Doping and Thickness and Relation to Gas Sensing," *ACS Appl. Mater. Interfaces*, vol. 3, no. 7, pp. 2281–2288, Jul. 2011, doi: 10.1021/am2006433.

[291] D. K. Pallotti, L. Passoni, P. Maddalena, F. Di Fonzo, and S. Lettieri, “Photoluminescence Mechanisms in Anatase and Rutile TiO_2,” *J. Phys. Chem. C*, vol. 121, no. 16, pp. 9011–9021, Apr. 2017, doi: 10.1021/acs.jpcc.7b00321.

[292] C. Jin, B. Liu, Z. Lei, and J. Sun, “Structure and photoluminescence of the TiO_2 films grown by atomic layer deposition using tetrakis-dimethylamino titanium and ozone,” *Nanoscale Res. Lett.*, vol. 10, no. 1, p. 95, 2015, doi: 10.1186/s11671-015-0790-x.

[293] A. Aritonang, H. Surahman, Y. Krisnandi, and J. Gunlazuardi, “Photo-electro-catalytic performance of highly ordered nitrogen doped TiO_2 nanotubes array photoanode,” *IOP Conf. Ser. Mater. Sci. Eng.*, vol. 172, p. 12005, Feb. 2017, doi: 10.1088/1757-899X/172/1/012005.

[294] J. Coates, “Interpretation of Infrared Spectra, A Practical Approach,” in *Encyclopedia of Analytical Chemistry*, 2006.

[295] H. Yan, X. Wang, M. Yao, and X. Yao, “Band structure design of semiconductors for enhanced photocatalytic activity: The case of TiO_2,” *Prog. Nat. Sci. Mater. Int.*, vol. 23, no. 4, pp. 402–407, 2013, doi: 10.1016/j.pnsc.2013.06.002.

[296] F. El Kamel, P. Gonon, and C. Vallée, “Experimental evidence for the role of electrodes and oxygen vacancies in voltage nonlinearities observed in high-k metal-insulator-metal capacitors,” *Appl. Phys. Lett.*, vol. 91, no. 17, p. 172909, Oct. 2007, doi: 10.1063/1.2803221.

[297] X. Xin, T. Xu, J. Yin, L. Wang, and C. Wang, “Management on the location and concentration of Ti^{3+} in anatase TiO_2 for defects-induced visible-light photocatalysis,” *Appl. Catal. B Environ.*, vol. 176–177, pp. 354–362, 2015, doi: 10.1016/j.apcatb.2015.04.016.